00003

QUARTERLY REPORT NO.1, PHASE II
CONTRACT JPL 952129

ION ENGINE THRUST VECTOR STUDY
DECEMBER 1968

HUGHES RESEARCH LABORATORIES · MALIBU

HUGHES RESEARCH LABORATORIES
Malibu, California

a division of hughes aircraft company

ION ENGINE THRUST VECTOR STUDY

Quarterly Report No. 1, Phase II
JPL Contract 952129

Prepared by

G. R. Brewer, K. Amboss, G. Nudd,
H. King, R. Seliger, and S. Kami

December 1968

TABLE OF CONTENTS

LIST OF ILLUSTRATIONS

x

LIST OF TABLES

ABSTRACT

This report describes the results of the analytical portion of the program to establish the expected degree of thrust misalignment in an electron bombardment ion thruster. The analysis includes the probable misalignment that might occur due to mechanical displacement and time, and its effect on the thrust vector. An analysis of mechanical displacement due to thermal and mechanical stresses on the screen and accel electrodes is presented. An analysis of the design of a thrust stand is presented. The thrust stand is required to complete the second phase, the experimental determination of the thrust with mechanically imposed electrode misalignments.

I. INTRODUCTION AND SUMMARY

As a result of comprehensive studies over the past three years, the fundamental design concepts associated with solar powered electric propulsion systems for interplanetary missions have become fairly well defined. It is known, for example, that the engine array will involve a cluster of thruster modules which may be arranged on a frame which can be translated in two directions (or other suitable freedom of motion) relative to the spacecraft. This translational motion is necessary in order to assure that the center of thrust will pass through the center of mass of the spacecraft, for any configuration of active and inactive thrusters. In addition to changes in the thrust axis due to switching of thrusters, the vector from an individual thruster will not necessarily be along the axis and could change slightly in magnitude and direction with time. The effect of these misaligned thrust vector components around the pitch and yaw axes can be negated by the translation mechanism mentioned above. The component around the roll axis, however, can be compensated only by the spacecraft attitude control system or by gimballing some or all of the thrusters. Therefore, it is of considerable importance to SEP spacecraft design to know the expected thrust vector misalignment as a function of various thruster operational parameters, mechanical displacements, and time. Such knowledge is also fundamental to the development of techniques of thruster construction for reducing the changes in the thrust vector.

The objective of this program is the establishment, by analysis and subsequently by experiment, of an expected change in thrust vector from an electron bombardment engine, as a result of all known or anticipated causes. The first phase of this program is devoted to the analysis of expected electrode displacements, determination of the effects of these displacements on the ion trajectories and thereby on the thrust vector, and the design of apparatus for experimental verification, in Phase II. This report covers the first nine-month effort comprising Phase I.

1

The misalignment of the thrust vector of an array of thrusters can arise from change in the magnitude of the axial thrust or from the transverse component of thrust from a single thruster. In turn, the total thrust (axial and transverse) of a thruster is made up of the thrust elements resulting from each aperture in the accelerator electrode system.

In the analysis of thrust vector misalignment, a comprehensive digital computer program was developed in order to determine the ion flow and trajectory conditions for a single hole as a function of the relative positions of the accelerator and screen electrode and ion current density. In this computer study the upstream plasma sheath (i.e., the source of ions) received careful attention; the program allowed changes in the shape and position of the sheath in the screen aperture. The position of the plasma emitting boundary was determined by an iterative technique, after which detailed trajectories were run. It was found that the sheath position and the average direction of the trajectories varied as the electrodes were perturbed in position. For changes in spacing between accel and screen electrodes, the principal cause of the change in current was the variation in plasma boundary area as this surface advances or recedes in the tapered screen aperture. With transverse electrode displacement the ion trajectories vary, with relatively little distortion of the plasma boundary. These relations, between ion optical characteristics and electrode displacement, are expressed by a number of linear coefficients.

Several possible causes of electrode misalignment are considered. Of these, the one which is inherent in this type thruster and which is of greatest importance is the warping or buckling of the screen and accel electrodes due to thermally induced stresses. Other causes (e.g., of transverse or rotational misalignment) will result from assembly errors or from shift caused by vibration; these causes are not amenable to accurate analysis but can be evaluated accurately in the experiments of Phase II. The thermal buckling problem received considerable attention. The temperature distribution in the screen and

2

accel electrodes due to various heat loads, heat input distributions, etc., was analyzed. The effect of these temperature distributions on the mechanical distortion of the electrodes was determined by means of a digital computer program. The predicted temperature distribution was compared with experimental data in one case, with good agreement. Therefore, by using the linear coefficients determined from the ion optical study together with expected electrode displacements, the expected change in thrust is determined. It is found, for example, that a change in axial thrust as high as 18% can be expected as a result of electrode warping.

The second major element of this phase of the program involved the design of experimental equipment for measuring the thrust vector of an electron bombardment thruster. A thruster was designed — of 30 cm, 2 kW size — to be representative of flight-type state-of-the-art mercury bombardment thrusters. Although not specifically part of Phase I, this thruster performance was verified experimentally as suitable for the purpose intended. During the evaluation of a number of different forms of thrust stand capable of measuring the four components of thrust desired, a new concept was conceived, analyzed in detail, and adopted for use in Phase II. This thrust stand design is novel in that the platform is floated on a pool of mercury with suitable linear force transducers to allow direct measurement of all transverse components of thrust. Comprehensive analysis showed that it exhibits the required sensitivity and stability. Layout designs of the thrust stand in the vacuum chamber have been made.

As a result of the work outlined above, we believe the objectives of Phase I have been met and Phase II can begin. As pointed out in the conclusions to this report, experimental work using the thrust stand should achieve more than the verification of analysis and experimental measurement of thrust vector components which is planned for Phase II. In addition, the thrust stand can be used effectively for a subsequent program of developing electrode support structures designed to reduce

transverse motion of electrodes due to assembly, vibration, and thermal warping, The ability to measure the thrust components accurately will provide the means for reducing the expected misalignment, since several of the possible causes are not amenable to reliable analysis.

In this report the ion optical study is discussed first, followed by an analysis of causes of electrode misalignment (principally thermal warping). In Section IV these two analyses are combined to yield the expected thrust change. The thruster and thrust stand design are given in detail in Section V, and conclusions are given briefly in Section VI.

II. ION OPTICAL STUDY

A. Introduction

The total thrust from an ion thruster consisting of an array of circular apertures is given by the time rate of change of the momentum of the ion particles exhausted from it. The velocity, and hence momentum, of each ion, is determined by the electric fields it experiences during its motion. Thus, a perturbation of these fields caused by an electrode misalignment will perturb the total thrust (magnitude and direction). A change in the total ion current will cause a similar change in total thrust. The purpose of the work reported here was to determine the exhaust momentum for various electrode perturbations and ion currents, and thus allow calculations of the expected variation in the thrust vector.

A number of the basic electrode misalignments considered are illustrated in Fig. 1. These were chosen to include the expected types of perturbations which an accel electrode can experience in assembly or operation of a thruster.

In Fig. 1(a) the electrode spacing is decreased while the rotational symmetry is preserved. This results in an increase in the magnitude of the thrust from this aperture, which may cause the direction of the thrust vector from the thruster as a whole to rotate. In Fig. 1(b), the electrodes are displaced normal to the beam axis, thus destroying its symmetry and causing a change in the magnitude and direction of the thrust vector. The case illustrated in Fig. 1(c) can be considered as the sum of the two effects above, which alters both the magnitude and direction of thrust vector.

It can be seen that the rotational symmetry of the flow generally will be destroyed and the perturbed flow will be formed about a curvilinear axis. It is not possible, in general, to determine this type of flow exactly, either with the analog or digital computer. However, a first order solution for the thrust vector has been formed by a combination of the axisymmetric and planar solutions obtained in the digital computer.
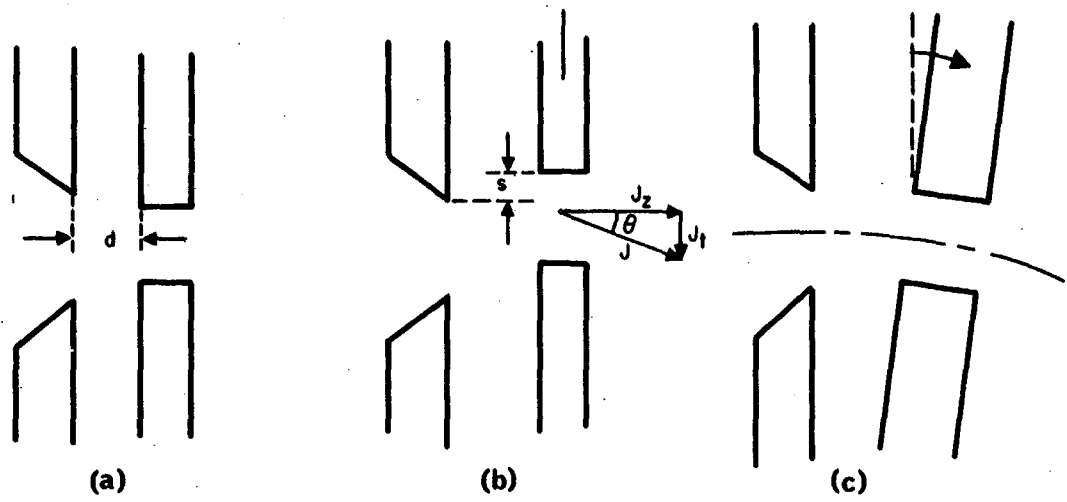
Fig. 1.   Basic electrode misalignments.

These ion flow calculations involve two fixed (in shape) bound-
aries (viz., the screen and accel electrodes) and two fluid boundaries
(viz., the upstream and downstream plasma surfaces). Fortunately
it was found that the shape and position of the downstream boundary
(the edge of the neutralized region) was relatively insensitive to up-
stream conditions and vice versa; its small changes did not affect the
ion flow. On the other hand, the upstream or ion source boundary
exerted a predominant effect on the ion current and trajectories; thus
considerable effort has been spent in assuring that the technique of
treatment of this surface is correct. This factor is also important
in this study in that the consideration of the fluidity of the upstream
boundary is an important difference between this thrust vector analysis
and that which has been carried out previously.

This section will describe first the techniques used in the ion
optical study; the analysis of the effect on ion flow of the several elec-
trode perturbations listed above will then be given. This analysis will
evolve linear coefficients between thrust and electrode displacement,
and these data will be used in Section IV to calculate the expected thrust
vector changes.

B.   Basic Techniques Employed

1.   Digital Computer Program

A digital computer program which determines the trajec-
tories of ions, assuming either rotational or planar symmetry, has been
used in this work. In most problems involving space charge flow, the
boundary conditions necessary for solution are prescribed on a given
surface, on which the potential variation or the normal derivative is
specified. On the other hand, problems involving plasma boundaries
involve "free" surface in the sense that the location of the boundary
must be found, given the nominal potential variation and the normal
derivative. This latter class of problem can be solved only by specifying
a boundary contour and by refining it in an iterative manner until the
desired boundary conditions are obtained.

The basic computer program uses finite difference techniques to solve Laplace's and Poisson's equations using boundary data specified by the user. Two types of boundaries are of interest: a Dirichlet boundary where the potential is known, and a Neumann boundary where the normal derivative of the potential is known. In order to specify these boundary data, the area of the accelerator is overlaid with a suitable mesh and the potential at each mesh point is calculated in terms of its neighbors. Hence the Laplace equation $\nabla^2 V = 0$ at point R, Z within the problem becomes $RV_{R-1, Z} + RV_{R, Z-1} + (R + 1/2) V_{R+1, Z} + (R - 1/2) V_{R, Z+1} - 4RV_{R, Z} = 0$ in terms of finite differences, where $V_{R, Z}$ is the potential at the mesh point R, Z. The ion source is then divided into segments of equal length and the emission is determined by Child's law, using the potential as calculated above at a given distance from the surface.

In practice, the region immediately in front of the emitter is known to be highly unstable and a "suppression factor" must be used in the calculation of the emission to ensure that the solutions converge. The trajectory of a characteristic ion from each segment is then determined using the electric fields associated with the Laplace solution. Charges appropriate to the current flow are then set in at each mesh point. The full Poisson solution can then be determined in terms of finite differences. The above process is repeated until the solutions converge.

Since the emitting surface in this case is a plasma, its shape and location are determined by the "self-consistent" electric fields at its surface. If the plasma sheath is considered to be thin and the surface well defined, its boundary conditions can be defined as

$$V (r_s) = const = V \text{ plasma}$$
$$E (r_s) = 0$$
$$\rho (r_s) = 0$$

where $V(r_s)$, $E(r_s)$ and $\rho(r_s)$ are the potential, electric field, and spacecharge, respectively, at r_s where r_s refers to points within

8

the plasma. A further boundary condition to be satisfied at the upstream boundary is that the ion emission from the plasma should be equivalent to the self-consistent space-charge flow from its surface.

In general, iterative methods must be used to determine the location and shape of the upstream and downstream boundaries self-consistently with the flow. The method used was to assume a trial boundary of the correct potential and then successively deform this until the other boundary conditions were satisfied. An electrolytic tank in conjunction with an analog computer was used to obtain an initial estimate of the upstream boundary shape and position. For this work an assumed downstream plasma boundary was used and the method of solution was similar to that described in Ref. 1. The boundary thus found was then used in the digital computer in order to determine the shape and location of the downstream plasma boundary.

2. The Unperturbed Accelerator

In the electron bombardment thruster the ions are extracted from a neutral plasma and given a directed velocity by a suitable electrode system. At an appropriate location outside the thruster the accelerated ions are mixed with electrons so that a neutral stream of charged particles is ejected from the spacecraft.

The design of the electrode system is governed by several considerations. The available ions must be focused efficiently so that the accelerated stream of ions has little transverse spread. At the same time, direct impingement on the accelerating electrode must be kept to a minimum to prevent it from being sputtered away. In addition, the mixing of electrons must be accomplished so that backstreaming of the electrons to the screen electrode is avoided. The accelerating electrode system also must be capable of drawing the required current density from the ion emitter.

The transition from the neutral plasma at a uniform potential to the region of pure ion flow, where fields exist, occurs within a very small dividing region within which the electrons having energy spread $\approx kT$ are reflected back into the plasma. It is therefore convenient to

9

regard the plasma as being bounded by a negligibly thin sheath, the Debye sheath. Since the plasma is a region of uniform potential, the sheath defines an equipotential; by the same definition the electric field normal to the sheath must vanish on the side facing the plasma and also on the side where the ion flow takes place.

The sheath thus assumes a position such that the space charge of the ions in the accelerating region can reduce the applied electric field to zero. This space charge field is determined by the rate at which ions are transported across the plasma sheath. Since no field can be set up to reflect them, the ion current density is always equal to the maximum available from the plasma. Since the plasma is (ideally) uniform, the ion current density is always uniform across the sheath and equal to the maximum available (assuming that sufficient potential is applied to the accelerator). Were it not for this property, the ion flow from the plasma sheath could be treated in identical fashion to the electron flow from a thermionic electron emitter. The principal property characterizing the plasma type ion emitter is thus its ability to adjust the boundary shape and position in order to satisfy the field and emission constraints discussed above.

The geometry and potential profile on the axis of the unperturbed aperture studied are shown in Fig. 2. The emitting plasma density was assumed to be such as to give a nominal perveance of 3.4×10^{-6} electron pervs. It can be seen that the ions, after extraction from the emitting plasma at a potential of approximately + 2.0 kV, are accelerated toward the accel electrode where the potential is - 2.0 kV. After passing through the aperture in the accel electrode, they are projected into an essentially field-free plasma at ground potential where neutralization takes place. The ion paths inside this latter plasma region are not deflected and the thrust from the aperture can be calculated from the ion trajectores at its (the downstream boundary) surface.

3.   Downstream Plasma Boundary

The boundary conditions applied for the solution of this downstream boundary are that the potential and the normal electric field be zero at the surface. The method used consisted of specifying the correct potential of zero volts on a trial boundary and examining the normal

10
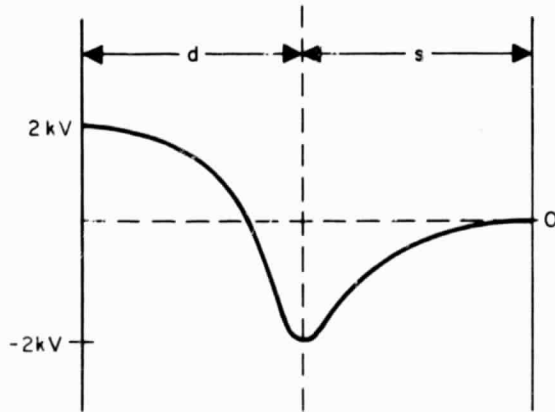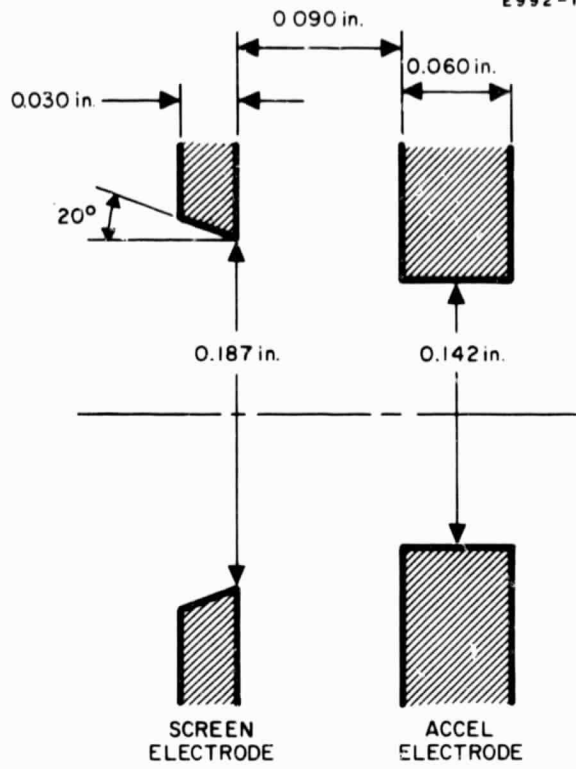
Fig. 2. Unperturbed electrode system and
voltage profile on axis.

11

component of electric field. The boundary was then deformed, until both these conditions were satisfied. This iterative method had to be employed since the potential and its derivative cannot be used as boundary conditions simultaneously as the Laplace and Poisson equations to be solved would become "overspecified."

The ion flow in a thruster consisting of a large number of closely packed co-planar accelerators can be considered to first order to be one dimensional. Hence, a first estimate of the location of the downstream boundary was obtained assuming that the flow was between infinite plane grids as illustrated in Fig. 3. The electric field at the injection and exit plane of the ions was assumed to be zero since this is a boundary condition of plasma surface. In this case the relationship between the spacings and voltages is given by[2]

$$\frac{s}{d} = (1 - R^{-1/2})^{1/2} (1 + 2R^{-1/2})$$

where

$$R = \frac{|V_2 - V_1|}{|V_2|}$$

and

V_1 = voltage of emitting plasma

V_2 = voltage of neutralization plasma

S = distance between emitting plasma and potential minimum

d = distance between neutralization plasma and potential minimum.

Hence a boundary at an axial distance of $(d + S)$, as calculated by the above formulas, from the screen was used as the first estimate. This was successively refined until the normal electric field became negligible. The final solution of the downstream boundary was found to be located at an axial distance of 0.33 in. in front of the screen.

V_1 V_2 V_3

PLANE OF   **PLANE OF**   **PLANE OF**
SCREEN ELECTRODE   **ACCEL ELECTRODE**   **DOWNSTREAM BOUNDARY**
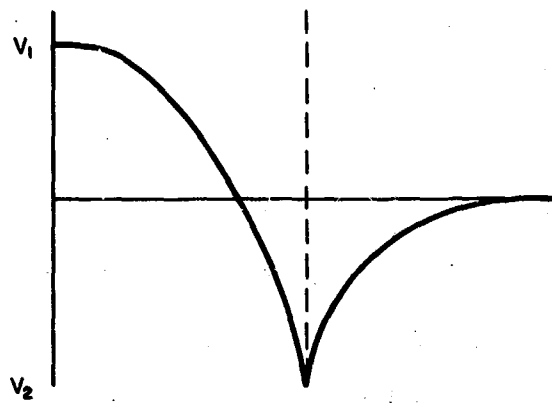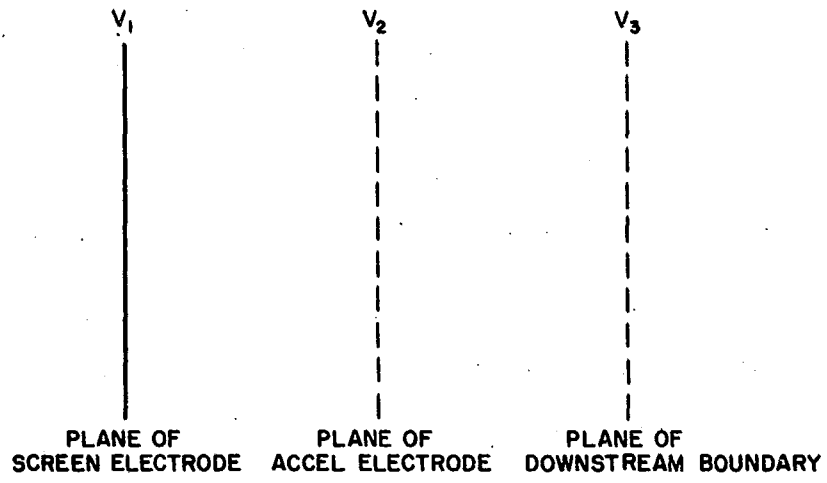
Fig. 3.   Idealized system assuming planar symmetry.

It can be seen that the ion trajectories in the vicinity of the boundary are straight and hence the calculations of thrust are not sensitive to small movements of this boundary. Since changes in the upstream boundary have been found to produce negligible changes in the downstream boundary, the same downstream boundary was used for all solutions.

4.   Upstream Boundary

The shape and position of the upstream plasma boundary exert a very strong effect on the ion flow and trajectories. In the calculations for the ion trajectories, the screen electrode was assumed to be at -40 V with respect to the emitting plasma and the accel electrode at - 4.0 kV with respect to the screen. In this case, the surface of the emitting plasma does not meet the screen electrode but will lie approximately parallel to it at a distance D (see Fig. 4). As a first estimate D was calculated by Child's law for parallel diodes with a voltage difference of 40 V.

The boundary conditions used for the solution of the emitting surface were the following:

1.   The emitting surface must be an equipotential

2.   The normal derivative of the voltage must be zero across the surface

3.   The emission density at each point across the surface must equal the ion arrival rate at the plasma surface.

These three conditions cannot be applied simultaneously in the solution of the Poisson equation and the trajectory equation without first determining the shape and location of the boundary. Hence an iterative method was used.
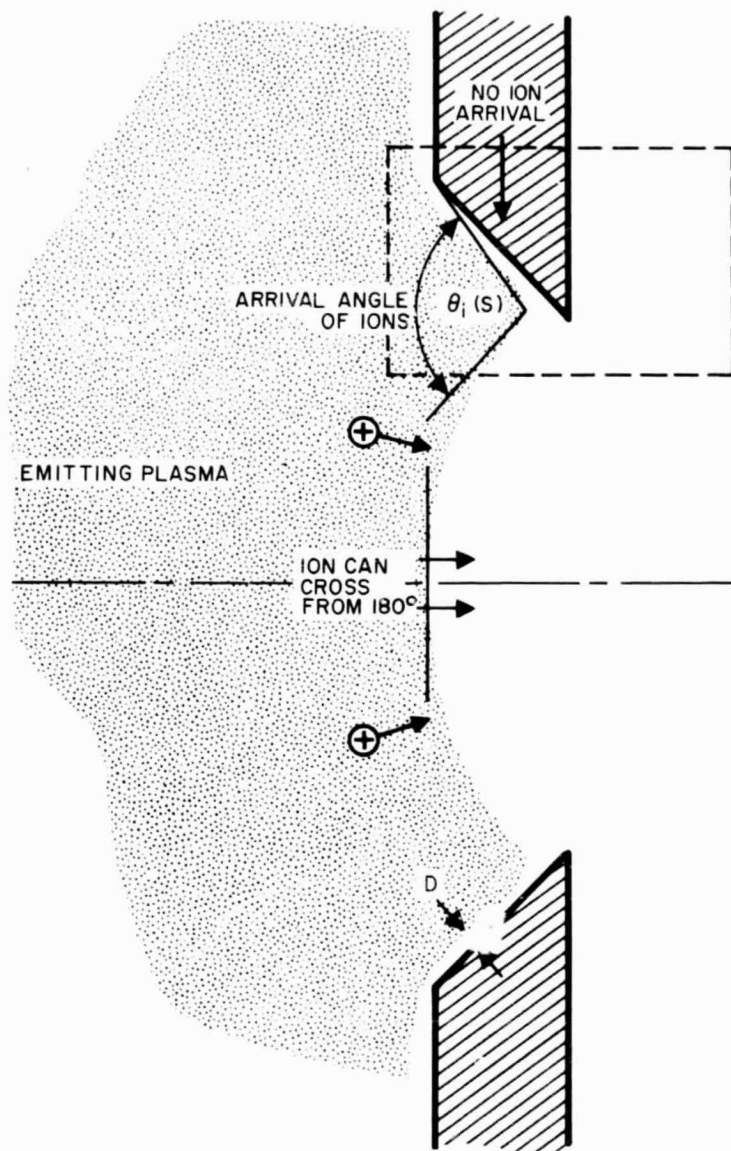
Fig. 4.   Geometry at the emitter, showing the shield-
ing effect of the screen.

The first of these conditions was met in the computer calculations by assuming that the emitting surface is a Dirichlet boundary, and the second by assuming that the emission is space-charge limited. Since the ion current is determined solely by the ion arrival rate, the location and shape of the surface must be deformed until the space-charge limited emission is exactly maintained by the arriving ions. Hence the ion arrival rate across the surface must be calculated first from the desired perveance of the unperturbed beam. In this case the assumed perveance was 3.4 μperv.[*] As a result of the finite thickness of the screen electrode the arriving ion current density is not uniform across the screen aperture. For a plasma density of 10^{11} ions/cm^3 and an ion temperature of 300°C, the mean free path is long compared with the screen thickness. In this case the ion paths can be assumed to be collision free in the vicinity of the screen electrode and the ion arrival rate at a point on the emitter surface can be calculated from the angle θ shown in Fig. 4, which shows a diametral plane through the aperture. Hence for the ith segment in this plane the current will be proportional to the angle θ_i. The comparable angle from which the ions can arrive at the plasma boundary in the plane normal to that shown in Fig. 4 is ψ. For the unperturbed case the current density $\bar{j}_i$ in an element represented by one trajectory was calculated from the required perveance P and the product of the angles θ_i and ψ_i, using $\bar{j}_i \propto \psi_i \theta_i$ and

$$\Sigma \bar{j}_i = \frac{P}{V^{3/2}} \frac{N}{A_s}$$

where N is the number of trajectories.

Because of the inherent instability in the immediate vicinity of the emitter, a fundamental limitation arises in the accuracy to which the boundary can be located self-consistently (see Appendix I). As a

---

[*]The computer program is set up to calculate the perveance in electron pervs. Hence this figure is given in these units.

result, the following method was used. A number of cases for various boundaries were first run as described above until the position of the boundary was known within approximately 0.0005 in. The best location for the boundary was then estimated and the correct current distribution is imposed upon it. This step is equivalent to assuming a small initial velocity of ions at the emitter, which is true in practice. The self-consistent plasma boundaries and beam profile for the unperturbed geometry with a total beam current of 0.132 µA are shown in Fig. 5.

5. Calculation of Thrust for Unperturbed System

The computer program, when used to solve problems with axial symmetry, divides the flow into a number of annular segments centered on the axis of symmetry and calculates a self-consistent ion trajectory for each segment. Each trajectory so calculated illustrates the flow of all the ions emitted from its annular segment. If I_i is the current associated with the ith annular segment, the total axial thrust T_A from the aperture is

$$T_A = k \Sigma I_i \sqrt{V} \cos \phi_i \qquad (1)$$

where the summation is for all the trajectories, k is a constant, and

V ≡ voltage difference between upstream and downstream plasma

ϕ_i ≡ angle between trajectory and axis at downstream boundary (exit angle).

The total axial thrust for the unperturbed geometry with a perveance of 3.4×10^{-6} was calculated to be 2.503×10^{-5} lb.

The transverse thrust $T_\perp$ is given by an expression similar to (1)

$$T_\perp = k \Sigma I_i \sqrt{V} \sin \phi_i \; ; \qquad (2)$$

because of axial symmetry, however, the summation leads to zero.

17
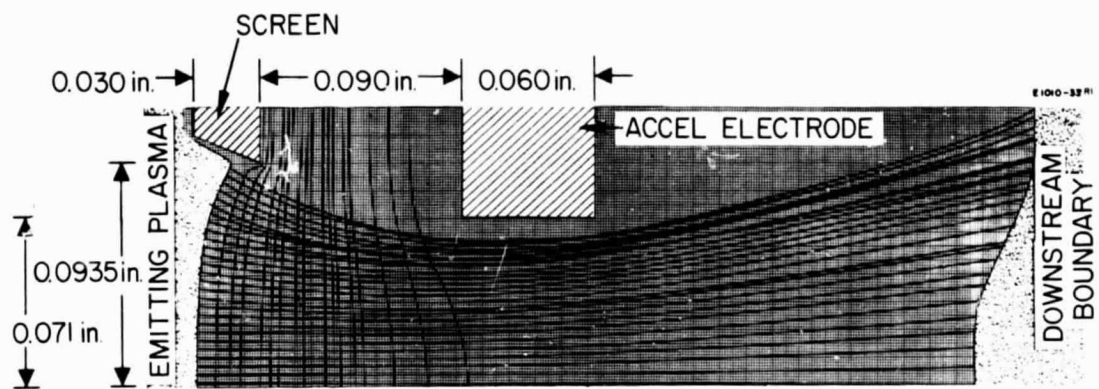
Fig. 5.   Trajectories for unperturbed accelerator (case 1).

C. Thrust Calculations with Displaced Electrodes

1. Axial Displacements

It has been found that the major contribution to the change in thrust for axial displacements results from the movement of the upstream plasma boundary rather than from the change of direction of the trajectories downstream. A change in screen-accel electrode spacing causes the form and position of the boundary to change, resulting in a change in emitting area and hence in the total emitted current. The total current I_t passing through a single aperture can be expressed as

$$I_t = \sum_o^{A_s} \bar{j}_o \, (\Delta A_i) \, F_i \tag{3}$$

where $\bar{j}_o$ is the density of current flowing through an element of area ΔA_i on the emitting surface, F_i is the "view factor" which accounts for the shielding effect of the screen electrode, A_s is the total curved surface area of the emitting plasma, and the summation is for all elements on the emitting surface. It can be seen that an increase in area A_s will cause an increase in total current and hence an increase in the thrust. The axial thrust from an aperture calculated from (1) can be expressed by means of (3) as

$$T = k\sqrt{V} \; \Sigma \bar{j}_o \, (\Delta A_i) \, F_i \cos \phi_i \;. \tag{4}$$

From (4) we can find the effect of small changes in the various parameters

$$\delta T_A = \Sigma \left(\frac{\partial T_i}{\partial (\Delta A_i)} \; \delta(\Delta A_i) \right) + \Sigma \left(\frac{\partial T_i}{\partial F_i} \; \delta F_i \right) + \Sigma \; \frac{\partial T_i}{\partial (\cos \psi_i)} \; \delta(\cos \phi_i)$$

$$= \Sigma T_i \; \frac{\delta(\Delta A_i)}{\Delta A_i} + \Sigma T_i \; \frac{\delta F_i}{F_i} + \Sigma T_i \; \frac{\delta(\cos \phi_i)}{\cos \phi_i} \;. \tag{5}$$

19

The first two components result solely from changes in the emitting plasma boundary, while the third is an ion optical effect. The relative importance of the three components can be estimated from the magnitudes of

$$\frac{\delta(\Delta A_i)}{\Delta A_i}, \quad \frac{\delta F_i}{F_i} \quad \text{and} \quad \frac{\delta(\cos \phi_i)}{\cos \phi_i} \quad .$$

When the solution obtained for the unperturbed system is compared with that for a 22% decrease in accel-screen spacing, the change in thrust resulting from ion optics can be shown to be small compared with that resulting from the boundary movement. This can readily be seen if δT_A is expressed as

$$\delta T_A = \Sigma \left(\frac{\partial T_i}{\partial I_i} \ \delta I_i \right) + \Sigma \left(\frac{\partial T_i}{\partial (\cos \phi_i)} \ \delta(\cos \phi_i) \right)$$

$$= \Sigma T_i \ \frac{\delta I_i}{I_i} + \Sigma T_i \ \frac{\delta(\cos \phi_i)}{\cos \phi_i} \tag{6}$$

and if the maximum values $\delta I_i / I_i$ and $\delta(\cos \phi_i)/\cos \phi_i$ are compared. Since

$$\delta \ \frac{(\cos \phi_i)}{\cos \phi_i} = \tan \phi_i \ \delta \phi_i \quad ,$$

ϕ_i is small (less than 20° for all trajectories and $\tan 20^\circ = 0.36$), and the maximum value of $\delta \phi_i < 0.1$, this term will be less than 0.036. However, the maximum value of $\delta I_i / I_i = 0.13$. Hence the change in thrust resulting from the change in current is the dominant factor in this case; this result is somewhat unexpected at first glance.

When the actual values rather than the maximum values are used for the 22% decrease in axial spacing, summing for all the trajectories we obtain

$$\frac{\delta I_t}{I_t} = 0.117;$$

hence, for δT_A,

$$\Sigma T_i \frac{\delta I_i}{I_i} = 2.9 \times 10^{-6} \text{ lb}$$

$$\Sigma T_i \frac{\delta(\cos \phi_i)}{\cos \phi_i} = 3.6 \times 10^{-7} \text{ lb} .$$

However, the increase in emitted current results from two factors: the increase in emission area and the increase in view factor. We can therefore write

$$I_t = \Sigma I_i = J_0 \Sigma(\Delta A_i) F$$

$$\delta I_t = \Sigma \frac{\partial I_i}{\partial(\Delta A_i)} \delta(\Delta A_i) + \Sigma \frac{\partial I_i}{\partial F} \delta F$$

$$= \Sigma J_0 \delta(\Delta A_i) F + \Sigma J_0 \delta F (\Delta A_i)$$

$$= \Sigma J_0 (\Delta A_i) F \frac{\delta(\Delta A_i)}{\Delta A_i} + \Sigma J_0 \delta F (\Delta A_i) . \qquad (7)$$

Since the trajectories calculated represent annuli of equal thickness, the fractional change in emitting area will be the same for all elements and we can write

$$\frac{\delta(\Delta A_i)}{\Delta A_i} \text{ (is constant)} = \frac{\delta A_s}{A_s} . \qquad (8)$$

Therefore,

$$\delta I_t = I_t \frac{\delta A_s}{A_s} + \Sigma J_o \, \delta F_i (\Delta A_i)$$

or

$$\frac{\delta I_t}{I_t} = \frac{\delta A_s}{A_s} + \frac{\Sigma J_o \, \delta F_i (\Delta A_i)}{I_t} \quad . \tag{9}$$

In this case $\delta A_s / A_s$ was calculated to be approximately 0.09; hence the change in current resulting from the change in view factor is approximately 2.7%.

We can now write the change in thrust δT_A as

$$\frac{\delta T_A}{T_A} = \frac{\delta T_{1,A}}{T_A} + \frac{\delta T_{2,A}}{T_A} + \frac{\delta T_{3,A}}{T_A} \tag{10}$$

where

$\delta T_{1,A} \equiv$ change in axial thrust due to change in ion paths alone

$\delta T_{2,A} \equiv$ change in axial thrust due to change in emitting area

$\delta T_{3,A} \equiv$ change in axial thrust due to change in screen electrode shielding.

A change in the ion arrival rate will also introduce a perturbation which preserves the axial symmetry of the system. In this case the change in thrust is given by

$$\delta T_A = \Sigma T_i \frac{\delta I_i}{I_i} + \Sigma T_i \frac{\delta(\cos \phi_i)}{\cos \phi_i} \tag{11}$$

where

$$\delta I_i = I_t \frac{\delta A_s}{A_s} + I_t \frac{\delta \bar{j}_o}{\bar{j}_o} + \Sigma \bar{j}_o \, \delta F(\Delta A_i) \tag{12}$$

because the ion arrival rate $\bar{j}_o$ varies.

Using the above notation we can write

$$\frac{\delta T_A}{T_A} = \frac{\delta T_{1,A}}{T_A} + \frac{\delta T_{2,A}}{T_A} + \frac{\delta T_{3,A}}{T_A} + \frac{\delta T_{4,A}}{T_A} \tag{13}$$

where $\delta T_{4,A} \equiv$ the change in thrust because of the change in ion arrival rate.

Five cases with axial symmetry have been solved for three "ion arrival rates," and the total thrust is given in Tables I, II, and III. The three values of ion arrival rate assumed in Table I are such as to maintain an ion current density at the screen aperture of the unperturbed system of 7.87 mA/cm^2 (cases 1 and 2), 4.5 mA/cm^2 (case 3) and 2.28 mA/cm^2 (cases 4 and 5). The electrode perturbation considered was an axial movement of the accel electrode of 0.020 in. toward the screen. The trajectories calculated for cases 1 through 5 are shown in Fig. 5 to 9.

For small perturbations the change in thrust can be divided into components parts according to eq. (13). This has been done for the cases 1, 2, 4, and 5 shown in Table I, and the results are shown in Table II.

23
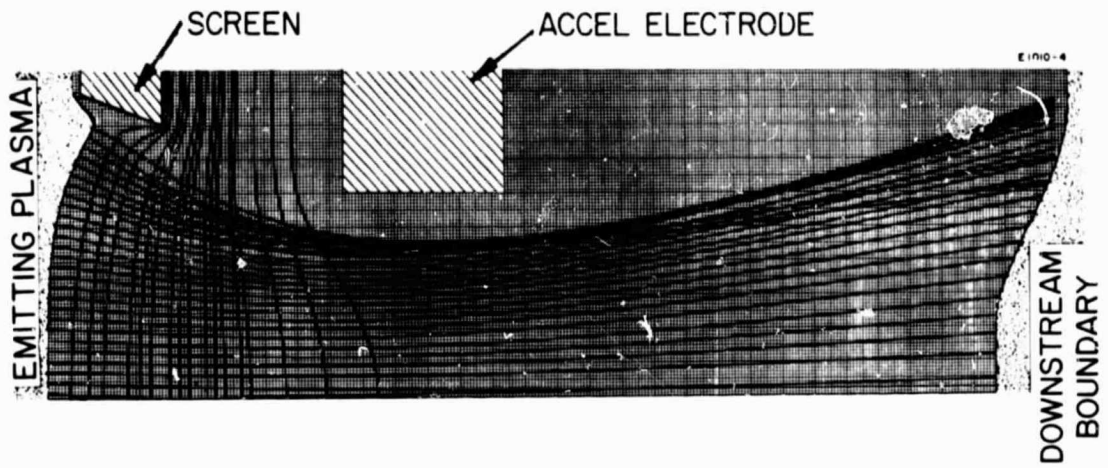
Fig. 6. Ion trajectories for case 2.
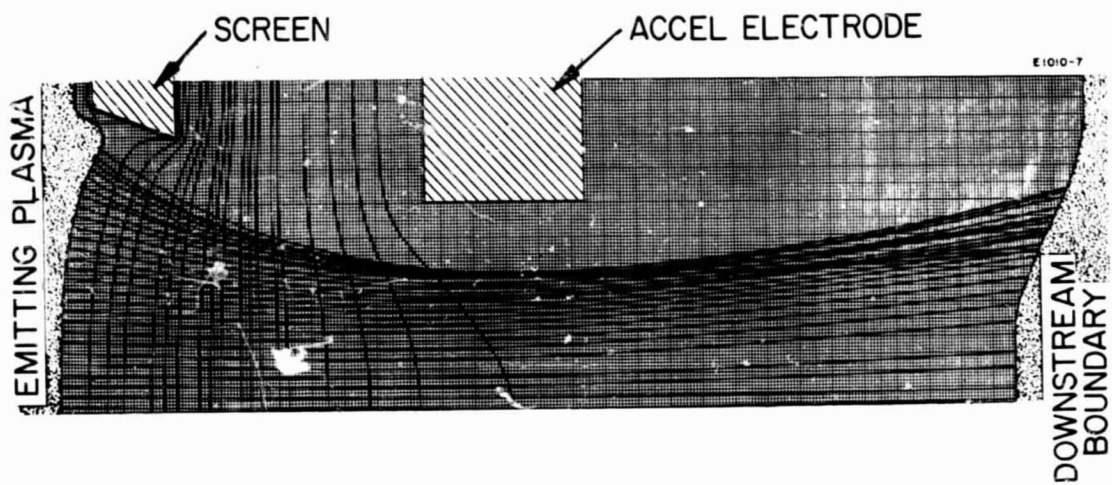
Fig. 7.   ion trajectories for case 3.
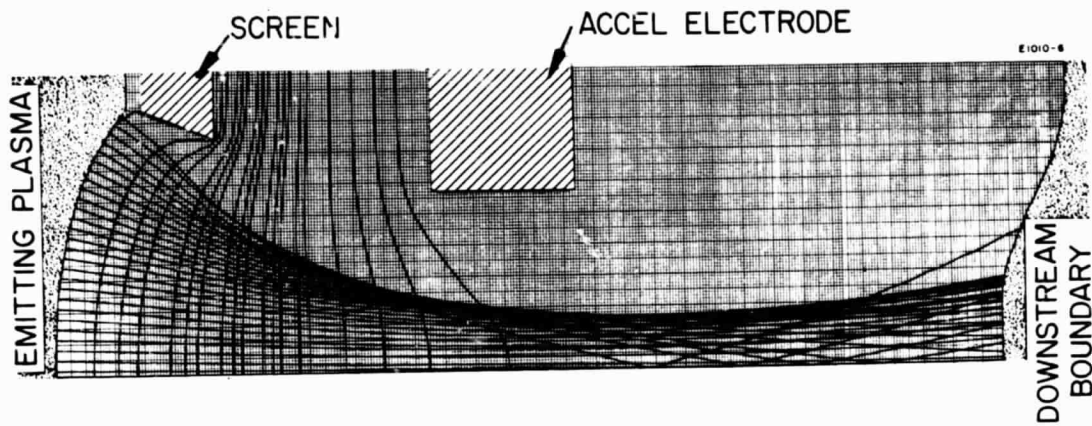
Fig. 8.   Ion trajectories for case 4.
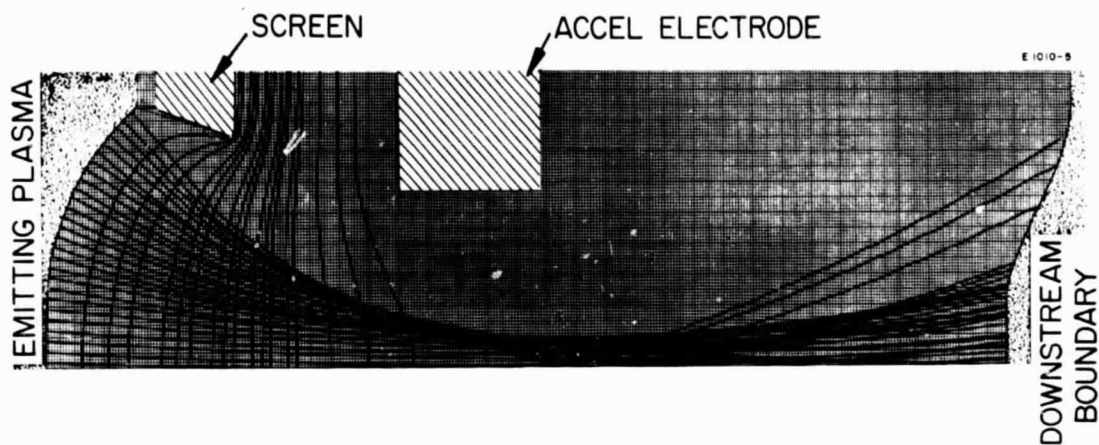
Fig. 9.   Ion trajectories for case 5.

27

TABLE I

Thrust Calculated for Electrode Configurations with Axial Symmetry in Unperturbed System

Case Number	Screen/ Accel Spacing, in.	Average Current Density,[a] mA/cm^2	Electron Perv $\times 10^{-6}$	Axial Thrust, $lb \times 10^{-5}$
Constant Ion Arrival Rate $\equiv 3.4 \times 10^{-6}$ electron perv				
1	0.090	7.87	3.4	2.503
2	0.070	8.87	3.83	2.829
Constant Ion Arrival Rate $\equiv 1.942 \times 10^{-6}$ electron perv				
3	0.090	4.5	1.942	1.502
Constant Ion Arrival Rate $\equiv 0.985 \times 10^{-6}$ electron perv				
4	0.090	2.28	0.985	0.821
5	0.070	2.56	1.105	0.887

[a] Evaluated at screen aperture.

TABLE II

Change in Thrust due to 0.020 in. Movement of Accel
Electrode in the Unperturbed System

Case Number	Axial Thrust, lb x 10^{-5}	$\delta T/T$, %	$\delta T_1/T$, %	$\delta T_2/T$, %	$\delta T_3/T$, %
Ion Arrival Rate $\equiv 3.4$ x 10^{-6} electron perv					
1^a	2.503	—	—	—	—
2	2.829	13	1.43	8.9	2.67
Ion Arrival Rate $\equiv 0.985$ x 10^{-6} electron perv					
4^a	0.821	—	—	—	—
5	0.887	8.0	3.4	4.5	0.1

[a]Considered as the unperturbed system.

The above analysis applies strictly to small perturbations only, since it assumes linearity neglecting products of first order terms. An estimate of the changes in thrust due to large reductions in ion arrival rate in the unperturbed electrode system can be obtained if we write

$$\delta T_A = K\sqrt{V} \left\{ \Sigma I_{i2} \cos (\phi_{i2}) - \Sigma I_{i1} \cos (\phi_{i1}) \right\}$$

$$= K\sqrt{V} \left\{ \Sigma (I_{i1} + \delta I_i) \cos (\phi_i + \delta\phi_i) - \Sigma I_{i1} \cos (\phi_{i1}) \right\}$$

and

$$\delta T_{A1} = K\sqrt{V} \Sigma \left\{ I_{i1} \cos (\phi_{i1} + \delta\phi_{i1}) - \cos (\phi_{i1}) \right\}$$

This assumes $\Sigma \delta I \cos (\phi_1 + \delta\phi) = \delta I \cos \phi_1$

$$\delta T_{A2} = \frac{\partial T}{\partial(\Delta A_s)} \, \delta(\Delta A_s)$$

$$\delta T_{A3} = \frac{\partial T}{\partial F_i} \, \delta F_i$$

$$\delta T_{A4} = \frac{\partial T}{\partial_j} \, \delta_j \quad .$$

The results broken down in this way for the three ion arrival rates are shown in Table III. (It can be seen that the error in this assumption is about 4%).

TABLE III

Thrust Calculated for Accelerator with Axial Symmetry

Case Number	Axial Thrust, lb x 10^{-5}	$\delta T/T$, %	$\delta T_1/T$, %	$\delta T_2/T$, %	$\delta T_3/T$, %	$\delta T_4/T$, %
1	2.503[a]	—	—	—	—	—
2	1.502	-40	2.9	8.6	2.7	-54.3
3	0.821	-67.2	5.2	14.	9.5	-71.3

[a] Considered as the unperturbed system.

From Fig. 10 it can be seen that the variation in thrust with emitted current is linear and hence

30

E1010-10
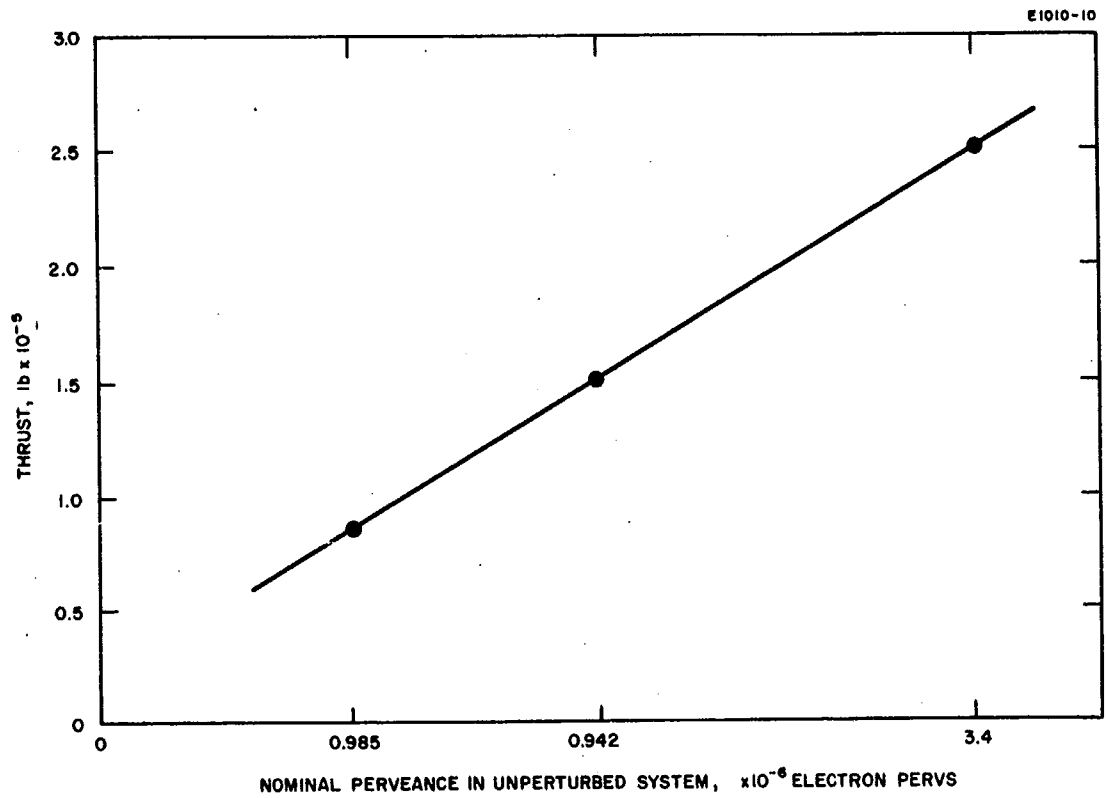
Fig. 10. Change in thrust due to ion arrival rate with constant screen to accel spacing of 0.090 in.

$$\frac{\partial T}{\partial \bar{j}} \equiv \frac{\text{change in thrust}}{\text{change in ion arrival}}$$

can be evaluated as

$$= 0.01725 \text{ mlb/mA} \; ;$$

similarly, the derivative

$$\left. \frac{dT(\%)}{dd} \right| \quad = \frac{\text{percentage change in axial thrust}}{\text{percentage change in electrode spacing}}$$

at constant
ion arrival
rate

$$= \Sigma \frac{\partial T_i}{\partial (\Delta A_i)} + \Sigma \frac{\partial T_i}{\partial F_i} + \Sigma \frac{\partial T_i}{\partial \phi_i}$$

can be evaluated for two ion arrival rates.

From Fig. 11 and 12 we see that

$$\left. \frac{dT(\%)}{dd} \right| \qquad = 0.103, \; \%/\text{mil}$$

at $P_o \equiv 3.4 \times 10^{-6}$
electron pervs

$$\left. \frac{dT(\%)}{dd} \right| \qquad = 0.419 \; \%/\text{mil} \; .$$

at $P_o \equiv 0.985 \times 10^{-6}$
electron pervs

From the above results it is possible to estimate the thrust T_A for small perturbations which preserve the axial symmetry of the system.

32
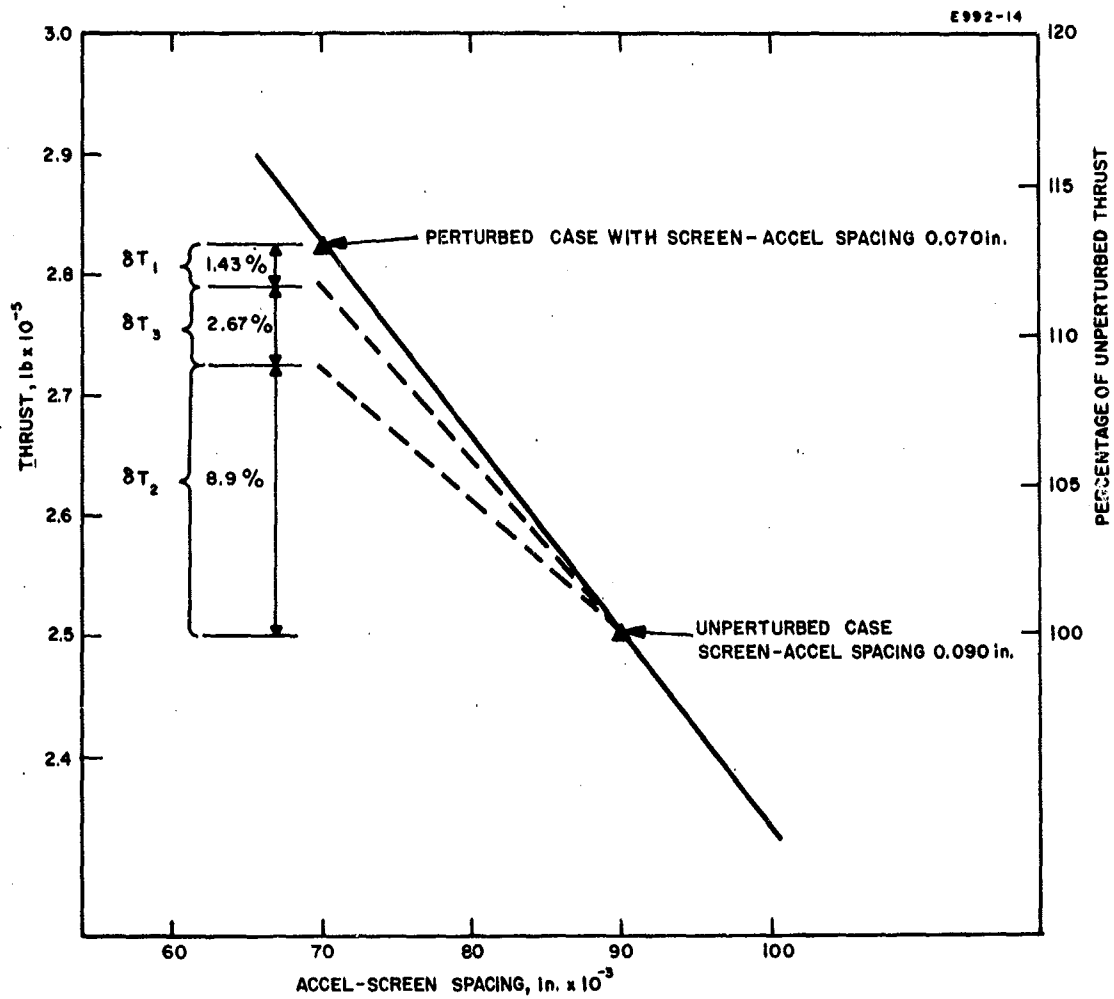
Fig. 11. Change in axial thrust with electrode spacing. δT_1 = change in axial thruster due to ion paths. δT_2 = change in axial thrust due to emitting area. δT_3 = change in axial thrust due to screen shielding.

33
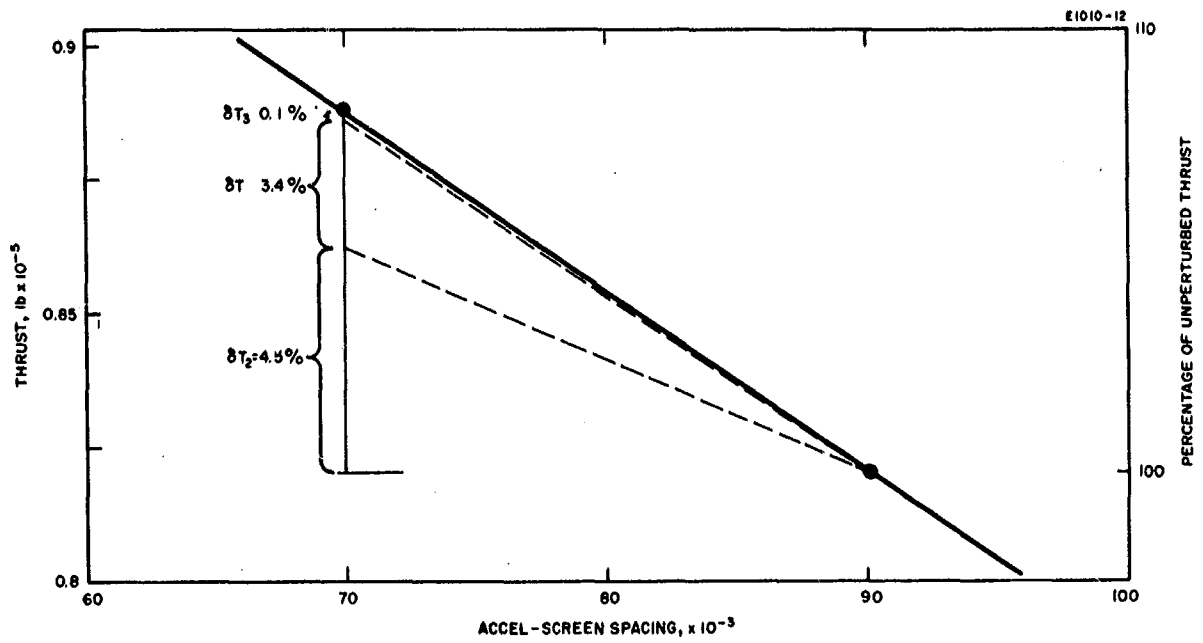
Fig. 12. Change in axial thrust with electrode spacing for system with nominal perveance of 0.985×10^{-6} electron pervs.

34

2. Transverse Displacements

When the accel-electrode is displaced transversely, the axis of symmetry of the aperture is destroyed; hence the ion motion cannot be solved assuming circular symmetry.

A transverse misalignment is illustrated in Fig. 13, where the axes of the screen electrode and the accel electrode are shown displaced by a distance ϵa (where a is the radius of the accel aperture).

The $R - \theta$ equation of the displaced surface can be found by expressing

$$R = x + iy \qquad (14)$$

where

$$x = a\cos \theta$$
$$y = \epsilon a + a \sin \theta \; ;$$

hence

$$R = (x^2 + y^2)^{1/2} \; , \qquad (15)$$

or to first order

$$R = (a^2 + 2\epsilon a^2 \sin \theta)^{1/2} \doteq a (1 + \epsilon \sin \theta) \; . \qquad (16)$$

It can thus be seen that this type of displacement introduces a perturbation in the radial coordinate R which varies as $\sin \theta$.

If two sections are drawn through the system normal to each other, representing the planes of least and greatest perturbations, the axis lines of the two electrodes will coincide in the first plane and be displaced by ϵa in the second plane. The trajectory equations can be solved as planar problems for these two cases and the results will

35
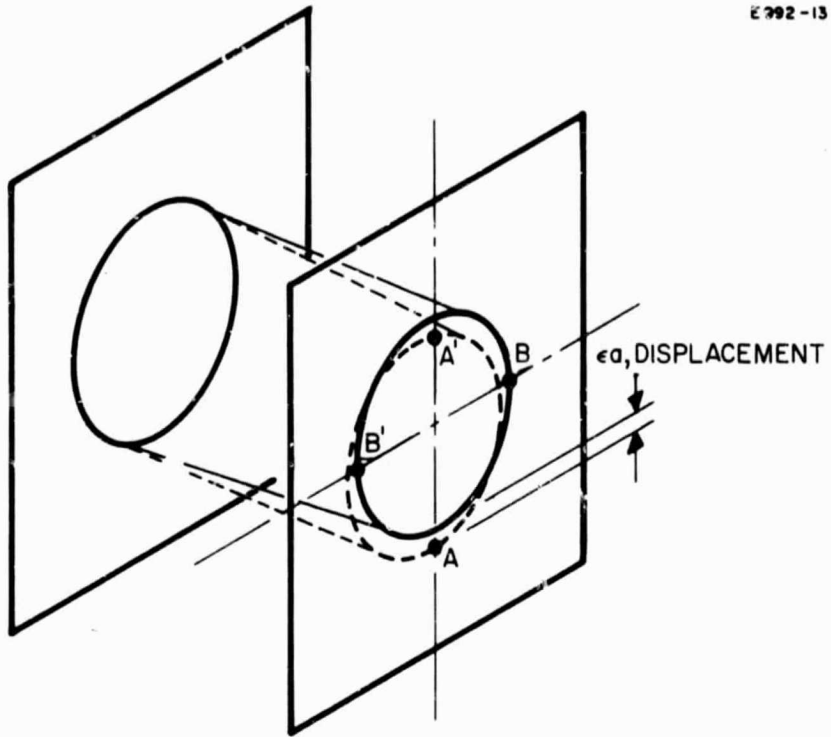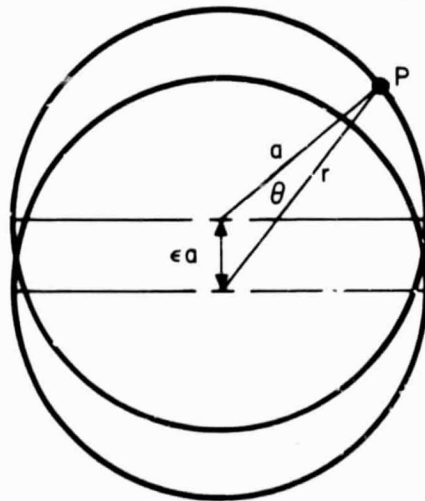
Fig. 13. Displacement of the accel electrode of ϵa normal to the axis of the unperturbed system.

be as illustrated in Fig. 14. It can be seen that the calculated trajectories will differ. The effect of this transverse displacement can be thought of as displacing each trajectory through an angle δ_i. Hence, for the trajectories nearest the screen the change in exit angle is δ_{27} at the top and δ_1 at the bottom.

If it is assumed that the change in exit angle varies as $\sin \theta$ in the azimuthal direction (as shown in Fig. 15), the angular displacement of the outermost trajectory in a plane at an angle $(\pi/2 - \theta)$ from the plane of the displacement can be written as

$$- \frac{1}{2} (\delta_1 + \delta_{27}) \sin \theta + \frac{1}{2} (\delta_1 - \delta_{27}) . \qquad (17)$$

Hence in a plane normal to the displacement where $\theta = 0$, the change in exit angle $\delta\phi_i$ is $1/2 (\delta_1 - \delta_{27})$. In the plane of the displacement at $\theta = \pi/2$, $\delta\phi_i = -\delta_{27}$; at $\theta = -\pi/2$, $\delta\phi_i = \delta_1$. Hence from a small element (shown in Fig. 20) where the current density is $\bar{j}_i$, the axial thrust is given by

$$\Delta T_{i, A} = \bar{j}_i \, \delta S_i \cos \phi_i' \, t_i \sqrt{V} \qquad (18)$$

where ϕ_i' is the exit angle $\delta S_i = R_i \, \delta\theta$

$\qquad R_i \equiv$ radial coordinate of the element

$\qquad \delta\theta \equiv$ angular width of the element.

Therefore,

$$\Delta T_{i, A} = R_i t_i \sqrt{V} \, \bar{j}_i \cos \phi_i' \, \delta\theta . \qquad (19)$$

Hence the total thrust from the annulus shown is

E992-12
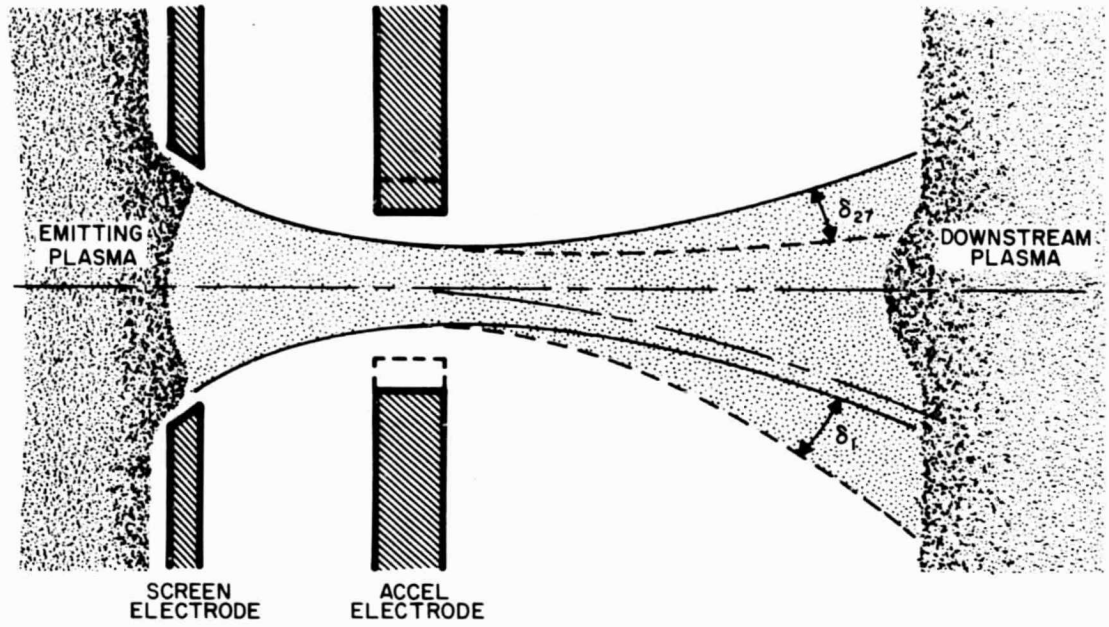
Fig. 14. Effect of translational misalignment of the ion paths calcu-
lated assuming planar symmetry (dotted lines represent
perturbed solutions).

38

M 6257
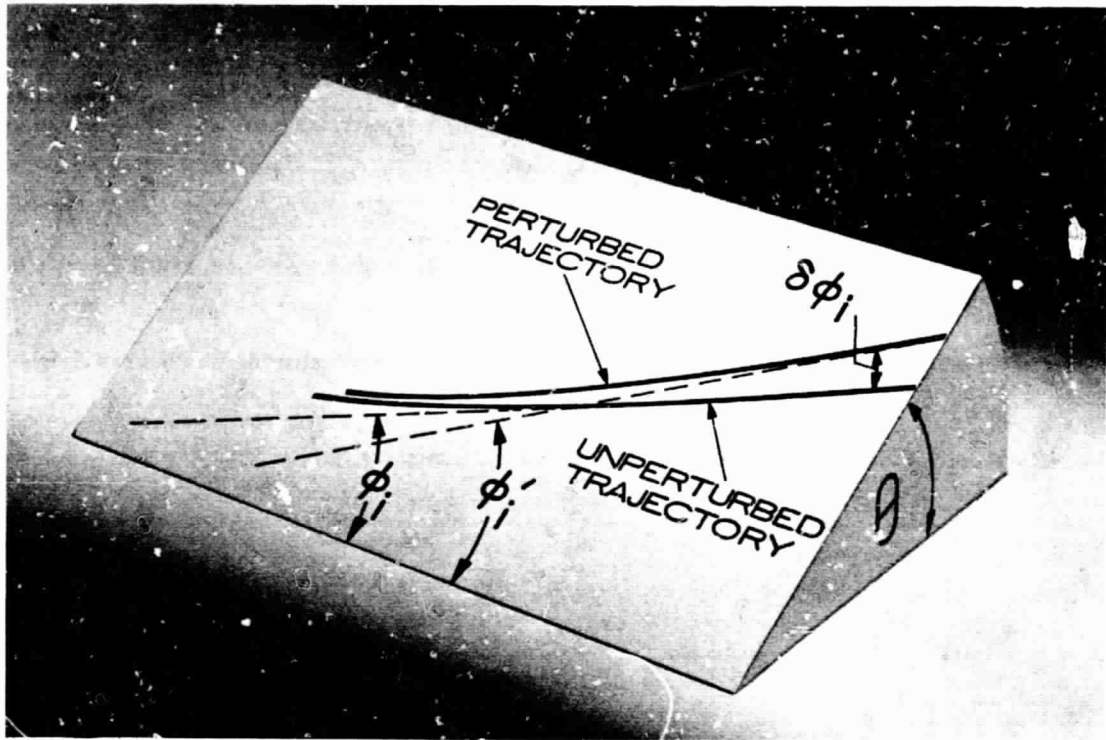
Fig. 15.   Three-dimensional representation of the perturbed and un-
perturbed trajectories.

$$T_{i, A} = \Sigma(R_i t_i \overline{j}_i) \sqrt{V} \cos \phi_i{}' \, \delta\theta \quad . \tag{20}$$

In this equation we can write $J_i \delta\theta = R_i t_i \overline{j}_i \, \delta\theta$. J_i is the current per radian in the ith trajectory; therefore, $J_i \delta\theta$ is the current contained in an element of the ith trajectory subtended by an angle $\delta\theta$ at the axis. Hence $I_i = \Sigma J_i \, \delta\theta$. Since boundary conditions for the upstream plasma are that the emission density be equivalent to the ion arrival rate at the surface and that the ion density be assumed constant across a single aperture, it can be shown that variations in J_i with θ will produce at most second order perturbations in the thrust. (Variations in J_i will be produced by variations in the shielding effect of the screen electrode only because of the asymmetry of the upstream boundary.) Hence $J = (I_i/2\pi)$. In (20),

$$\phi_i{}' = \phi_i - \frac{1}{2} (\delta_i + \overline{\delta}_i) \sin \theta + \frac{1}{2} (\delta_i - \overline{\delta}_i) \tag{21}$$

where

$$\phi_i \equiv \text{exit angles for the unperturbed axisymmetric run}$$

$$\delta_i \equiv \text{maximum positive angular displacement}$$

$$\overline{\delta}_i \equiv \text{maximum negative angular displacement.}$$

Hence

$$T_i = \frac{I_i \sqrt{V}}{2\pi} \int_0^{2\pi} \cos \left\{ \phi_i + \frac{(\delta_i - \overline{\delta}_i)}{2} + \frac{(\delta_i + \overline{\delta}_i)}{2} \sin \theta \right\} d\theta$$

$$= \frac{I_i \sqrt{V}}{2\pi} \left[\cos \left(\phi + \frac{\delta_1 - \overline{\delta}_i}{2} \right) \int_0^{2\pi} \cos \left(\frac{(\delta_i + \overline{\delta}_1)}{2} \sin \theta \right) d\theta \right.$$

$$\left. - \sin \left(\phi + \frac{\delta_1 - \overline{\delta}_i}{2} \right) \int_0^{2\pi} \sin \left(\frac{\delta_i + \delta_1}{2} \sin \theta \right) d\theta \right] \quad . \tag{22}$$

40

However,

$$\int_0^{2\pi} \cos\left(\left(\frac{\delta_1 + \delta_i}{2}\right) \sin \theta\right) d\theta = 2\pi \, J_0\left(\frac{\delta_i + \overline{\delta}_i}{2}\right)$$

where J_0 is the Bessel function of order zero and

$$\int_0^{2\pi} \sin\left(\frac{\delta_i + \overline{\delta}_i}{2} \sin \theta\right) d\theta = 0 \quad .$$

Hence

$$T_i = I_i \sqrt{V} \, J_0\left(\frac{\delta_i + \overline{\delta}_i}{2}\right) \cos\left(\phi_i + \frac{\delta_i - \overline{\delta}_i}{2}\right) . \tag{23}$$

The total perturbed axial thrust is therefore given by

$$T_0 = \Sigma I_i \sqrt{V} \, J_0\left(\frac{\delta_i + \overline{\delta}_i}{2}\right) \cos\left(\phi_i + \frac{\delta_i - \overline{\delta}_i}{2}\right) . \tag{24}$$

The self-consistent ion trajectories solved assuming a 0.0142 in. transverse displacement and planar symmetry and a normal ion arrival rate equivalent to a perveance of 3.4 μpervs are shown in Fig. 16. A self-consistent upstream boundary was found for each case. It can be seen that the beam is deflected in an opposite direction to the perturbation, and that the two beam edges are moved in this direction by approximately equal amounts. This result is in agreement with previous work.[3] The angular deflection at the edges is about 4°; hence for the beam edge the angular deflection can be calculated to be 0.028°/mil. However, the mean angular deflection $\overline{\delta\phi}_i$ is calculated as

$$\overline{\delta\phi}_i = \sum_i^N \frac{(\delta\phi_i)}{N}$$
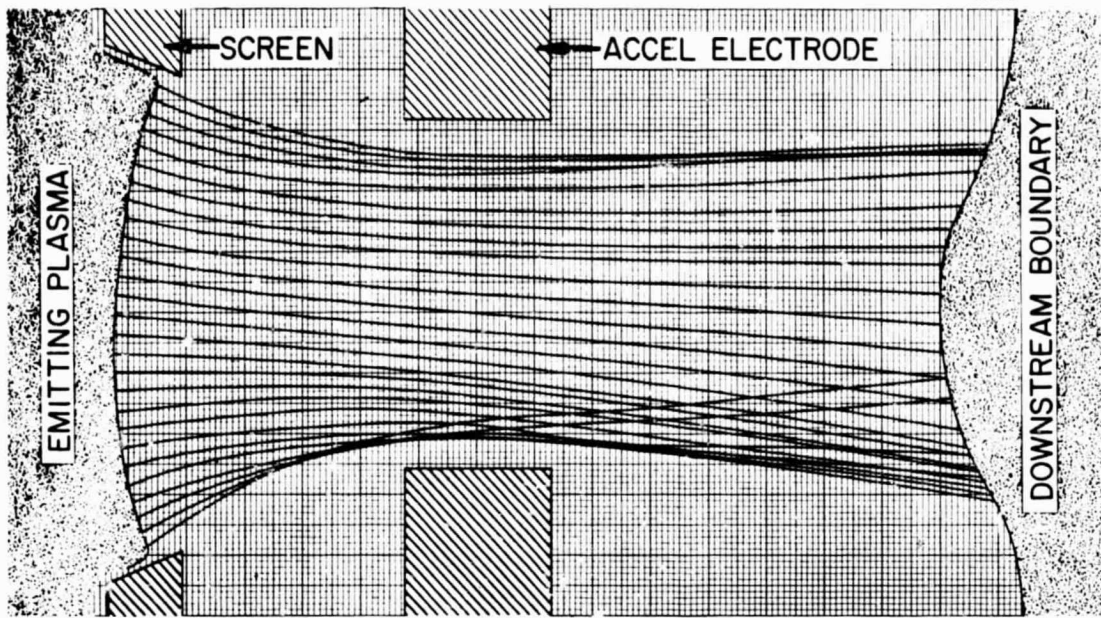
Fig. 16.   Ion trajectories calculated assuming planar symmetry for case 6.

where

$$N \equiv \text{number of trajectories}$$

$$= 8.2^{\circ} .$$

Hence if it is assumed that the mean angular deflection is a linear function of transverse displacement of the accel electrode, the proportionality constant can be calculated as $0.578^{\circ}/\text{mil}$. In metric units this is equivalent to $23.2^{\circ}/\text{mm}$, which compares with a value of $29^{\circ}/\text{mm}$ reported by other workers.[4] This difference can be explained by a number of factors. The geometry and voltages assumed in this case are somewhat different. Thus the lens produced in our geometry is slightly stronger (which tends to reduce the divergence) and in previous work no account was taken of the relocation of the emitting plasma caused by the electrode perturbation; in addition, the correct position of the downstream boundary was not determined.

If the total thrust is calculated using for this case

$$T = \Sigma I_i \sqrt{V} \, J_0 \left(\frac{\delta_i + \overline{\delta}_i}{2} \right) \cos \left(\phi_i + \frac{\delta_i - \overline{\delta}_i}{2} \right) ,$$

a value of 2.472×10^{-5} lb is obtained.

The transverse thrust $\overrightarrow{T}'$ is a vector which can be represented by its components T'_1 and T'_2 where T'_1 is the component of thrust parallel to the displacement ϵa and T'_2 is the component normal to it. Then

$$T'_1 = \Sigma \int_0^{2\pi} \frac{I_i}{2\pi} \sqrt{V} \sin \phi'_i \sin \theta d\theta \qquad (25)$$

and

$$T'_2 = \Sigma \int_0^{2\pi} \frac{I_i}{2\pi} \sqrt{V} \sin \phi'_i \cos \theta d\theta \qquad (26)$$

43

where $\phi_i' = \phi_i + (1/2)(\delta_i + \overline{\delta}_i)\sin\theta + (1/2)(\delta_i - \overline{\delta}_i)$ and the summation is for $i = 1$ to 27.

We can write

$$T_1' = \Sigma \int_0^{2\pi} \frac{I_i}{2\pi} \sqrt{V} \left\{ \sin\left(\phi_i + \frac{\delta_i - \overline{\delta}_i}{2} \cos\left(\frac{\delta_i + \overline{\delta}_i}{2} \sin\theta\right)\right) \right.$$

$$\left. + \cos\left(\phi_i + \frac{\delta_i - \overline{\delta}_i}{2} \sin\left(\frac{\delta_i + \overline{\delta}_i}{2} \sin\theta\right)\right) \right\} \sin\theta\, d\theta \qquad (27)$$

and

$$T_2' = \Sigma \int_0^{2\pi} \frac{I_i}{2\pi} \sqrt{V} \left\{ \sin\left(\phi_i + \frac{\delta_i - \overline{\delta}_i}{2}\right) \cos\left(\frac{\delta_i + \overline{\delta}_i}{2} \sin\theta\right) \right.$$

$$\left. + \cos\left(\phi_i + \frac{\delta_i - \overline{\delta}_i}{2}\right) \sin\left(\frac{\delta_i + \overline{\delta}_i}{2} \sin\theta\right) \right\} \cos\theta\, d\theta \qquad (28)$$

Noting that

$$\int_0^{2\pi} \sin\left(\frac{1}{2}(\delta_i + \overline{\delta}_i)\sin\theta\right)\cos\theta = 0$$

$$\int_0^{2\pi} \sin\left(\frac{1}{2}(\delta_i + \overline{\delta}_i)\sin\theta\right)\sin\theta = 2\pi J_1\left(\frac{\delta_i + \overline{\delta}_i}{2}\right)$$

$$\int_0^{2\pi} \cos\left(\frac{1}{2}(\delta_i + \overline{\delta}_i)\sin\theta\right)\cos\theta = 0$$

$$\int_0^{2\pi} \cos\left(\frac{1}{2}(\delta_i + \overline{\delta}_i)\sin\theta\right)\sin\theta = 0 \quad , \qquad (29)$$

44

we can write

$$T'_1 = \Sigma I_i \sqrt{V} \, \cos \left(\phi_i + \frac{\delta_i - \bar{\delta}_i}{2} \right) J_1 \left(\frac{\delta_i + \bar{\delta}_i}{2} \right) \qquad (30)$$

$$T'_2 = 0. \qquad (31)$$

The values of thrust have been calculated for both a 0.0142 in. and a 0.0071 in. transverse displacement of the accel electrode for two values of ion arrival rate. The ion trajectories calculated are shown in Figs. 16 to 19. The results are given in Table IV and are illustrated in Figs. 20, 21, and 22.

TABLE IV

Thrust Calculated for Accelerator with Transverse Perturbations

Case Number	Nominal Perveance, Electron Pervs	Transverse Perturbation of Accel x 0.001 in.	$\overline{\delta\phi}_2$ Average Deflection, deg	Axial Thrust, lb	Transverse Thrust, lb	Rotation of Thrust Vector, deg
6	3.4×10^{-6}	0.0071	4.13	2.487×10^{-5}	1.278×10^{-6}	2.94
7	3.4×10^{-6}	0.0142	8.2	2.472×10^{-5}	2.529×10^{-6}	5.84
8	0.985×10^{-6}	0.0071	4.49	8.12×10^{-6}	3.573×10^{-7}	2.52
9	0.985×10^{-6}	0.0142	8.8	8.032×10^{-6}	7.085×10^{-7}	5.04

It can be seen that for the ranges of displacement considered the change in thrust is a linear function of the electrode spacing.

3.   Tilt

For an engine with a diameter of 30 cm and a spacing between the screen and accel electrode of 0.090 in., the maximum angle for gross tilt is of the order of $\tan^{-1} 0.007$. This is equivalent to an angle of about $0.4°$. (However, localized warping could increase the angle to some extent.) A case has been run with a symmetric tilt of $1.5°$ about the unperturbed center line. This produces a maximum
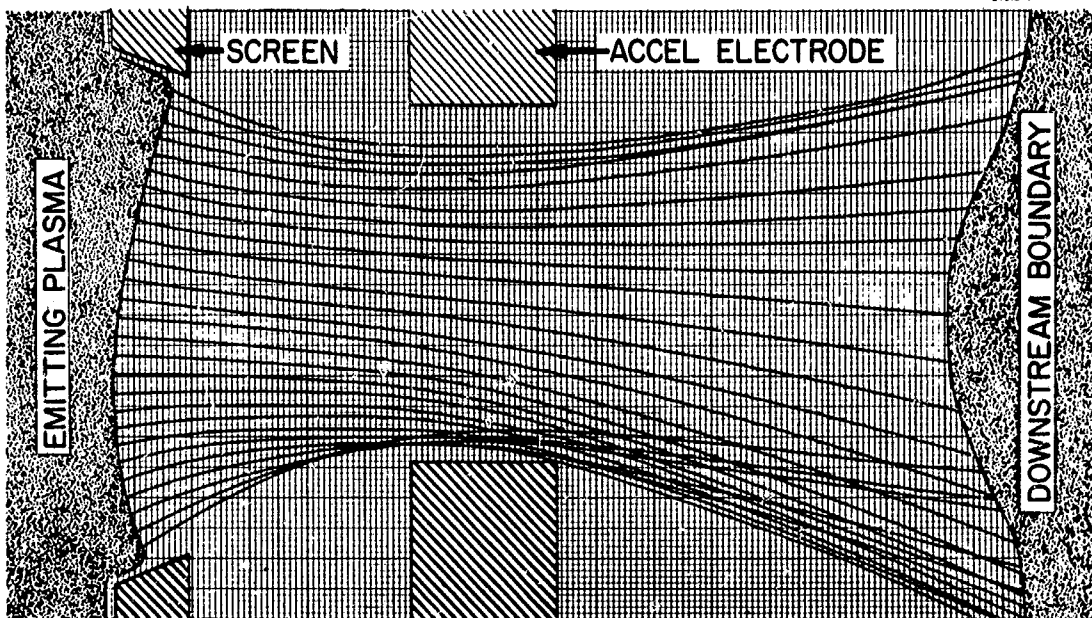
Fig. 17.   Ion trajectories calculated assuming planar symmetry for case 7.
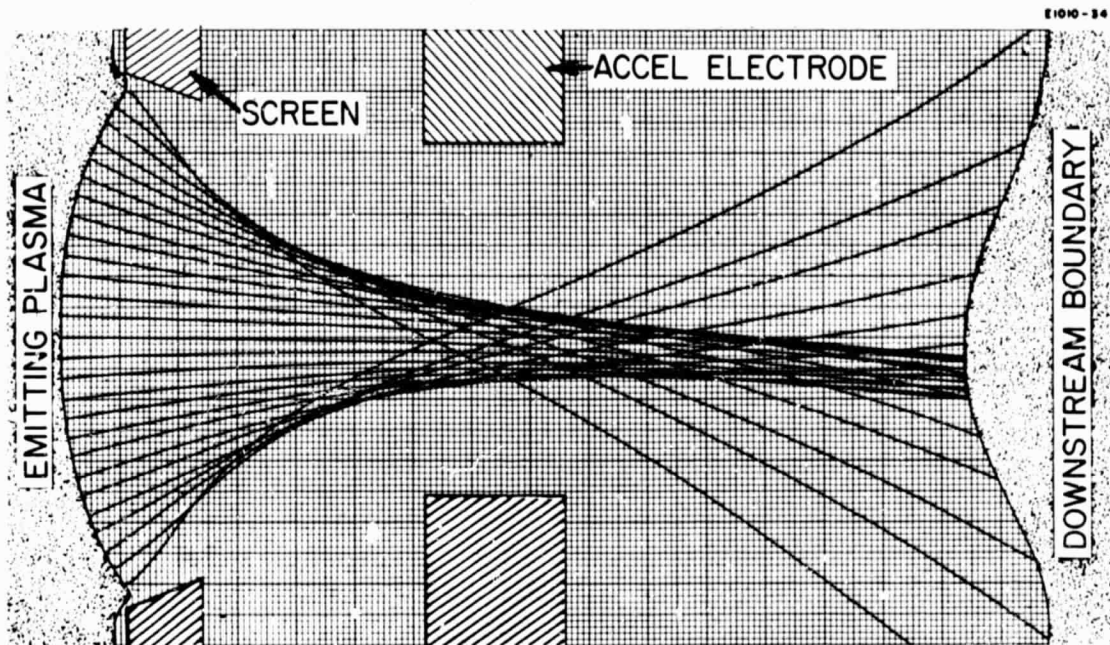
Fig. 18.   Ion trajectories calculated assuming planar symmetry for
            case 8.

47
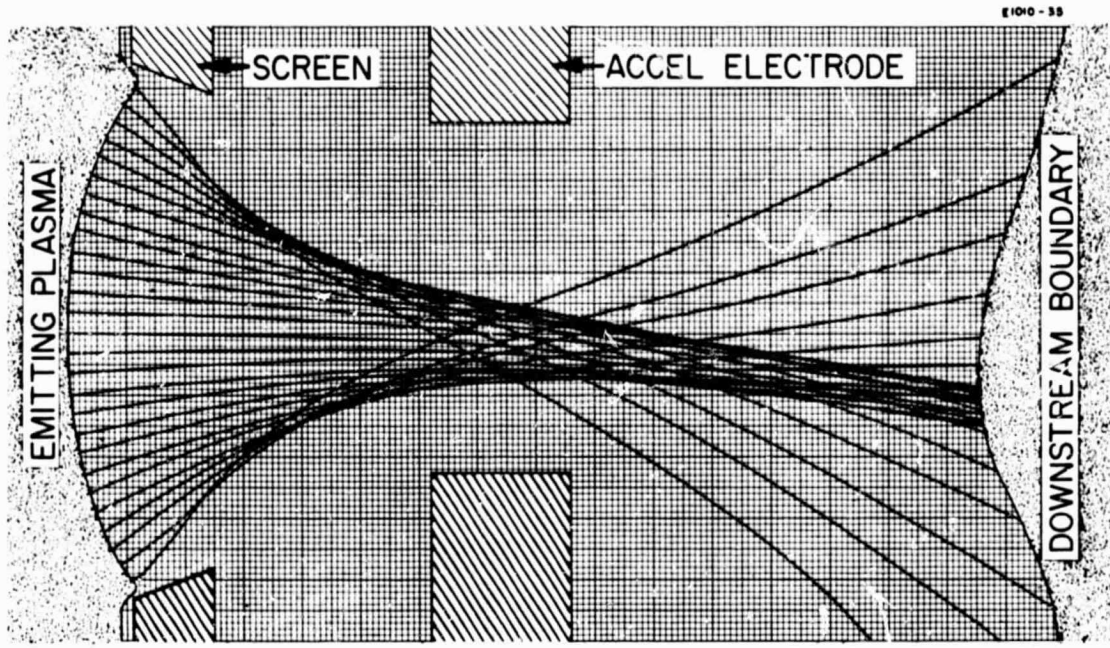
Fig. 19.   Ion trajectories calculated assuming planar symmetry for
            case 9.
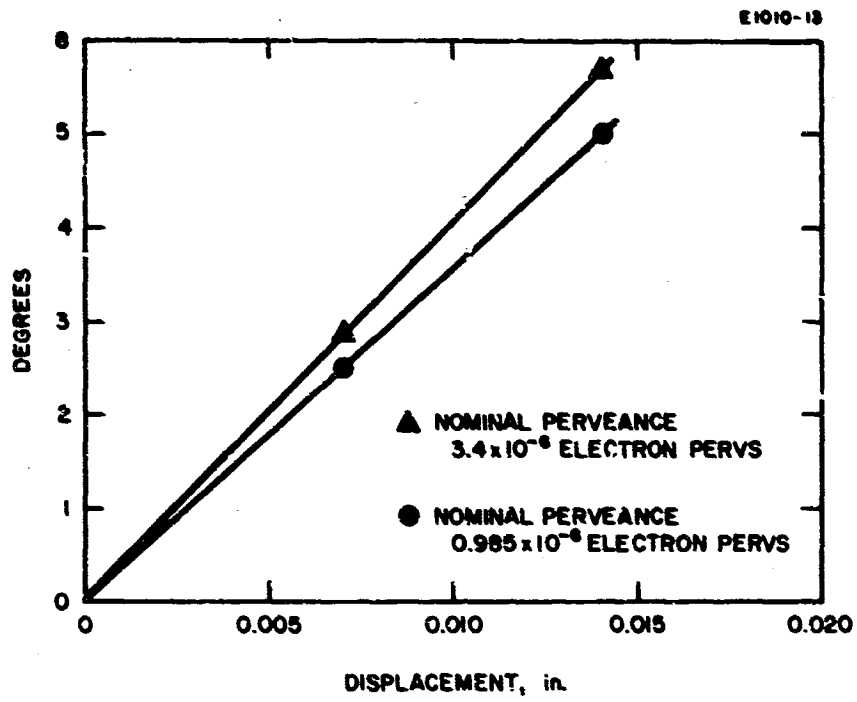
Fig. 20.   Rotation of thrust vector due to transverse
            displacement of accel electrode.
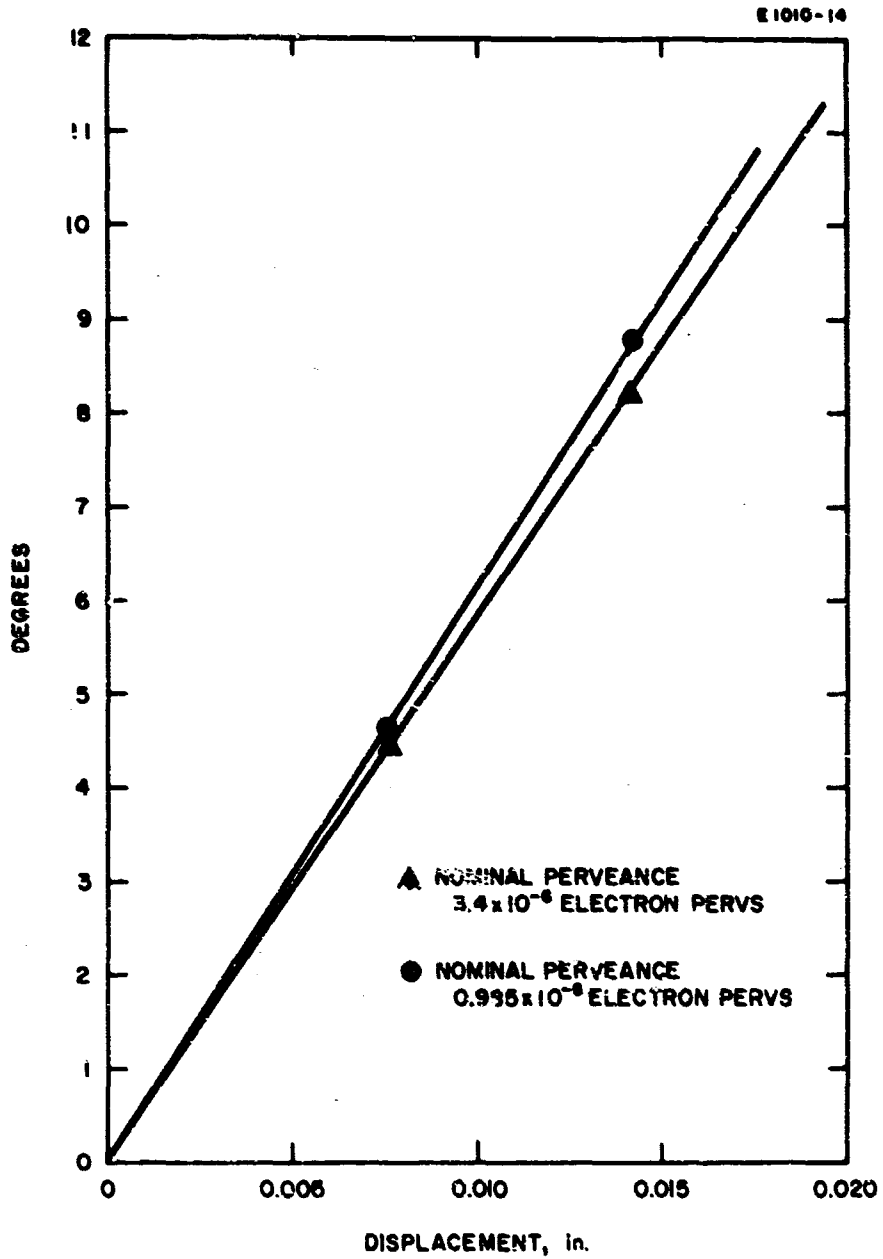
Fig. 21.   Mean angular displacement of ion trajectories
due to transverse displacement.

50
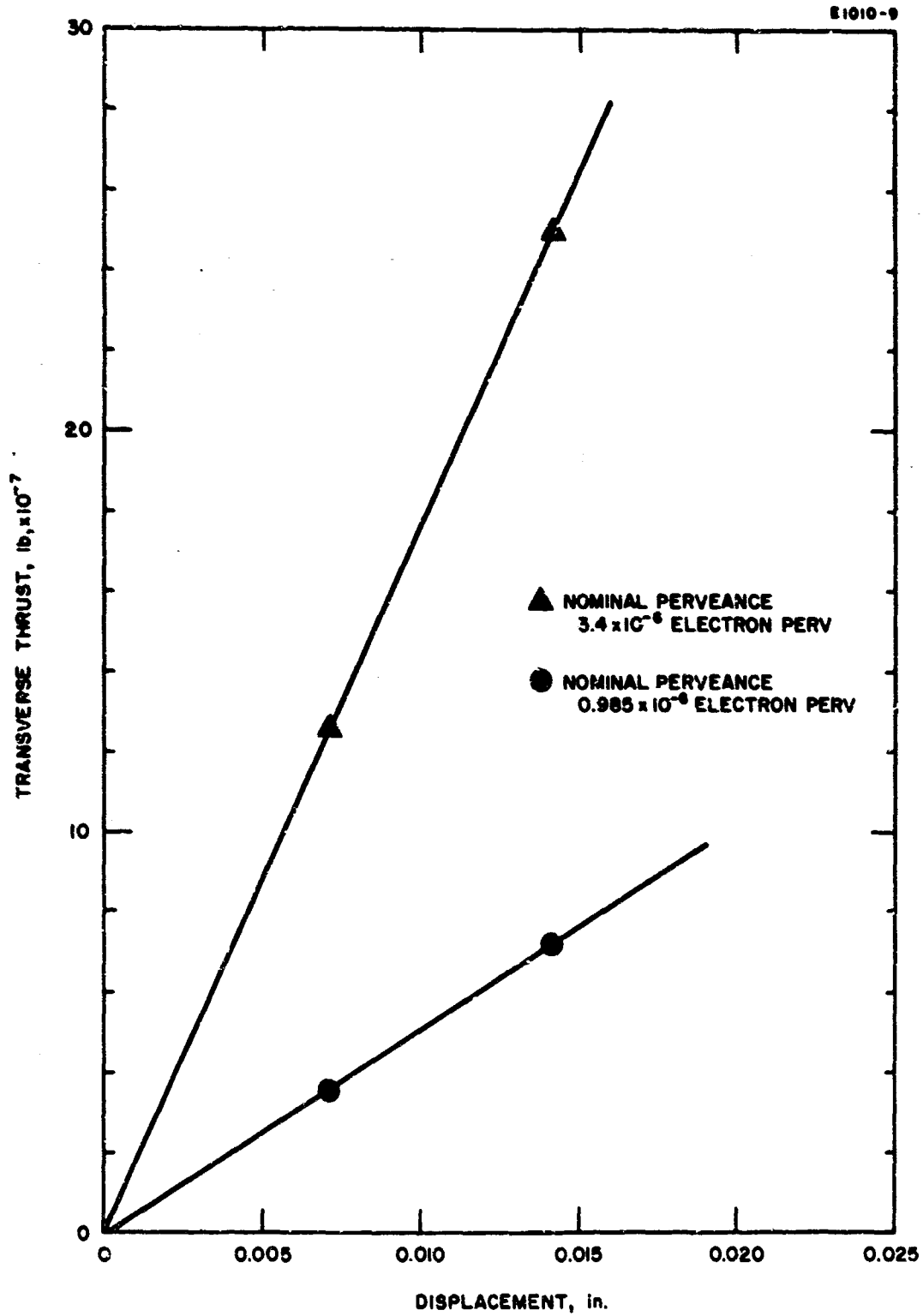
Fig. 22.   Transverse thrust due to displacement of accel electrode.

displacement of the accel-electrode of 0.002 in. The results from this run show no significant change in ion optics or emission density. This is in general agreement with the other reported work,[4] where it was found that for tilt angles of less than 5° no meaningful results could be obtained since the small calculated beam deflection approaches the accuracy of the computer program.

However, tilt may be a significant factor at the edge of the engine where the displacement of the accel-electrode can be regarded as a combination of an axial movement and a tilt. In this case a satisfactory solution can be found by considering the appropriate axial displacement alone.

D. Conclusions

The ion optics have been solved self-consistently for ten different configurations and the total thrust from a single aperture calculated for each. The thrust from the unperturbed system with a nominal perveance of 3.4×10^{-6} electron pervs was calculated to be 2.503×10^{-5} lb. Three types of perturbation have been considered: (1) changes in ion emission rate, (2) changes in the axial spacing of the electrodes, and (3) transverse misalignments. The first two types can be solved directly since they both possess axial symmetry. The third type produces a disturbed flow about a curvilinear axis and cannot be solved precisely by presently known techniques. A first order solution has been formed for this.

It has been found that changes in thrust due to perturbations which preserve the axial symmetry result primarily from the relocation of the emitting plasma, and the influence of ion optics has been found to be small. However, for the transverse misalignments considered (0.0071 in. and 0.0142 in.), the effect of the upstream boundary movement is small and the change in ion optics is more significant.

The results can be expressed in terms of the parameters defined below.

52

$$\alpha\Big|_P = \frac{\text{change in axial thrust}}{\text{change in axial spacing of electrodes}}$$

at constant ion emission rate equivalent to an electron perveance of P

$$\beta = \frac{\text{change in axial thrust}}{\text{change in emitted current}}$$

$$\gamma\Big|_P = \frac{\text{change in axial thrust}}{\text{transverse displacement of accel}}$$

at constant ion emission rate equivalent to an electron perveance of P

$$\eta\Big|_P = \frac{\text{change in transverse thrust}}{\text{transverse displacement of accel}}$$

at constant ion emission rate equivalent to an electron perveance of P

$$\omega\Big|_P = \frac{\text{rotation of thrust vector}}{\text{transverse displacement of the accel}}$$

at constant ion emission rate equivalent to an electron perveance of P

The values derived for the above constants are given in Table V. These values will be used in Section IV, together with the calculated magnitudes of electrode displacement, to provide the estimated total thrust vector variation of a single thruster.

TABLE V

Parameters Defining Change in Thrust Vector for Various Perturbations

P (Nominal Perveance). Electron Pervs	$\alpha\big|_{P'}$ lb/0.001 in.	β, lb/mA	$\gamma\big|_P$ lb/0.001 in.	$\eta\big|_P$ lb/0.001 in.	$\omega\big|_P$ deg/0.001 in.
3.4×10^{-6}	-1.63×10^{-7}	1.765×10^{-5}	2.18×10^{-8}	-1.78×10^{-7}	0.411
0.985×10^{-6}	-0.33×10^{-7}	0.684×10^{-5}	1.26×10^{-8}	-0.498×10^{-7}	0.354

53

III. CAUSES AND MAGNITUDES OF ELECTRODE MISALIGNMENT

A. Introduction

Under ideal conditions the geometric composition of a Kaufman thruster may be described as an arrangement of right circular cylinders. The main thrust axis is defined by the large cylindrical discharge chamber with the circular electrodes lying in parallel planes at one end. Thousands of hole pairs in the electrodes, located symmetrically about the thrust axis, form an array of small cylindrical accelerating structures whose axes are all aligned parallel to the thrust axis. The over-all thrust vector produced passes precisely through the geometric center of the electrodes and is parallel to the common axes of all the cylinders; no torques are produced about any axis. An additional assumption required for this ideal thruster operation is that the ion density in the discharge chamber be axisymmetric. If this assumption is violated or if any of the aligned cylindrical geometries become disturbed, perturbations in the thrust vector will be incurred.

Of the many possible causes of thrust vector perturbation it is reasonable to study those which are most likely to occur and which produce the largest thrust disturbances. Some detailed design aspects of the Kaufman thruster, such as discharge chamber layout or electrode support structure, could lead to thrust vector perturbations (due to nonsymmetric discharge profiles or motions of the electrodes). However, these design aspects are now under investigation and a detailed analysis of their causes and magnitudes would be premature at this time. Instead, the thrust vector disturbances produced in these cases are analyzed so that tolerance can be specified for the current design efforts.

The cause of thrust vector perturbation which was analyzed in sufficient detail for quantative prediction is the thermal buckling of the electrodes. In contrast to many other causes of thrust vector disturbance, the misalignments in the grid system which result from heating (an assembly initially aligned at room temperature) to operating

temperatures are inherent in the basic thruster design. The largest and most often observed thermal electrode motion is axial displacement (bowing). Because of the frequent occurrence and seriousness of the buckling problem in operating thrusters, electrodes are usually given an initial bow so that the direction of subsequent motion will be determined and preset to coincide. One may suspect that axial displacements equal to half the initial grid spacing are common. It will be shown in the subsequent sections that a spacing change from a uniform 0.090 in. to a parabolic distribution, which varies from 0.090 in. at the edge to 0.045 in. at the center, will cause an 18% change in thrust magnitude.

Although electrode spacing changes will be the only cause of misalignment that will be modeled analytically, the thrust vector perturbations caused by a number of modes of electrode misalignment are evaluated for thrust vector disturbance.

The thermal buckling analysis is presented in its two main parts: (1) the thermal analysis leading to the grid system temperature distributions, and (2) the stress analysis of the mechanically loaded electrodes with given temperature distribution.

These analyses will yield the expected electrode perturbations, which will be combined (in Section IV) with the coefficients, relating the thrust vector to electrode displacement, to give the expected thrust vector variation.

B.   Thermal Simulation of the Grid System

In order to provide a guide to initial thrust analysis, before a thermal simulation of the grid system was attempted, temperature distributions were measured on a thermal mockup of a bombardment thruster. A schematic drawing of the mockup is shown in Fig. 23. Each spot represents the location of one of the 24 thermocouples. The heat sources were simulated by heating coils located at the front of anode A, over the remaining anode surface B, and at the cathode
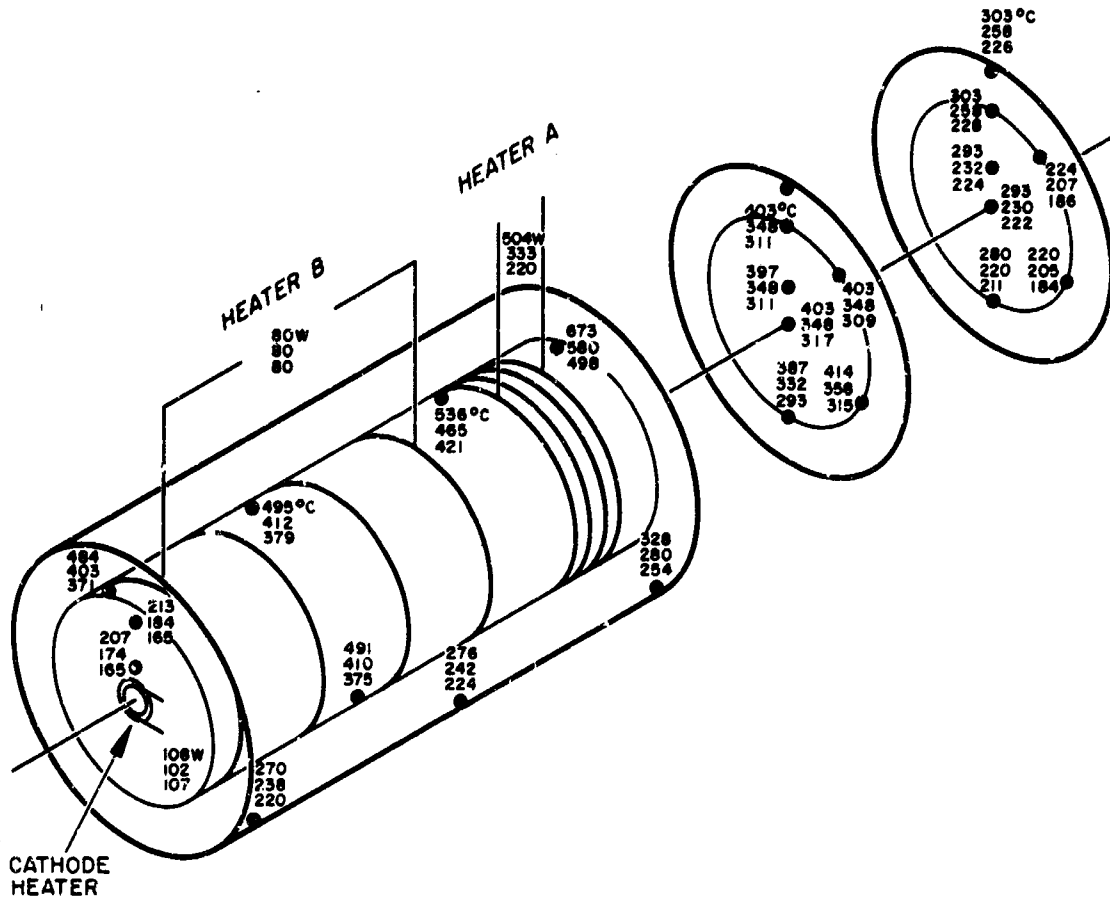
Fig. 23. Thermal mockup of electron bombardment thruster.

57

position. Three temperature distributions were measured for various combinations of input heater powers, with the mockup in a vacuum tank. Typical data are also shown in Fig. 23.

Efforts to predict these data by using analytical models based on nonreflective radiative transfer were unsuccessful. Upon further consideration of the data (particularly the rather uniform equilibrium temperature distributions across the electrodes), it was suspected that a large number of multiple reflections occur inside the discharge chamber; accordingly, the heat flux distribution across the screen electrode is fairly uniform. Because it was recognized that a difficult multiple reflection radiation problem was at hand, the simulation was directed toward a detailed analysis of the grid system only, under the assumption of various incident heat flux distributions from the discharge chamber.

The multiple reflection heat transfer in the grid system was simulated by the existing thermal analysis computer program TAS-1B. This is a digital computer program solves for the steady-state temperature distribution in a lumped parameter network of temperature points (nodes) and heat flow paths (resistors). A node is provided for each constant temperature portion of the device being modeled. The network may contain up to 80 nodes and each node may be connected to any or all of the others. Any two nodes may be connected by two resistors. One represents conduction and/or convection; the other represents infrared radiation. In addition to interchanging heat with other nodes, each node may receive radiation and/or a direct heat input (such as from internal dissipation of electrical energy).

Considerable effort was devoted to formulating a thermal network for the two perforated electrodes. The definition of nodes and the subsequent calculation of their view factors and thermal conductivities is discussed below in Section III-B-1. In Section III-B-2 a parametric study is given of electrode temperature distributions which are calculated from the thermal simulation.

58

1.   Network Model

A thermal model of the grid system was developed in the form of a network of nodes, each of which corresponds to a constant temperature region on an electrode. For axisymmetric heating the nodes N_i and N_i' are washer shaped (annuli) regions on the electrodes (see Fig. 24). Heat is transferred between adjacent washers of each electrode by conduction and between opposite washers of the two electrodes by radiation. An additional constant temperature node N_B, which represents the background, absorbs heat radiated directly from the accelerator electrode and from the screen electrode by way of the holes in the accelerator electrode. The heat input to the grid system from the discharge chamber is represented by a distribution of black body radiation which is incident on screen electrode and varies radially in intensity. The thermal network corresponding to this model is shown in Fig. 25. The node N_B is fixed at a constant temperature (0°F in our examples) and is assumed to be a black body ($\epsilon = 1$) whose area is much larger than any other node. Under these assumptions N_B may be regarded as a heat sink. For given values of incident heat flux Q_i, the temperatures of the other nodes N_i, N_i' can be calculated once the node coupling by the conductance paths $C(i, j)$ and radiation paths $R(i, j)$ is established. The evaluation of the thermal conductivities between the nodes of the model is straightforward and will be considered first. The evaluation of the geometric (view) factors which govern the radiative heat transfer in the model is more complicated; only a brief discussion will be given which is based on the detailed view factor calculations in Appendix I.

a.   Heat Conductance in the Electrodes — The temperature of a (washer shaped) node on an electrode shown in Fig. 26(a) will be taken as the value of the temperature at the circle halfway between the edges of the washer. Thus, the temperatures of nodes N_1, N_2, and N_3 are taken at the locations R_1, R_2, and R_3. The thermal conductance between nodes N_i and $N_i + 1$ is then equal to the conductance between the
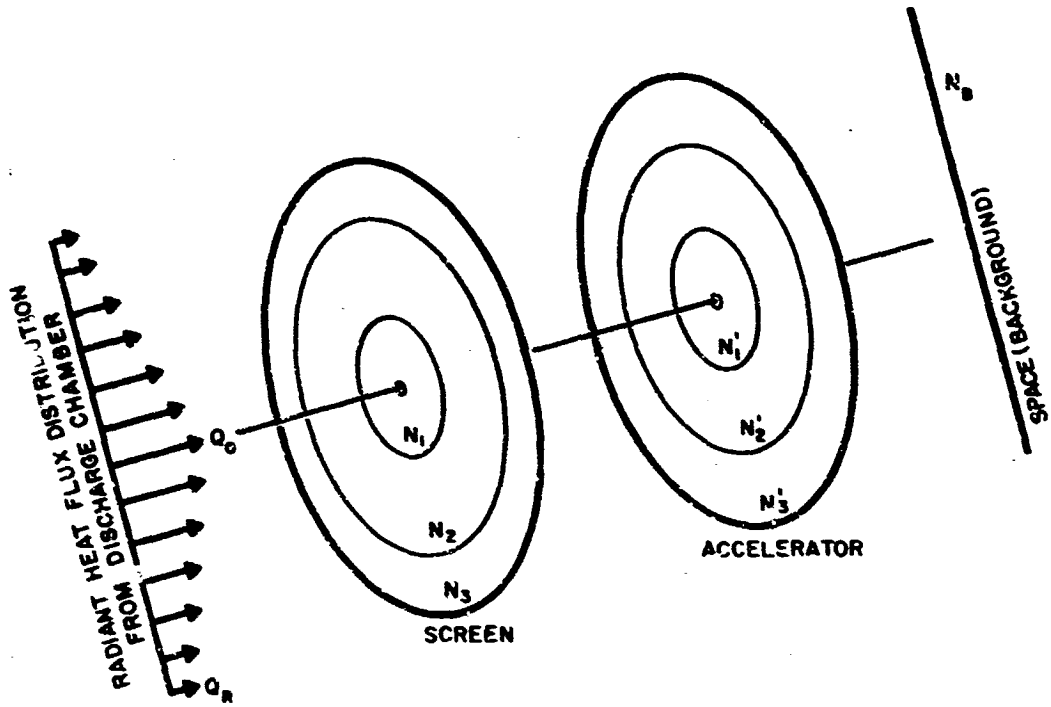
Fig. 24. Model for electrode thermal analysis.
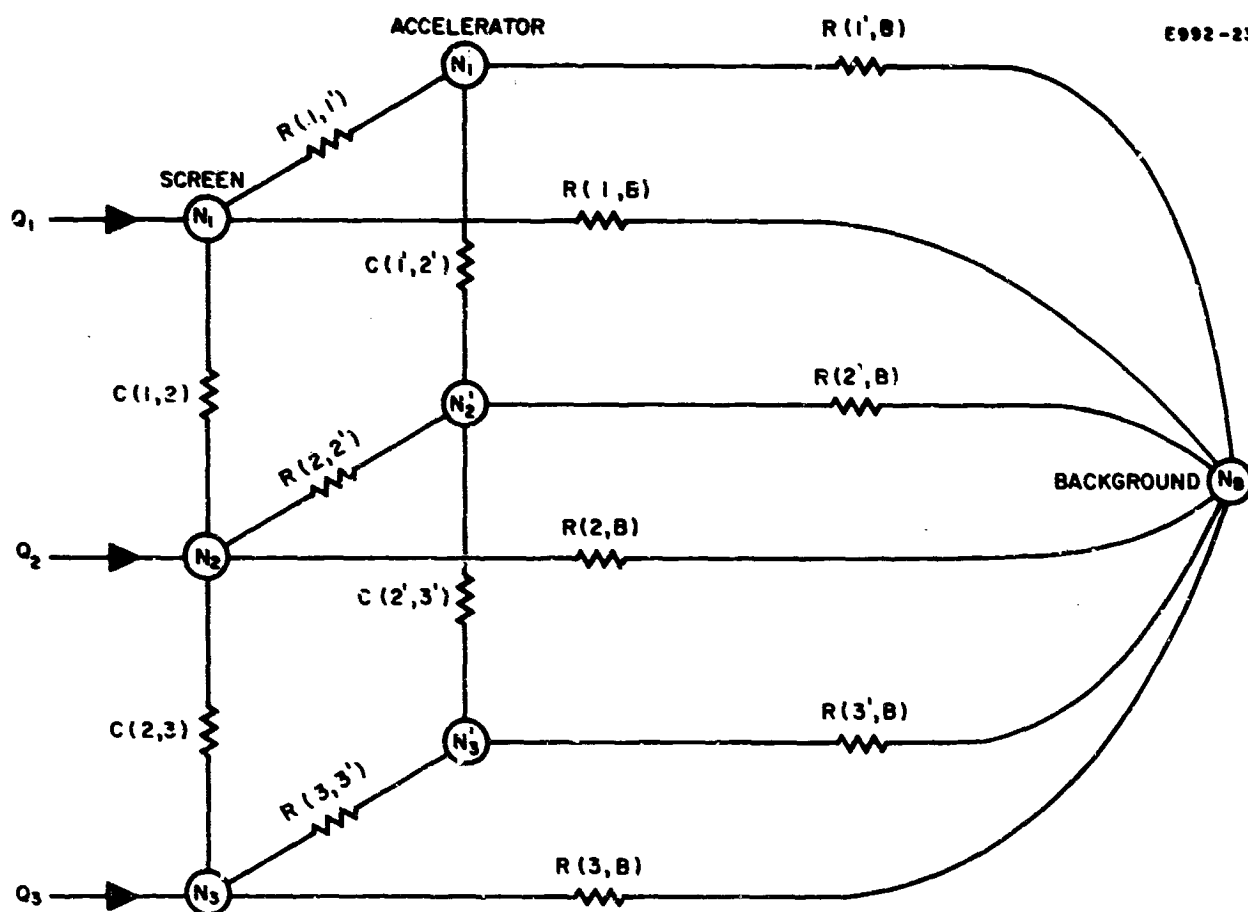
Fig. 25. Thermal network for grid system.

E992-26

(a)

(b)
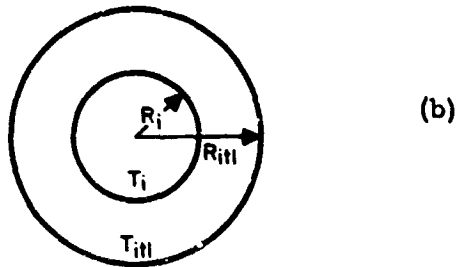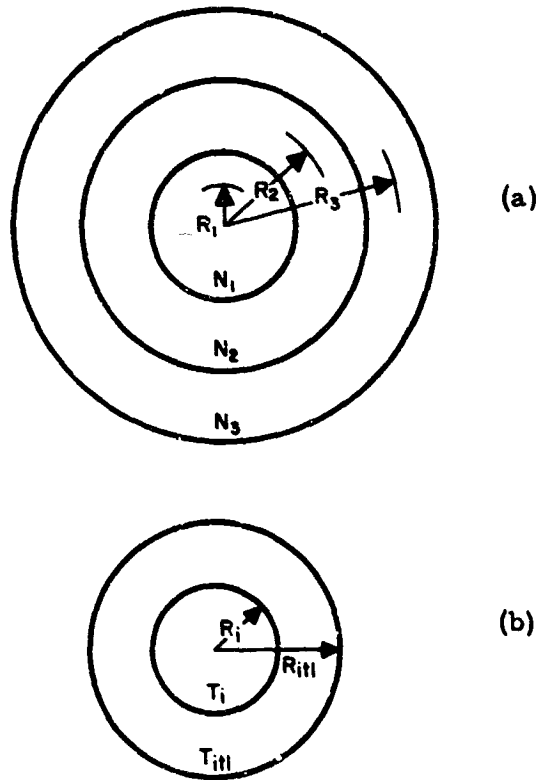
Fig. 26.
Heat conduction between an-
nular regions.

inside and outside edges of the washer shown in Fig. 26(b). The formula for this conductance is

$$C_{i,i+1} = \frac{2\pi t K'}{\log \frac{R_{i+1}}{R_i}}$$

where

    t $\equiv$ thickness of the washer

    K' $\equiv$ thermal conductivity of the washer.

For a perforated plate of open area fraction f and material thermal conductivity K, we take $K' = (1 - f) K$.

      b.   <u>View Factors for Radiative Heat Transfer in the</u>

               <u>Grid System</u> — Because of the small spacing between the electrodes relative to the radii of the annular nodes (see Fig. 24), it is reasonable to assume that radiative heat transfer occurs only between the directly opposing nodes (i. e., between N_i and N_i'). Under this assumption the desired view factors for the grid system can be calculated on the basis of two infinite parallel perforated plates. The geometry of a cross section of two aligned perforated plates S and A is shown in Fig. 27. The nodes for which view factors are to be calculated are indicated by the numbers 1 through 7. The actual calculations are carried out in Appendix II; because of their complexity, approximations are made. The nodes 1 through 6 describe in detail the coupling between each set of nodes (N_i, N_i'). The over-all detailed network for the grid system has three sets of six nodes each, as shown in Fig. 28.

      The heat incident on the screen electrode is first divided (into Q_1, Q_2, and Q_3) between the three nodes N_1, N_2, and N_3. A radial heat flux distribution is assumed which varies linearly between Q_o at the center of the screen and Q_R at the edge. The heat components Q_i are then split into $(1 - f_s)Q_i$ (input to the material surface of N_i (node 3)) and $f_s Q_i$ (input to the open surface area of N_i (node 1)). Here f_s is the open area fraction of the screen. In the heat transfer calculations it is assumed that node 1 is a black body $(\epsilon = 1)$.
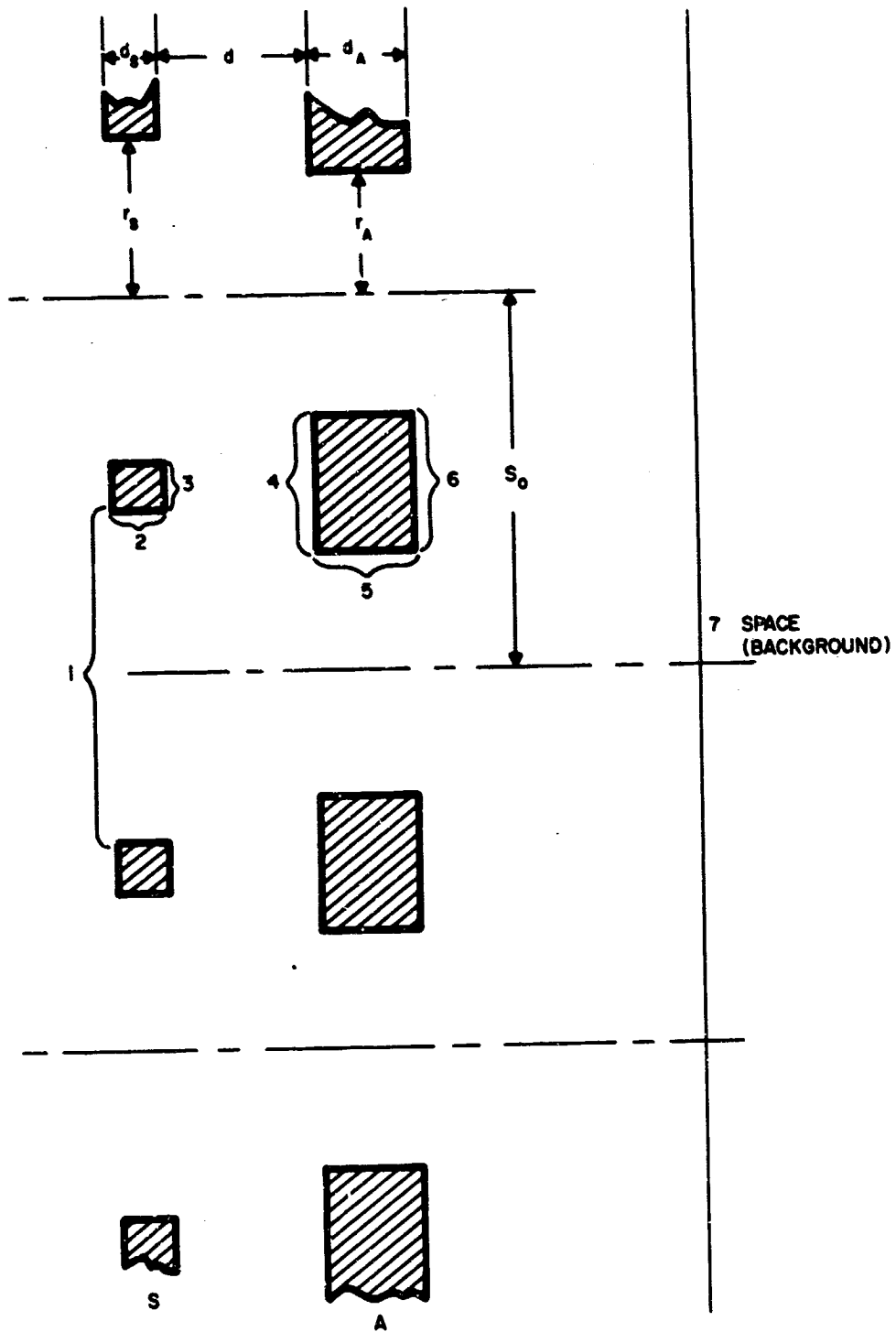
Fig. 27. Cross section of parallel perforated plates.
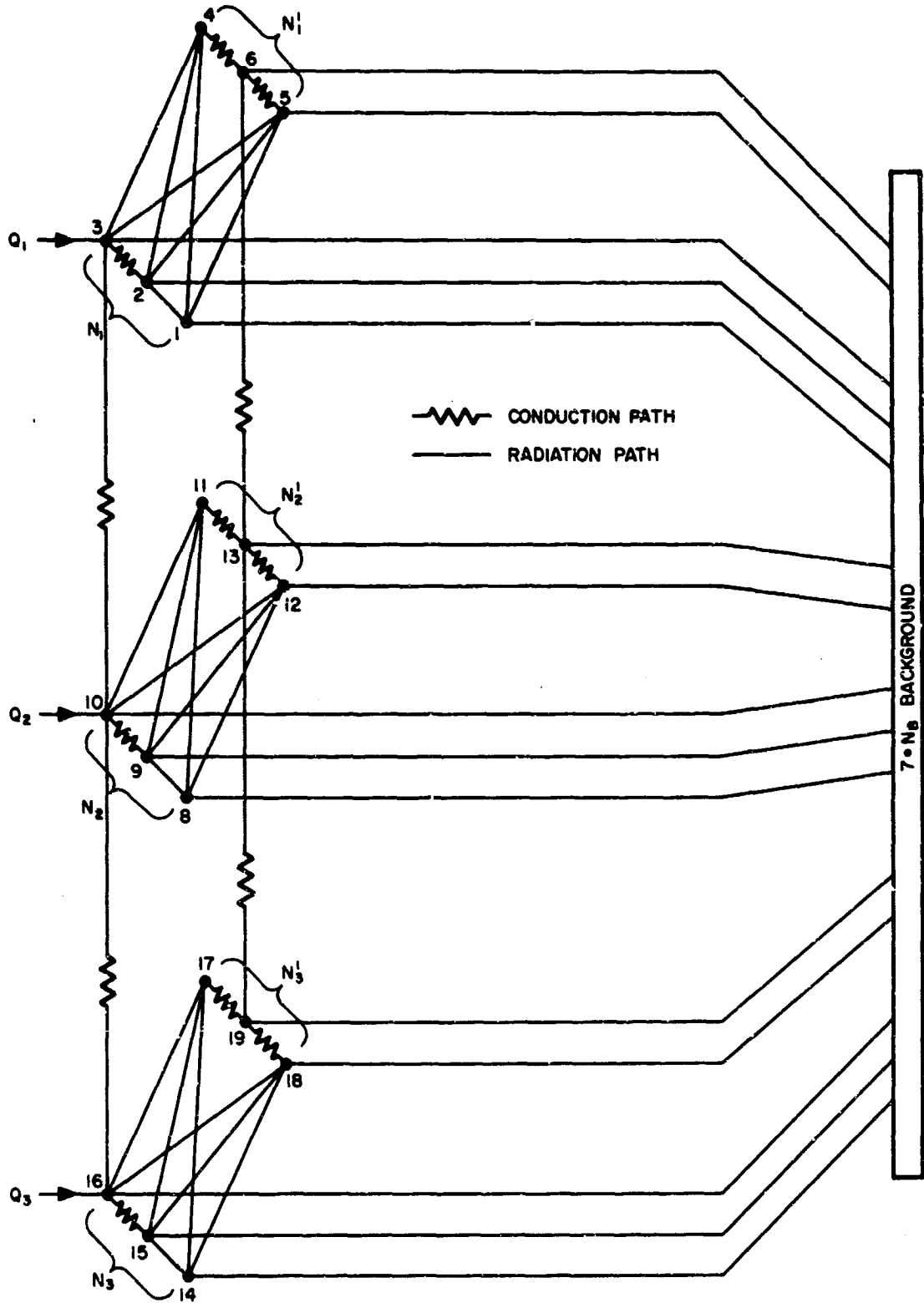
Fig. _   _tailed thermal network for grid system.

2. Grid System Temperature Distributions

A parametric study of the equilibrium grid system tempera-
ture distributions was made for a variety of electrode spacings and input
power profiles. The calculations were carried out by the computer
program TAS-1B and employ the network model shown in Fig. 28. The
nodal areas and thermal conductivities, which correspond to the assumed
electrode geometry given in Table VI, are given in Table VII. The view
factors corresponding to three values of electrode spacing 0.09 in., 0.07 in.,
and 0.05 in. are given in Table VIII.

TABLE VI

Assumed Electrode Geometry

	Screen	Accelerator
Diameter	30 cm	30 cm
Thickness	0.030 in.	0.060 in.
Open area	70%	40%
Hole diameter	0.187 in.	0.142 in.
Hole spacing	0.213 in.	0.213 in.

The sensitivity of the electrode temperature distributions to
variations in (a) electrode spacing, (b) discharge power distribution,
(c) total discharge power, and (d) interception power was studied and
will now be discussed.

a. Electrode Spacing — The sensitivity of the electrode
temperatures to the spacing between the electrodes is due to the depen-
dence of the view factors on spacing (see Table VIII).

The six curves in Fig. 29 give the screen and accelerator
electrode temperatures for three values of spacing. As shown,
decreasing the interelectrode spacing lowers the over-all temperatures
of both electrodes. Apparently, the grid system appears more trans-
parent to the incident radiation as the electrode spacing decreases.

66

E992-33R2
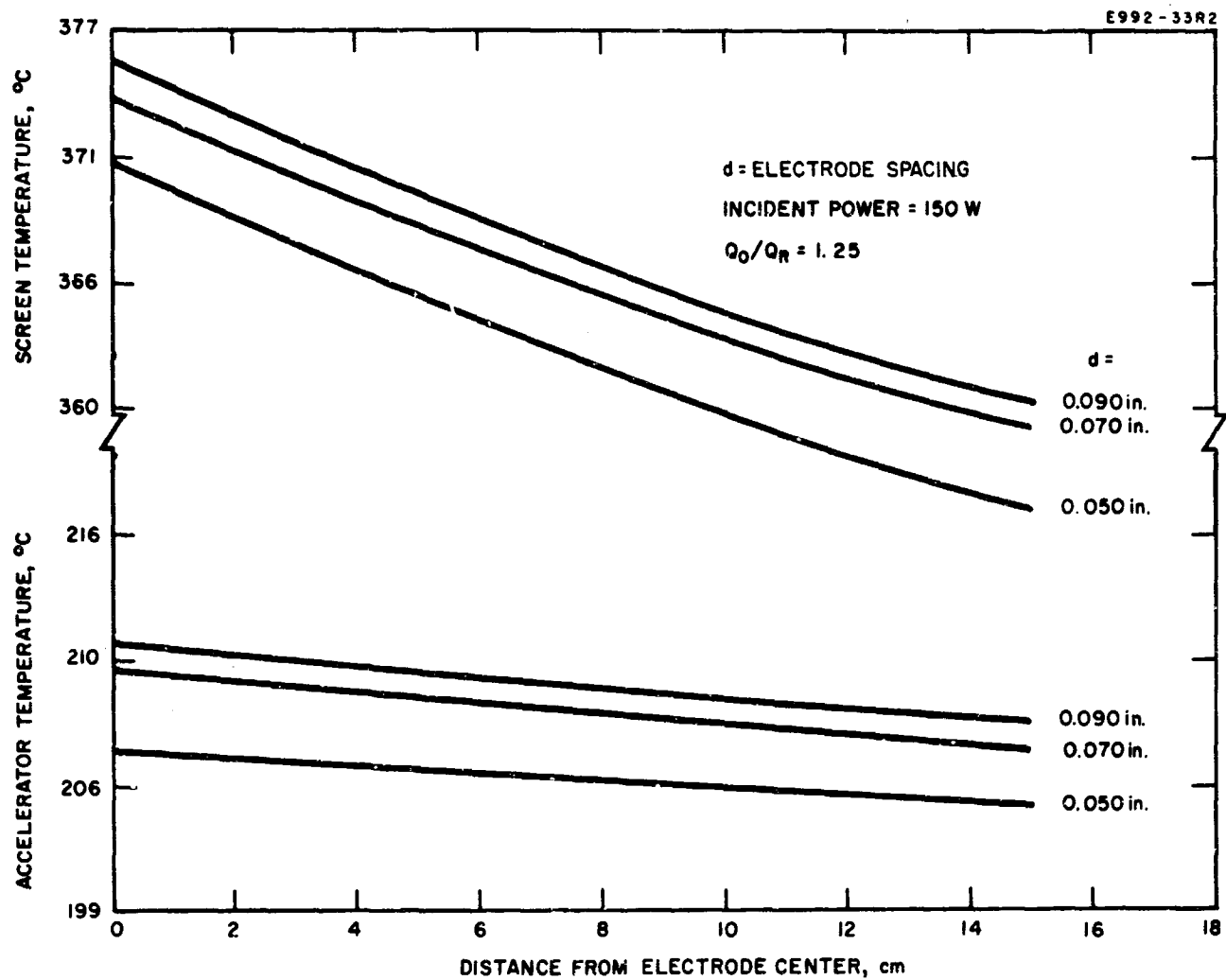
Fig. 29. Dependence of grid system temperature distributions on electrode spacing.

Since the actual decrease in temperatures is small and the temperature gradients across the electrodes remain unchanged as the spacing varies, the assumption that the grid system temperature distributions can be calculated independently from the thermal-warping is substantiated.

TABLE VII

Nodal Areas, Power Inputs, and Thermal Conductivities

Areas, in.^{2}	Thermal Conductivities, W/$^\circ$C
A_1 = 8.55	$C_{3,10}$ = 0.314
A_2 = 5.50	
A_3 = 3.55	$C_{10,16}$ = 0.674
A_4 = 7.30	
A_5 = 8.25	$C_{6,13}$ = 1.28
A_6 = 7.30	
A_7 = 10^7	$C_{13,19}$ = 2.74
A_8 = 25.6	
A_9 = 16.4	
A_{10} = 10.8	$C_{2,3}^a$ = $C_{9,10}$ = $C_{15,16}$ =
A_{11} = 21.6	
A_{12} = 24.6	$C_{4,5}$ = $C_{17,18}$ = $C_{5,6}$ =
A_{13} = 21.6	
A_{14} = 43.0	$C_{12,13}$ = $C_{18,19}$ =
A_{15} = 27.5	
A_{16} = 17.8	$10^6 \dfrac{W}{^\circ C}$
A_{17} = 36.2	
A_{18} = 41.7	
A_{19} = 36.2	

[a]Instead of calculating the very high conductances between these nodes, we insured that they arrive at equal temperatures by coupling them with very high conductances.

TABLE VIII

Grid System View Factors

	Electrode Spacing		
	0.90 in.	0.070 in.	0.050 in.
$F_{1,2} = F_{8,9} = F_{14,15}$	0.27	0.27	0.27
$F_{1,4} = F_{8,11} = F_{14,17}$	0.38	0.35	0.33
$F_{1,5} = F_{8,12} = F_{14,18}$	0.14	0.16	0.17
$F_{1,7} = F_{8,7} = F_{14,7}$	0.21	0.22	0.23
$F_{2,2} = F_{9,9} = F_{15,15}$	0.15	0.15	0.15
$F_{2,4} = F_{9,11} = F_{15,17}$	0.31	0.29	0.26
$F_{2,5} = F_{9,12} = F_{15,18}$	0.05	0.07	0.09
$F_{2,7} = F_{9,7} = F_{15,7}$	0.05	0.06	0.06
$F_{3,4} = F_{10,11} = F_{16,17}$	0.60	0.68	0.75
$F_{3,5} = F_{10,12} = F_{16,18}$	0.3	0.26	0.21
$F_{3,7} = F_{10,7} = F_{16,7}$	0.1	0.06	0.04
$F_{5,5} = F_{12,12} = F_{18,18}$	0.34	0.34	0.34
$F_{5,7} = F_{12,7} = F_{18,17}$	0.33	0.33	0.33
$F_{6,7} = F_{13,7} = F_{14,7}$	1.0	1.0	1.0

b.   Discharge Power Distribution — As shown in Fig. 24, the heat flux distribution from the discharge chamber is assumed to vary linearly between the values Q_o at the center and Q_R at the edge. Since heat conduction is small in the scree.. electrode (because it is thin and highly perforated) its temperature gradient, from center to edge, will depend strongly on the ratio Q_o/Q_R. This dependence is illustrated by the three sets of temperature distributions in Fig. 30, which correspond to $Q_o/Q_R = 1$, 1.5, 2. For all three cases the total discharge power incident on the screen is 250 W and the interception power into the accelerator is 20 W (10 W into node N_1' and 10 W into N_2'). The heat intensity ratio $Q_o/Q_R = 1.5$ gives rise to a 40°C temperature variation from the screen center to edge. This value is considered reasonable and is used in the subsequent sensitivity studies.

c.   Total Discharge Power — The total heat flux incident on the screen electrode from the discharge chamber is highly dependent on the specific discharge chamber performance characteristics (e. g. , the ionization efficiency) and the operating point of the thruster. The variations in the screen and accelerator center temperatures and center to edge temperature differences have therefore been calculated as functions of the total discharge power. The curves are shown in Fig. 31. For a total discharge chamber power (cathode power plus arc power) of 400 W it is reasonable to expect that half (200 W) will be incident on the screen. In this case the electrode temperatures are the following:

	Screen	Accelerator
Center Temperature	430°C	290°C
Edge Temperature	407°C	269°C

d.   Interception Power — As illustrated in Figs. 30 and 31, the effects of varying the discharge power intensity ratio Q_o/Q_R and the total discharge power are most noticeable on the screen electrode. Another source of power into the grid system is the heating of the

70
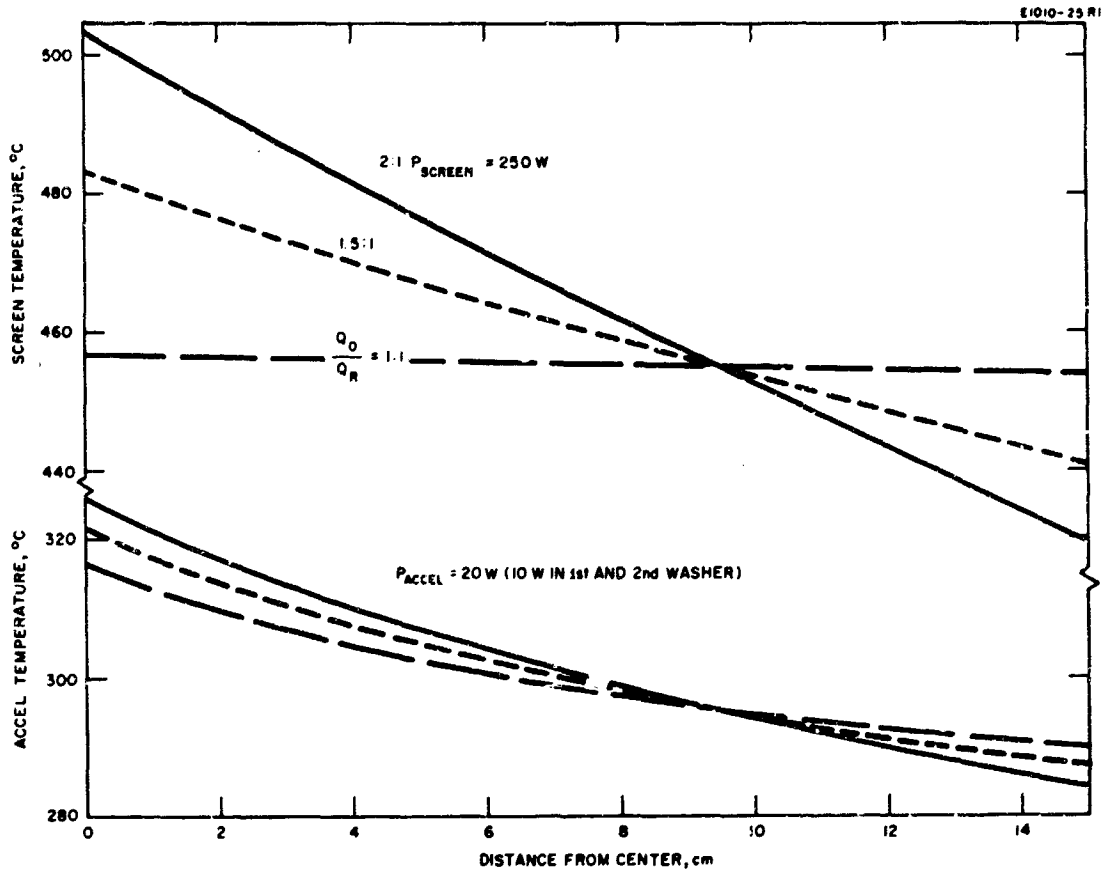
Fig. 30.   Dependence of electrode temperatures on discharge power
            distribution.

E1010-24
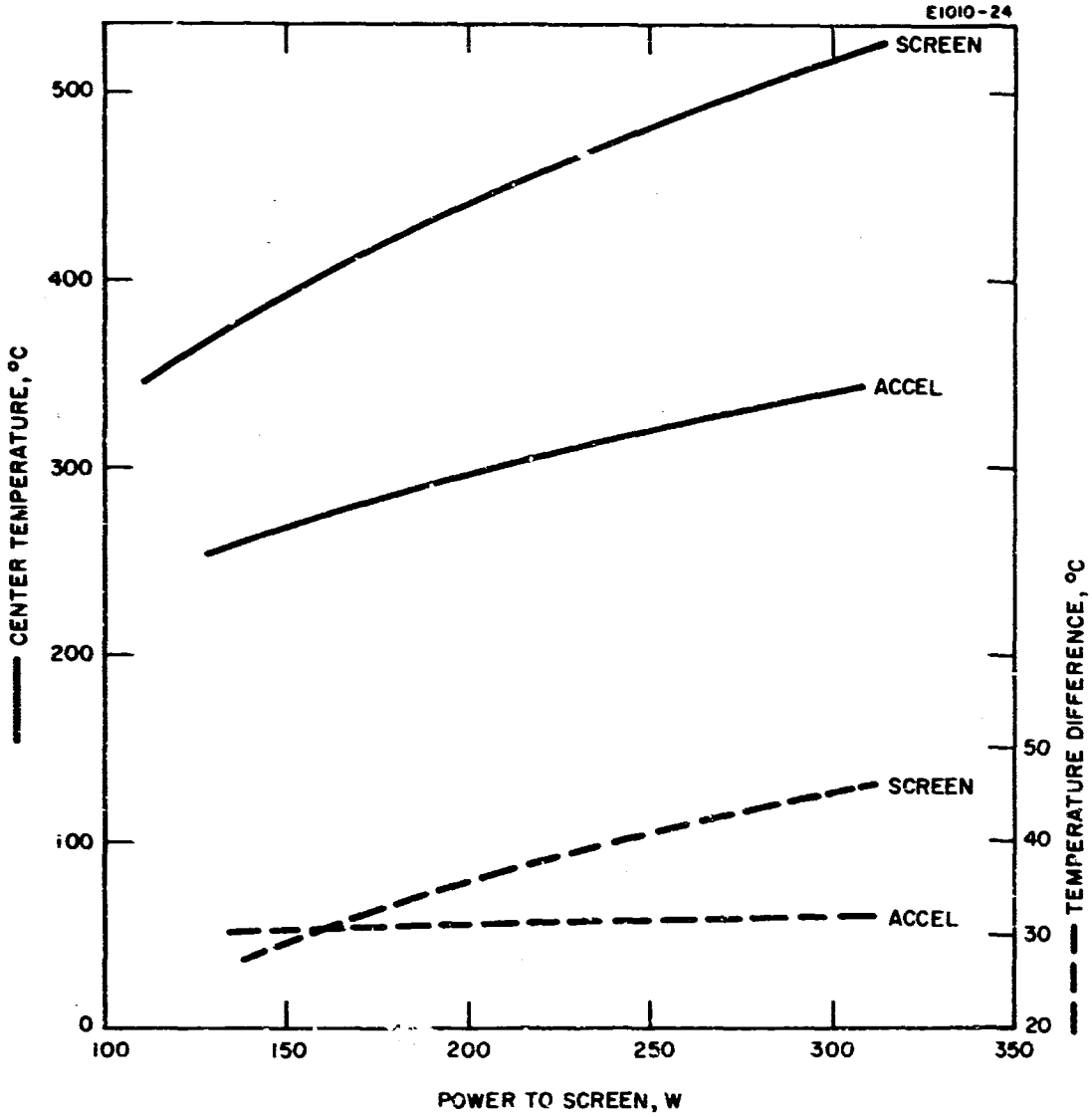
Fig. 31. Dependence of electrode temperatures on total discharge power.

72

accelerator by intercepted ions, which may be produced by charge exchange collisions. Relatively small amounts (10 to 20 W) of interception power cause noticeable accelerator temperature changes, as shown in Fig. 32. The interception power is divided equally between nodes N_1' and N_2' (see Fig. 32). Since the areas of nodes N_1', N_2', N_3' are in the ratios 1:4:9, the interception power distribution assumed is peaked in the center. The accelerator center to edge temperature difference is increased from $10^\circ C$ to $30^\circ C$ by 20 W of interception power.

In Fig. 33, a breakdown of the heat flow paths in the grid system is shown for the case of 200 W incident on the screen in the distribution $Q_o/Q_R = 1.5$ and 20 W of interception power. The quantities of heat indicated represent the net heat transferred after multiple reflections. Of the 29.2 W incident on the node N_1, 20.8 W goes to space (part by radiation and part by transfer straight through the holes), 6.4 W is absorbed by the accelerator node N_1', and 2 W are conducted to the adjacent screen node N_2.

3.   Correlation of the Thermal Model with Experiment

An opportunity to correlate the thermal model which we have developed with some experimental data was provided by some recent JPL temperature measurements on an operating thruster. The electrode geometry of the JPL thruster is the following:

	Screen	Accelerator
Diameter	20 cm	20 cm
Thickness	0.030 in.	0.110 in.
Open Area	70%	40%
Hole Diameter	0.187 in.	0.142 in.
Hole Spacing	0.213 in.	0.213 in.

and the electrode spacing is 0.070 in. The corresponding nodal areas, view factors, and thermal conductivities are given in Table IX. Steady
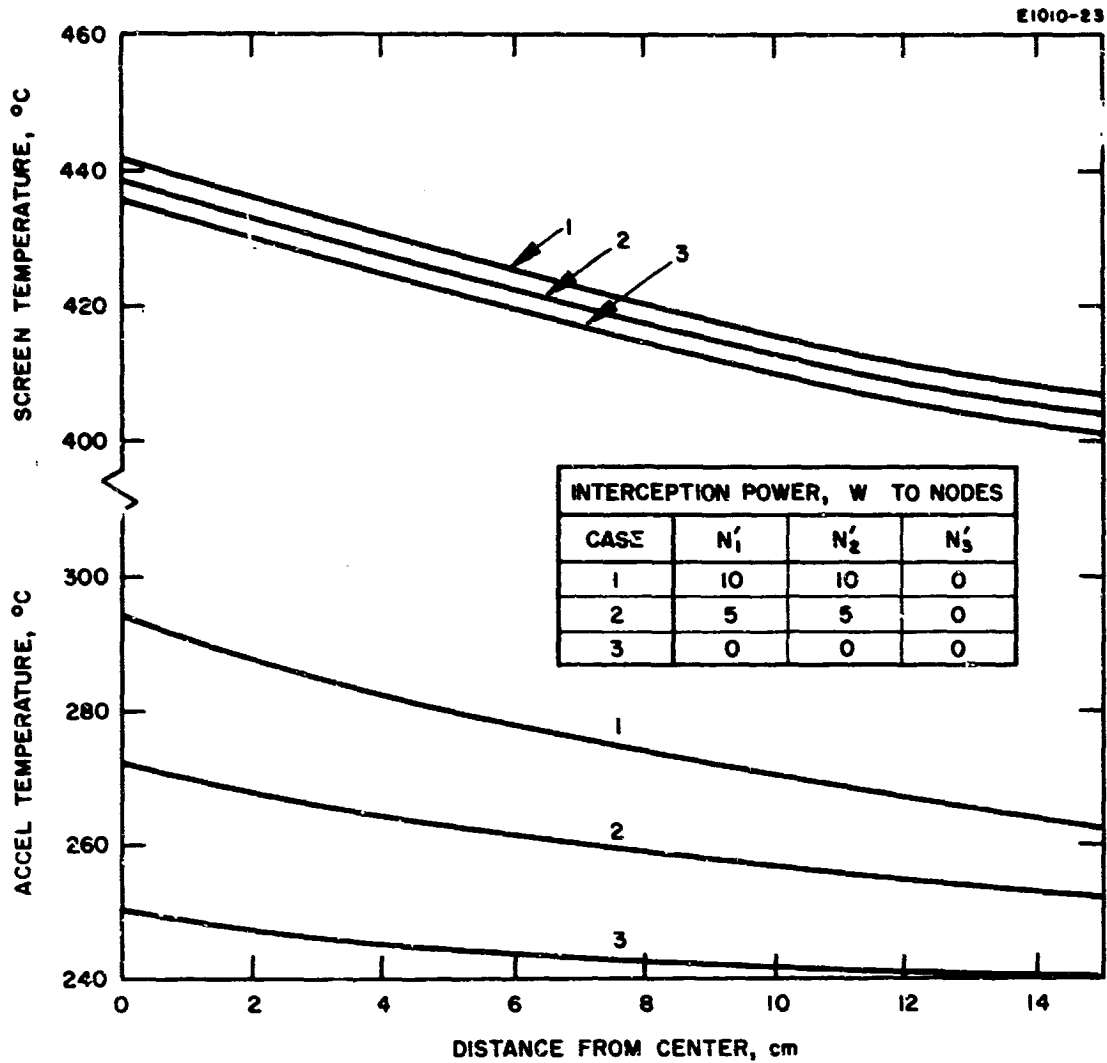
Fig. 32.   Dependence of electrode temperatures on interception power.
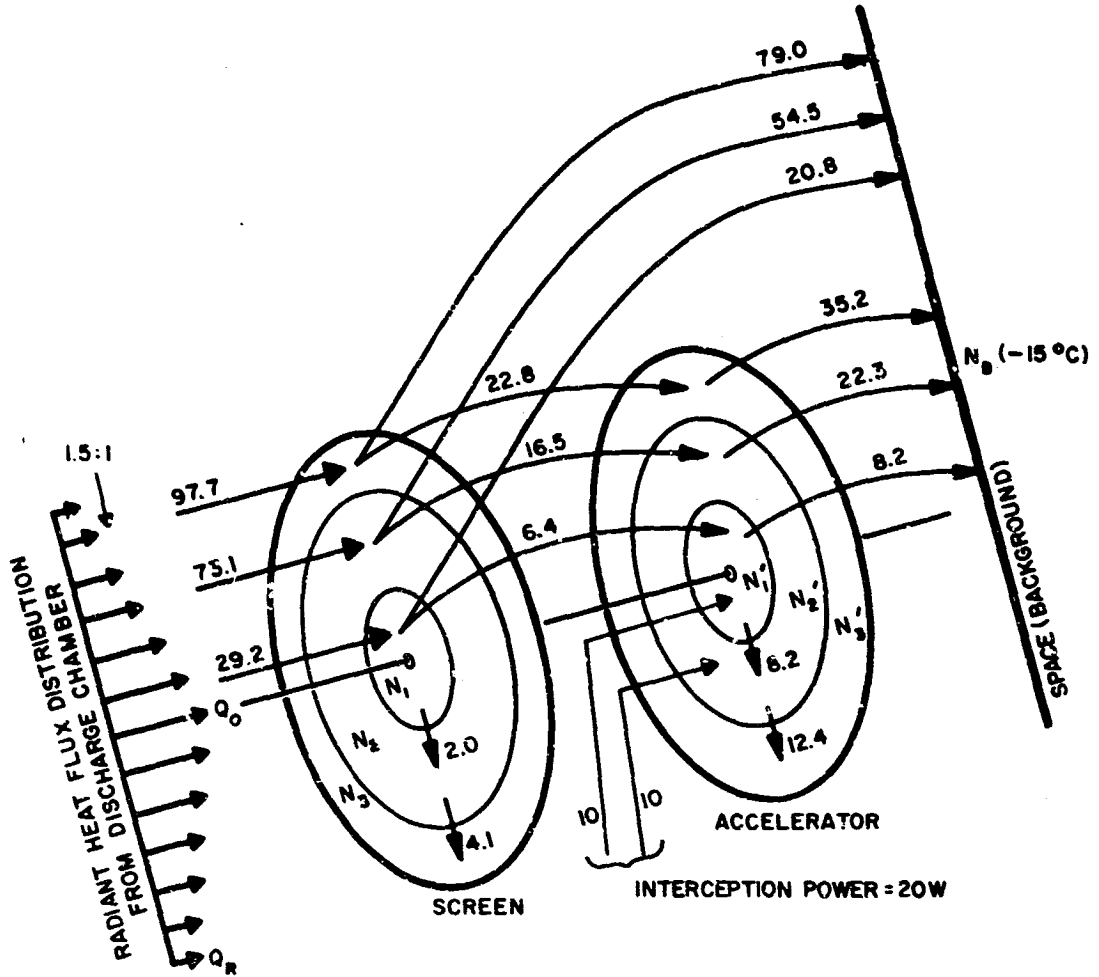
Fig. 33.   Heat flow paths in the grid system.   30 cm P_{in} = 200 W.
P_{Acc} = 20 W.

TABLE IX

Nodal Areas, View Factors, and Thermal Conductivities for the JPL
20 cm Thruster

View Factors				Areas, ft^2	
$F_{1,2}$ = $F_{8,9}$	= $F_{14,15}$	= 0.27		A_1 =	0.0351
$F_{1,4}$ = $F_{8,11}$	= $F_{14,17}$	= 0.35		A_2 =	0.0225
$F_{1,5}$ = $F_{8,12}$	= $F_{14,18}$	= 0.24		A_3 =	0.0147
				A_4 =	0.0297
$F_{1,7}$ = $F_{8,7}$	= $F_{14,7}$	= 0.14		A_5 =	0.0566
$F_{2,2}$ = $F_{9,9}$	= $F_{15,15}$	= 0.15		A_6 =	0.0297
				A_7 =	10^9
$F_{2,4}$ = $F_{9,11}$	= $F_{15,17}$	= 0.29		A_8 =	0.105
$F_{2,5}$ = $F_{9,12}$	= $F_{15,18}$	= 0.07		A_9 =	0.0675
$F_{2,7}$ = $F_{9,7}$	= $F_{15,7}$	= 0.06		A_{10} =	0.044
				A_{11} =	0.089
$F_{3,4}$ = $F_{10,11}$	= $F_{16,17}$	= 0.68		A_{12} =	0.169
$F_{3,5}$ = $F_{10,12}$	= $F_{16,18}$	= 0.26		A_{13} =	0.089
$F_{3,7}$ = $F_{10,7}$	= $F_{16,7}$	= 0.06		A_{14} =	0.175
				A_{15} =	0.112
$F_{5,5}$ = $F_{12,12}$	= $F_{18,18}$	= 0.50		A_{16} =	0.073
$F_{5,7}$ = $F_{12,7}$	= $F_{18,17}$	= 0.25		A_{17} =	0.148
$F_{6,7}$ = $F_{13,7}$	= $F_{19,7}$	= 1.0		A_{18} =	0.282
				A_{19} =	0.148

Thermal Conductivities, Btu/hr/°F	
$C_{3,10}$ =	0.299
$C_{10,16}$ =	0.681
$C_{6,13}$ =	2.01
$C_{13,19}$ =	4.55

$$C_{2,3}^a = C_{9,10} = C_{15,16} = C_{4,5} = C_{17,18} = C_{5,6} = C_{12,13} =$$

$$C_{18,19} = 10^6 \ \frac{W}{°C}.$$

[a]Instead of calculating the very high conductances between these nodes, we insured that they arrive at equal temperatures by coupling them with very high conductances.

state temperatures of 350°C and 322°C were measured by thermocouples located at the center and edge of the screen electrode with the thruster at the operating point:

Beam current	=	577 mA
Accelerator current	=	8 mA
Total voltage	=	4 kV
Mass utilization	=	69%
Arc power	=	100 W
Cathode power	=	100 W

A set of screen and accelerator temperature distributions were calculated with a total power of 150 W incident on the screen for a $Q_o/Q_R = 1.5$ distribution, for various values of interception power. The curves are given in Fig. 34. The case of 30 W of interception power (15 W into each node N_1' and N_2') gives accelerator center and edge temperatures of 354°C and 326°C, which are seen to be in excellent agreement with the measured values. The value of 30 W for the interception power was chosen to be equal to that observed in the comparison thruster, the 150 W total power was assumed as a reasonable fraction of the total discharge power (200 W), and the value $Q_o/Q_R = 1.5$ was chosen to give best agreement between theory and experiment; this last value is also quite reasonable. It is felt that, within the uncertainties of the parametric choices, the closeness of the calculated and observed temperatures shows that the analysis is a useful tool.

C. Stress Analysis of Electrodes at Operating Temperature

In Section III-B a thermal model of the grid system was developed for predicting the temperatures of the electrodes under normal (unperturbed alignment) operating conditions. Since the current practice is to align the electrodes precisely during assembly, at room temperature, the differences between the electrode operating temperatures and room temperature represent thermal-stress producing temperature gradients. We believe that the stresses produced as the grid system

77
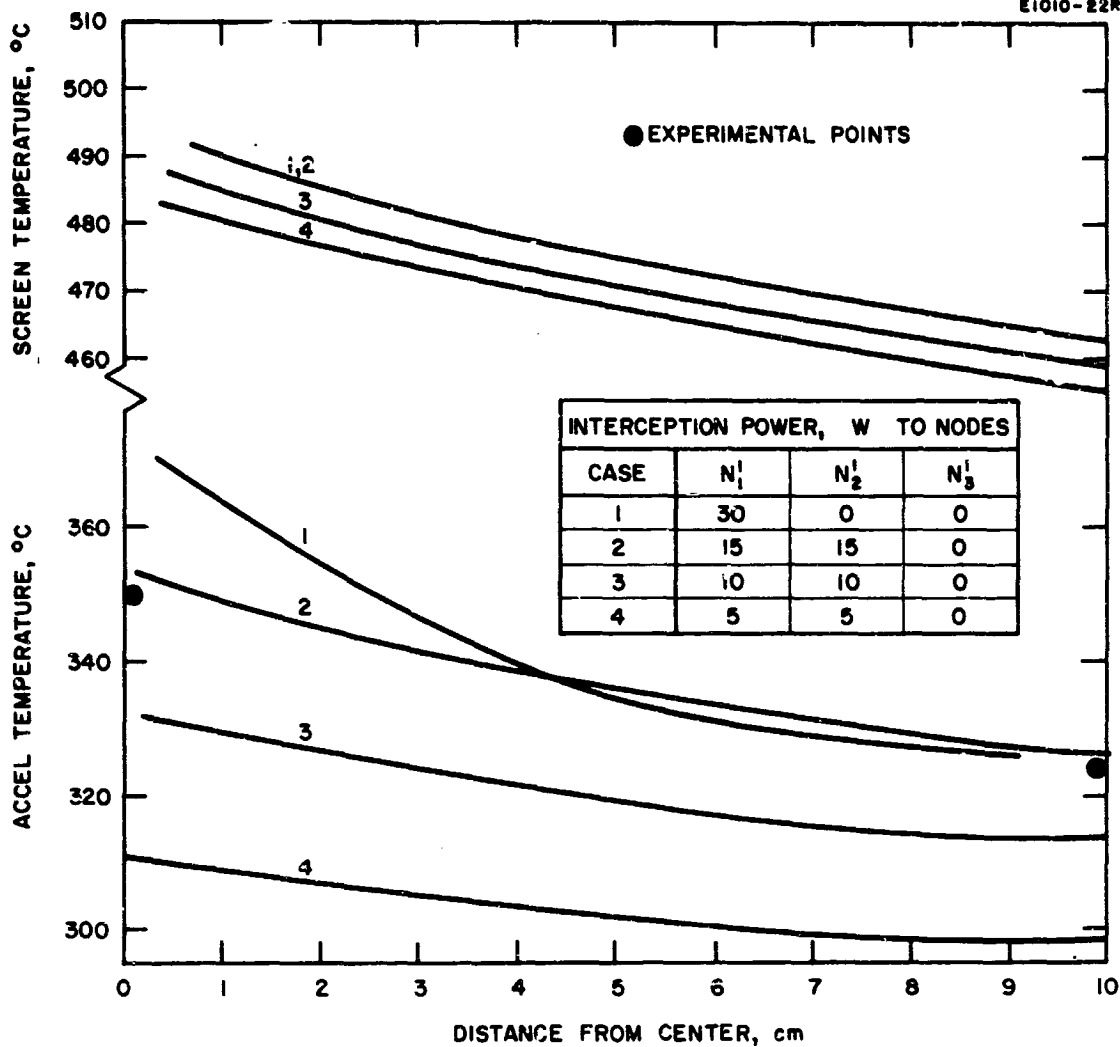
Fig. 34.   Dependence of electrode temperatures on interception power
(20 cm thruster).

undergoes heating to operating temperature produce the largest axisymmetric misalignments which are likely to occur. A significant effort has therefore been devoted to predicting these misalignments quantitatively. Although it is the natural next step, the extension of our analysis to cover misalignments resulting from nonaxisymmetric thermal stresses would have been too time consuming and expensive for the Phase I study. We will note here only that this problem is of concern for operating thrusters in an array.

A computer program which analyzes shells by the finite element method was used to study the thermal-buckling of the electrodes. The computer programs can handle shells of revolution subject to axisymmetric or asymmetric mechanical and thermal loads. An electrode is divided into washer shaped regions which form the elements of the model. Thermal and mechanical loads are prescribed on each element and the computer program solves the equations of motions for the deformations. Since the dimensions of each element can be specified independently, initially dished electrodes can be considered.

Because the stress analysis program considers solid plates, a literature search was conducted to determine whether an equivalent set of thermal and elastic parameters could be used in the solid plate analysis in order to simulate the actual punched plate electrode. It was found that such an equivalence is possible and has been used in the analysis. The values of equivalent elastic constants for the perforated plates, inferred from the paper by O'Donnell and Langer,[5] are the following

	Young's Modulus $(\%/^\circ F)$	Poisson Ratio
Screen	2.15×10^{6}	0.7
Accelerator	10.8×10^{6}	0.36

1.   Nominal Case

Thermal warping of the screen and accelerator electrodes was calculated for the temperature distributions which correspond to an incident screen power of 200 W, with $Q_o/Q_R = 1.5$, and 20 W of

interception power (Case 1 of Fig. 32). The radial and axial displace-
ments of the electrodes are shown in Fig. 35. Both electrodes were
initially dished to a depth of 0.010 in., and no mechanical loading is
present. Under these conditions the small perturbations in alignment
which occur are (1) a decrease in electrode shaping of 0.003 in.
maximum at the center and (2) radially outward motion of the screen
holes with respect to the accelerator holes, the maximum being 0.0044 in.
at the edge.

From this warping calculation some indication is given of the
behavior of a grid system (initially aligned at room temperature) when
it is heated to operating temperature. The main effects are as follows:

a.   Radial and axial displacements of both electrodes will
      occur.

b.   Both displacements will be greater for the screen
      because it becomes hotter with a larger temperature
      gradient, has a larger open area, and is thinner than
      the accelerator electrode.

c.   The misalignments which result from the above dis-
      placements are (a) a decrease in the electrode spacing,
      and (b) a transverse (radially outward) motion of the
      screen holes with respect to the accelerator holes.

d.   The magnitude of the decrease in spacing resulting
      from bowing of both electrodes is most dependent on
      the temperature gradients; the magnitudes of the radial
      diaplacements depend on the over-all temperature levels
      of the electrodes.

2.   Sensitivity to Mechanical Design

      The above warping calculations revealed the main buckling
motions found in the grid system. It will now be shown that the magnitudes
of these motions are highly sensitive to the grid system mechanical
design. The importance of two design points will now be considered:
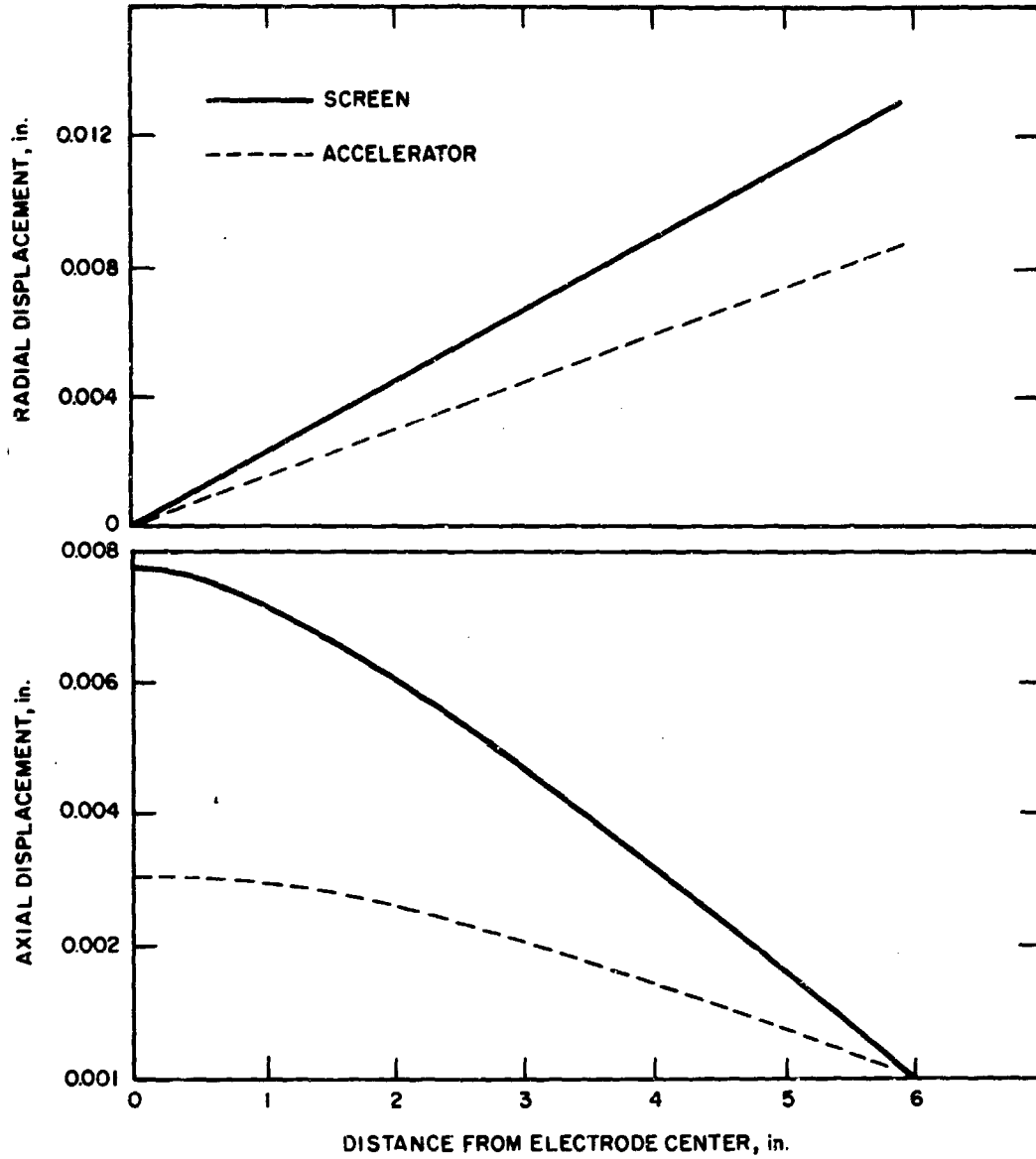
Fig. 35.   Axial and radial displacements of electrodes due to thermal warping with no mechanical loading.

(a) the sensitivity of the axial displacement of an electrode (after heating) to the depth to which it was initially dished, and (b) the influence of radial clamping forces such as those produced by the electrode supports.

a.   Initial Depth — If warping of the screen electrode is calculated under the same conditions (i. e., temperature distribution) as above but for an initial dish depth of 0. 040 in. (instead of 0. 010 in.), the much larger axial displacement (shown in Fig. 36) is found. To look more deeply into the dependence of axial displacement on initial depth, the axial displacement caused by heating to a given temperature distribution was found for electrodes of initial depths ranging from 0. 004 in. to 4 in. Again, no mechanical loading was present. The resulting curve (for the axial displacement at the center) is shown in Fig. 37. The appearance of a peak in the axial displacement curve was not expected, and an explanation was sought. For larger values of initial depth the curve approaches linear thermal expansion of about 0. 002 in. /in. , which was expected in view of the final average electrode temperature of 700°F and expansion coefficient of $8 \times 10^{-6}/^\circ$F.

An explanation of the decreasing portion of the curve (Fig. 37) was difficult to find because of the complicated nature of the two dimensional thermal stress problem being solved and because the competition between buckling forces is buried in the computer program. A satisfactory explanation of a qualitatively similar axial displacement versus initial position curve (e. g. , with a peak) was found, however, for an analogous thermal buckling problem. This analogous problem is simple enough to solve analytically and is discussed in detail in Appendix II.

b.   Radial Clamping — The computer program used to calculate the buckling of electrodes with no mechanical loading was also capable of finding the buckling of a radially clamped electrode. A strikingly large dependence of axial displacement on constrained radial displacement was found. Before presenting the numerical results a simple example of mechanical deformation of a parabolic dish is considered which points out how geometrically magnified axial displacements result when the radial displacements of an electrode are constrained.

82

E 1010-18
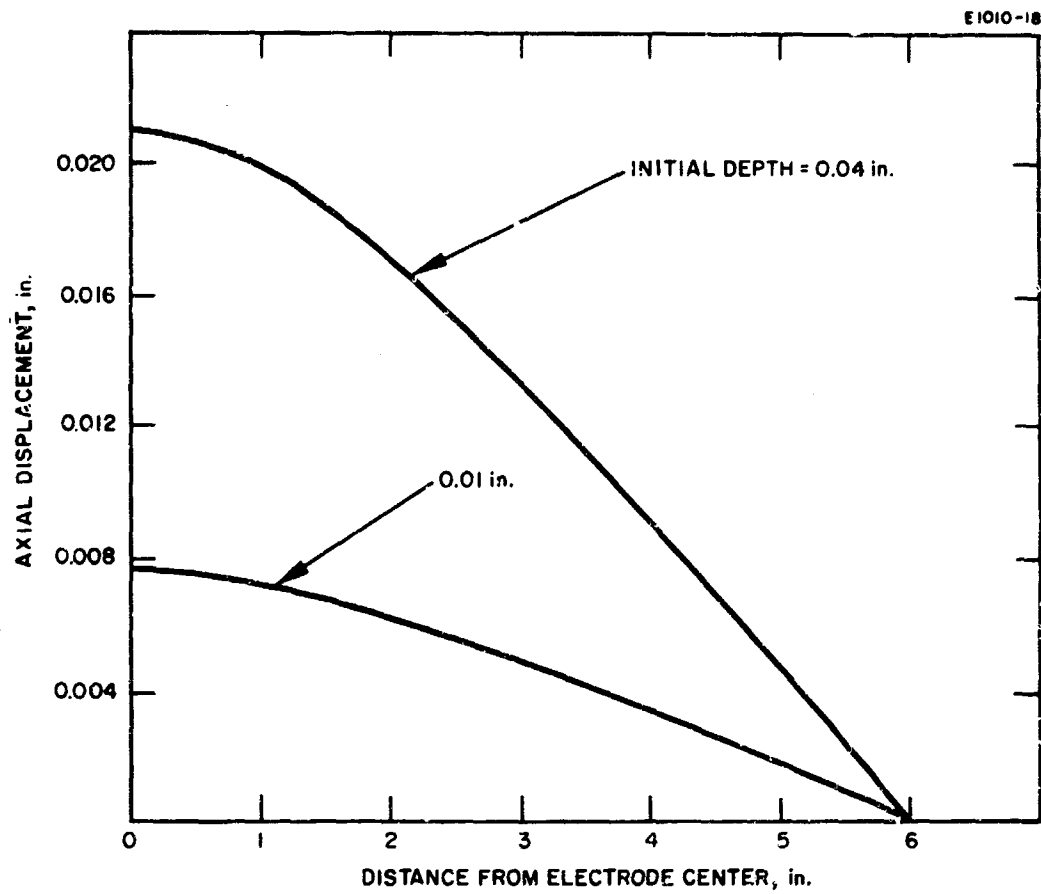
Fig. 36.   Sensitivity of axial displacement to initial depth.
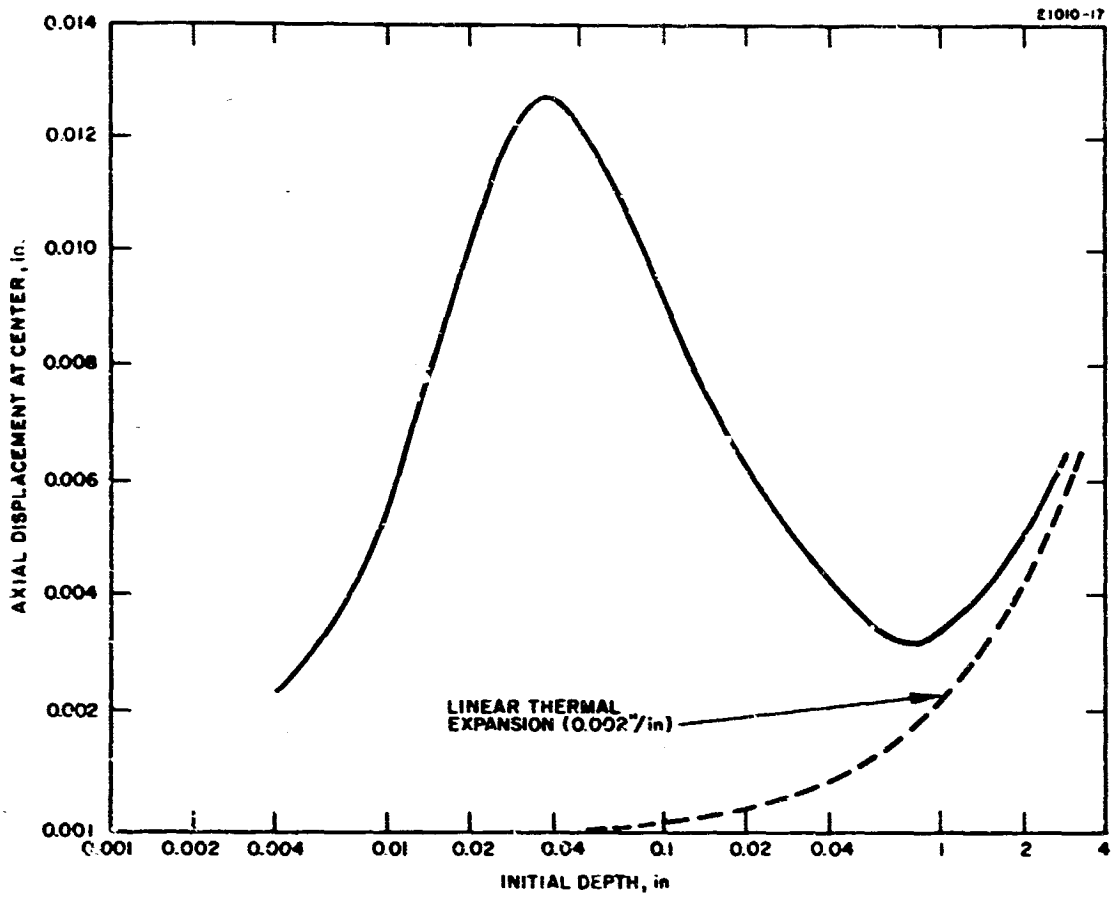
Fig. 37.   Axial displacement as a function of initial depth.

Consider a disk of depth h_o and radius R_o taken in the form of a parabola of revolution:

$$\underline{Z} = h_o\left(\frac{r}{R_o}\right)^2 \ .$$

Suppose that the radius of the given dish is reduced mechanically in such a way that the surface area of the dish remains constant. The result is that the dish will deform into a new shape with an increased depth. We wish to find the relationship between the change in radius ΔR and the change in depth Δh. This is easily done if it is assumed that the new shape of the dish is also a parabola of revolution with radius $R_o - \Delta R$ and the original surface area. With the original dish shallow, i.e.,

$$h_o \ << \ R_o \ ,$$

its surface area is

$$S_o = \pi(R_o^2 + h_o^2) \ .$$

The equation for the surface area of the deformed dish is

$$\pi(R^2 + h^2) = S_o \ ,$$

which can be solved for the new depth h as a function of the new radius R to obtain

$$h = \sqrt{R_o^2 - R^2 + h_o^2} \ . \tag{32}$$

In Fig. 38 the increase in depth ($\Delta h = h - h_o$) has been plotted as a function of the decrease in radius ($\Delta R = R_o - R$) for values of initial depth equal to 0.004 in, 0.02 in, 0.04 in, and 0.06 in. The important effect to observe is the enormous magnification between ΔR and Δh. From eq. (32) the derivative dh/dR is easily found to be
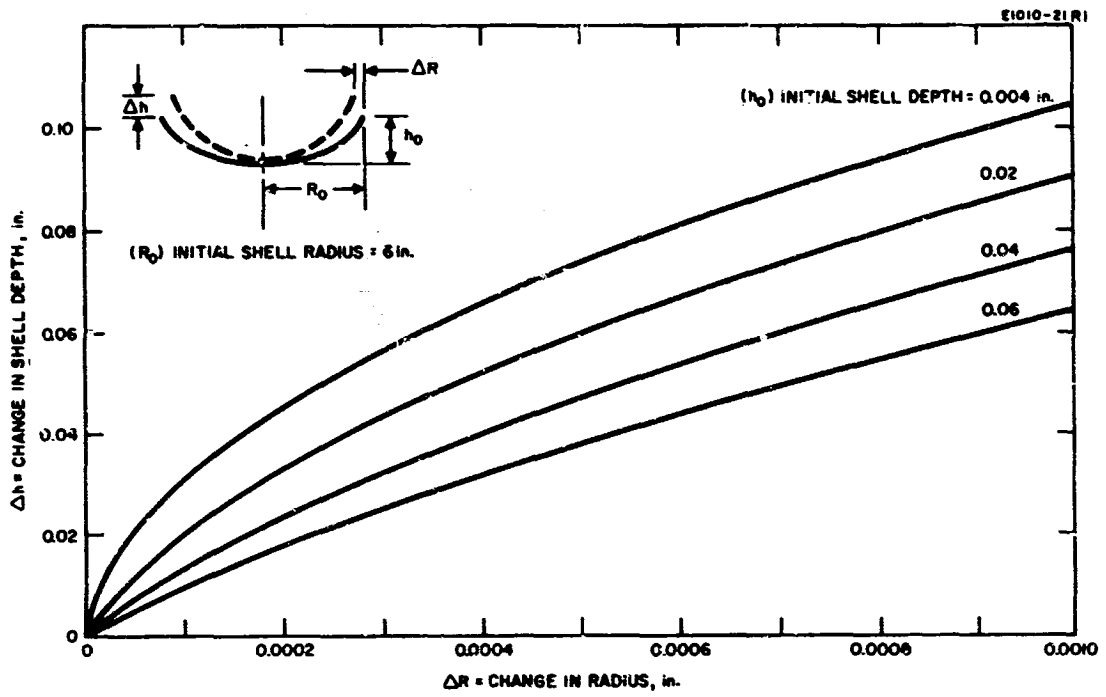
Fig. 38. Geometric effect of radial clamping.

$$\frac{dh}{dR} = - \frac{R}{h} \ .$$

Thus, the geometric magnification has magnitude R/h which is indeed very large for a shallow dish.

The effect of radially constraining an electrode which is thermally expanding was calculated by the Stress Analysis computer program. The case (shown in Fig. 36) of the screen electrode expanding from 0.040 in. initial depth to a final depth of 0.062 in. was used. Without radial constraining forces the radial expansion of the electrode is 0.01260 in. In the subsequent calculations a radial boundary condition was included which limited the radial expansion to values between 0.0124 and 0.0126 in. This radial constraint caused additional buckling of the electrode, as shown in Fig. 39. The curve is the final axial position at the center of the electrode versus the difference between free radial expansion (0.0126 in.) and the values specified by constraint. Thus, if clamping forces reduce radial expansion by 0.0001 in. the electrode center will move an additional 0.0135 in. (from 0.062 to 0.0755 in.).
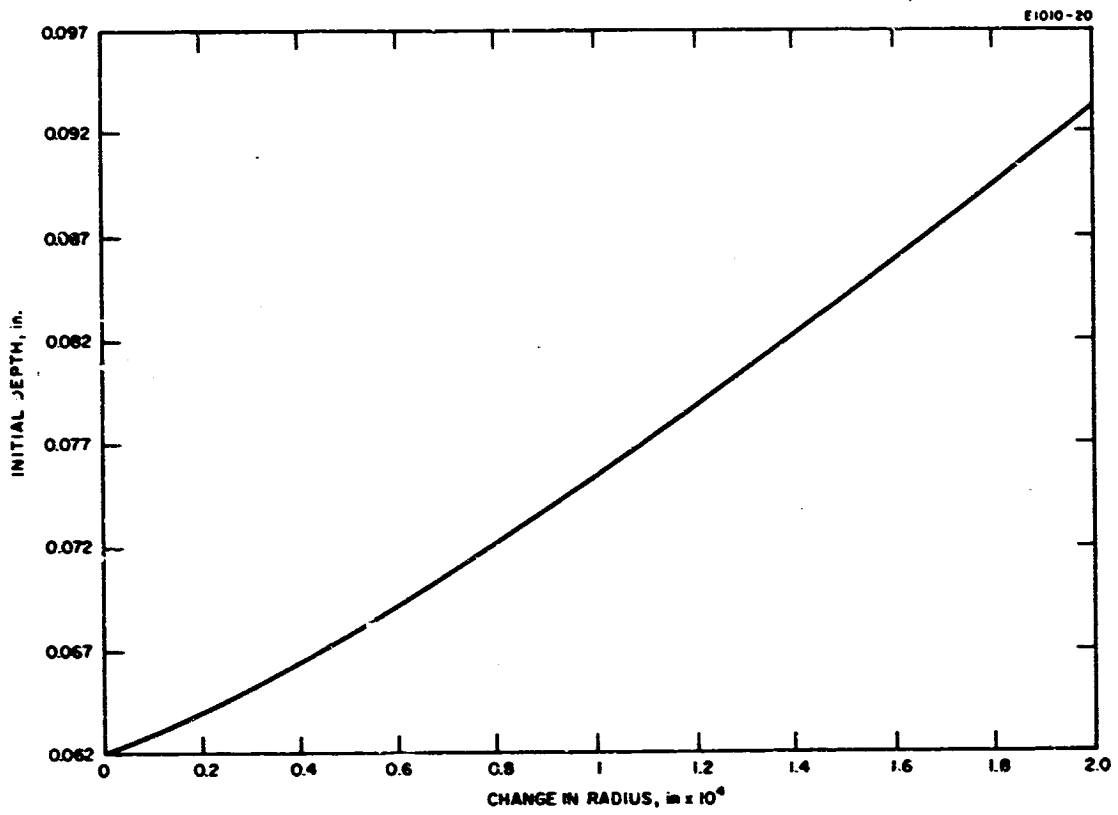
Fig. 39. Axial position of screen electrode center versus change in
radius due to mechanical constraint.

IV.   EXPECTED SINGLE ENGINE THRUST MISALIGNMENTS

A.   Introduction

In this section the perturbations in the thrust vector of a single engine which result from a number of modes of electrode misalignment are given quantitatively. The perturbations may be changes in the thrust magnitude and direction, or in the location of the center of thrust. Each mode of misalignment is analyzed independently. The effects of multiple modes can then be obtained by superposition.

B.   Elementary Modes of Electrode Misalignment

The beam intensity profile from an aligned Kaufman thruster is axisymmetric but varies radially from a maximum J_o at the center to a minimum J_1 at the edge. For typical thrusters measured beam profiles can be fit well by a gaussian curve of the form

$$J(r) = J_o \, e^{-\left(\frac{r}{r_o}\right)^2 \, \log\left(\frac{J_o}{J_1}\right)} \quad ,$$

where r_o is the radius of the thruster. For our example we have

$$J_o = 8 \, \frac{mA}{cm^2} \, , \quad J_1 = 2 \, \frac{mA}{cm^2} \, , \quad r_o = 15 \text{ cm} \quad .$$

Since these values of J_o and J_1 correspond to the densities of current leaving holes, the total thruster current is given by

$$I_o = \left(\int_o^{r_o} 2 \, \pi \, r \, J(r) \, dr \right) f_A$$

where f_A is the opened area fraction of the accelerator. Carrying out the integral yields the formula for the total current I_o in terms of the average current density $\bar{J}_o$:

89

$$I_o = \pi r_o^2 \, \bar{J}_o \, f_A, \quad \bar{J}_o = \frac{J_o - J_1}{\log J_o - \log J_1} \quad .$$

For our thruster $f_A = 0.4$, $\bar{J}_o = 4.3$ (mA/cm^2) and $I_{total} = 1.2$ A.

The thrust vector from a thruster with misaligned electrodes will be found by summing the perturbed thrusts contributed from each hole pair. First we consider the results of the ion optical study which gives the current density for a single hole pair under three modes of misalignment: (a) change in hole spacing, (b) relative displacement of the holes transverse to the beam. and (c) tilt of one hole out of its original plane (see Fig. 40). It turned out that only the first two modes produce significant thrust changes. Expressions for total engine thrust vector misalignment will then be derived for various electrode motions.

Changing the distance d between holes causes the plasma sheath position to move and results in a change in the total current from the hole pair. To include this effect in our analysis we let the current density J also be a function of the hole spacing d. For aligned electrodes the spacing is uniform $d_o (=0.090$ in.) and the current density is

$$J(r, d_o) = J_o e^{-\left(\frac{r}{r_o}\right)^2 \log\left(\frac{J_o}{J_1}\right)} \quad .$$

The dependence of the current density on spacing will be assumed linear and for small changes in spacing Δd

$$J(r, d_o + \Delta d) = J(r, d_o)\left\{1 + a\Delta d\right\} ,$$

where a is the percentage change in current density per unit spacing change. The value of a determined by the ion optical study is $6.5\%/mil$.

(a)   (b)   (c)
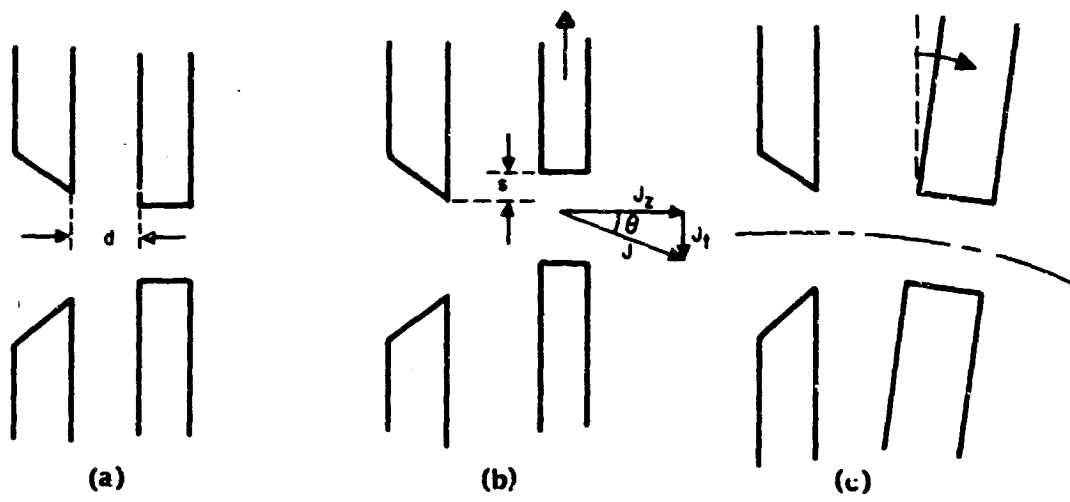
Fig. 40.   Individual modes of aperture misalignment.

The transverse displacement of the accelerator hole with respect to the screen hole by an amount s causes a deflection of the total thrust produced by the hole pair through an angle θ (see Fig. 40, case b). The total current from the hole pair is not affected, to first order, and is still governed by the distribution $J(r, d_o + \Delta d)$. The deflection angle θ is only a function of s to first order and is linear for small values of s. Accordingly, with Δs small $\theta(\Delta s) = \beta \Delta s$ where β is taken constant and equal to $0.411^\circ/\text{mil}$. The densities of the axial and transverse components of the currents produced by a hole pair with sidewise misalignment Δs are then given by

$$J_z(r, d_o + \Delta d, \Delta s) = J(r, d_o + \Delta d) \cos \theta(\Delta s)$$

$$J_t(r, d_o + \Delta d, \Delta s) = J(r, d_o + \Delta d) \sin \theta(\Delta s) \quad .$$

The magnitude and direction of the thrust from a single engine will now be calculated for a number of modes of electrode misalignment. Superposition of the contributions from each hole pair is achieved by integrating the current densities J_z and J_t over the emitting electrode area. The misalignments considered will begin with the simplest, uniform spacing change, and progress to nonaxisymmetric electrode spacings.

1. Axisymmetric Electrode Misalignments

For axisymmetric electrode misalignments the current densities $J_z(r, d_o + \Delta d, \Delta s)$ and $J_t(r, d_o + \Delta d, \Delta s)$ are constant on rings of radius r. Different modes of misalignment can be described by choosing Δd and Δs as functions of r.

Case 1. $\Delta d = \text{constant}, \quad \Delta s = 0$

The simplest case corresponds to uniform spacing. The total thruster current is axial and is given by

$$I = \left(\int_0^{r_0} 2\pi \, rJ(r, d_0) \left\{ 1 + \alpha \Delta d \right\} dr \right) \cdot f_A$$

$$I = I_0 \left\{ 1 + \alpha \Delta d \right\}, \quad \Delta d = \text{constant} \; .$$

The total engine thrust is $T(\Delta d) = T_0 \left\{ 1 + \alpha \Delta d \right\}$ where T_0, the total (unperturbed) engine thrust, is related to I_0 by $T_0 = k\sqrt{V} \, I_0 = (21 \ 25)$ $(1.2 \ A) = 25.5 \ \text{m-lb}$.

Case 2. $\Delta d = 0, \quad \Delta s \neq 0$

The second case corresponds to a transverse displacement of the accelerator electrode with respect to the screen electrode through a distance Δs. Now the hole current densities are

$$J_z = J(r, d_0) \cos (\beta \Delta s)$$

$$J_t = J(r, d_0) \sin (\beta \Delta s)$$

and the total axial and transverse thrust components are

$$T_z = T_0 \cos (\beta \Delta s)$$

$$T_t = T_0 \sin (\beta \Delta s) \quad .$$

Case 3. $\Delta d = \text{constant}, \quad \Delta s = r\phi \; .$

The third case corresponds to rotating the accelerator grid about the thrust axis through an angle ϕ.

In this mode of misalignment all accelerator holes at radius r are rotated through an arc length $r\phi$, where ϕ is measured in radians. A ring of hole pairs misaligned in this mode will produce axial thrust and a torque about the z axis. The total axial thrust from the engine is

$$T_z(\phi, \Delta d) = k\sqrt{V}\left(\int_0^{r_0} 2\pi r \, J(r, d_0 + \Delta d) \cos(\beta r\phi) \, dr\right) f_A$$

The total torque produced by the thruster is

$$\tau_z(\phi, \Delta d) = k\sqrt{V}\left(\int_0^{r_0} 2\pi r^2 \, J(r, d_0 + \Delta d) \sin(\beta r\phi) \, dr\right) \cdot f_A$$

For the values of ϕ of interest the argument $\beta r\phi$ remains small (less than 7^0); thus the approximations

$$\cos\theta = 1 - \frac{\theta^2}{2}$$

$$\sin\theta = \theta$$

may be used to simplify the integrals. Both integrals can then be carried out and yield

$$T_z(\phi, \Delta d) = T_0(1 + \alpha\Delta d)\left\{1 - \frac{(\beta r_0 \phi)^2}{2}\left(\frac{\overline{J}_0 - J_1}{J_0 - J_1}\right)\right\}$$

$$\tau_z(\phi, \Delta d) = r_0 T_0(1 + \alpha\Delta d)\left\{\beta r_0 \phi\left(\frac{\overline{J}_0 - J_1}{J_0 - J_1}\right)\right\}$$

where the angle $\beta r_0 \phi$ is in radians.

$$\text{Case 4.} \quad \Delta d = d_o \left\{ p \left(1 - \left(\frac{r}{r_o} \right)^2 \right) \right\}, \quad \Delta s = 0$$

The fourth case corresponds to a thermally warped set of electrodes whose shapes are parabolas of revolution. This mode of misalignment will occur in operating thrusters and has been discussed in Section III. The electrode spacing $d(r)$ is the difference between the screen and accelerator positions $z_s(r)$ and $z_a(r)$. For parabolic electrode shapes the functions $z_s(r)$ and $z_a(r)$ have the form

$$z_s(r) = p_s \left(1 - \left(\frac{r}{r_o} \right)^2 \right) d_o$$

$$z_a(r) = d_o \left\{ 1 + p_a \left(1 - \left(\frac{r}{r_o} \right)^2 \right) \right\}$$

and

$$d(r) = z_a - z_s = d_o \left\{ 1 + (p_a - p_s) \left(1 - \left(\frac{r}{r_o} \right)^2 \right) \right\}.$$

Since the screen warps more than the accelerator, $p_s > p_a$. We therefore take $p = p_s - p_a > 0$ and use the above representation of $d(r)$ in this case. The entire engine thrust will be axial but the magnitude will depend on the differential bowing which is characterized by the parameter p. The total engine thrust is

$$T_z(p) = \left(k\sqrt{V} \int_0^{r_o} 2\pi r \, J(r, d_o + \Delta d) \, dr \right) f_A$$

where

$$\Delta d = - p \left(1 - \left(\frac{r}{r_o} \right)^2 \right).$$

After carrying out the integral we obtain the formula

$$T_z(\phi) = T_o \left\{ 1 - \alpha d_o p \left(\frac{J_o - \bar{J}_o}{J_o - J_1} \right) \right\}.$$

2.   Nonaxisymmetric Misalignment

It has been experimentally observed that the thermal deformation which occurs when electrodes are heated is not entirely symmetrical about the central axis. This occurs because all the sheet stock from which the electrodes are manufactured is formed by rolling and therefore has a "grain." This exists even after thorough annealing and stress relieving and causes a cylindrical mode of warping for the electrodes. While it is not possible to predict analytically the extent to which this component will be present, it is desirable that the effects of such cylindrical curvature be documented. This will permit the proposed measurements of thrust deflection and electrode shape to be correlated.

Expressions for the axial positions of the electrodes in this mode of misalignment are

$$z_s = d_o \lambda_s \sin \frac{\pi \eta}{r_o}$$

$$z_a = d_o \left(1 + \lambda_a \sin \frac{\pi \eta}{r_o} \right)$$

where η is a rectangular coordinate in the direction of roll in the electrode material. The spacing between electrodes is then

$$d = z_a - z_s = d_o \left\{ 1 - (\lambda_a - \lambda_s) \sin \frac{\pi \eta}{r_o} \right\}.$$

96

Assuming that $\lambda_s > \lambda_a$, we let $\lambda \equiv \lambda_s - \lambda_a > 0$ and have

$$\ell = d_o \left\{ 1 - \lambda \sin \frac{\pi \eta}{r_o} \right\} .$$

Since the electrode spacing is symmetrically distributed about d_o the total engine thrust is T_o. The thrust intensity is increased on half of the electrode (for $\eta > 0$) and decreased on the other half. The center of thrust is therefore shifted to a new off axis location $(0, \eta_o)$.

When written in the transverse coordinate system (ξ, η) the integral for the thrust vector displacement η_o is

$$\eta_o = \frac{k\sqrt{V}}{l_o} f_A \int_o^{2\pi} \int_o^{r_o} \eta J \left\{ r, d_o \left(1 - \lambda \sin \frac{\pi \eta}{r_o} \right) \right\} r \, dr \, d\nu$$

where $\eta = r \sin \nu$, as is shown in Fig. 41. The (ξ, η) coordinate system is introduced for the convenience of having the thrust vector displacement along one axis (η). In general, the (ξ, η) system will be rotated by an angle ν_o from the thrust stand coordinates (x, y). If $(\Delta x, \Delta y)$ denotes the location of the shifted center of thrust in (x, y) system, then Δx and Δy are given by

$$\Delta s = \eta_o \sin \nu_o$$

$$\Delta y = \eta_o \cos \nu_o .$$

The angular integral in the expression for η_o can be carried out to give

$$\eta_o = - 2d_o r_o a \lambda \frac{J_o}{J_o} \int_o^1 u^3 \phi_1(m) e^{-u^2 \log \frac{J_o}{J_1}} du$$

97
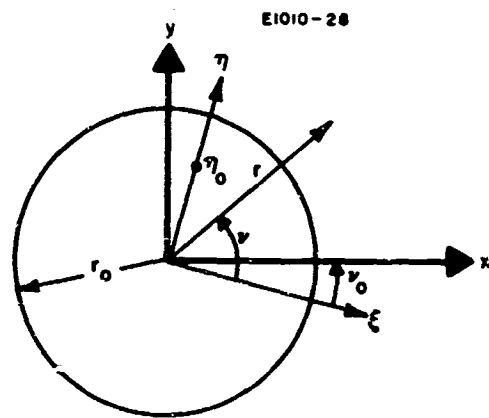
Fig. 41.
Definition of the (ξ, η) coordinate system.

where $\oint_1$ is a Bessel function of order 1, and the substitution $u = r/r_o$ was made. Finally, by evaluating this last integral numerically we obtain

$$\eta_c = -\lambda \left\{ (0.1)d_o \; r_o a \; \frac{J_o}{\overline{J}_o} \right\}.$$

C. Expected Thrust Vector Perturbations

A summary of single engine thrust vector perturbations caused by the five elementary modes of electrode misalignment is given in Table X. Applications of these formulas to a variety of physical situations will now be presented in order to give a feel for the implications of our study.

1. Uniform Spacing Change

The over-all effect of any axisymmetric spacing change Δd between the electrodes is a change in the (axial) thrust magnitude T_z. The relationship between T_z and Δd is linear and is characterized by the constant $a = -0.65\%/\text{mil}$ which was determined in the ion optical study. Since uniform spacing changes can be easily prevented by the electrode supports, this mode of misalignment should not present a significant problem. For an uncertainty of 2 mils in spacing (which may be due to assembly tolerances) the uncertainty in thrust magnitude is 1.3%.

2. Transverse Displacement

The transverse displacement Δs of the accelerator with respect to the screen causes an angular deflection θ in the thrust vector. For small displacements the relationship between θ and Δs is $\theta = \beta \Delta s$ where β is the constant $0.411°/\text{mil}$ which was found in the ion optical study. The expected amount of displacement is highly dependent on the particular electrode support design employed. The best technique for estimating Δs is perhaps by vibration testing. In any case, uncertainties of 10 mils (for example) relative in transverse positions of the electrodes cause uncertainties of $4°$ in thrust angle.

TABLE X

Elementary Modes of Single Engine Thrust Misalignment

1. **Uniform Spacing Change, Δd = constant**

$$d(r) = d_o + \Delta d$$
$$T_z = T_o (1 + a\Delta d)$$
$$T_t = \tau_z = \eta_o = 0$$

2. **Transverse Displacement, Δs**

$$d(r) = d_o$$
$$T_z = T_o \cos \beta\Delta s, \quad T_t = T_o \sin \beta\Delta s$$
$$\tau_z = \eta_o = 0$$

3. **Rotation About Thrust Axis, ϕ**

$$d(r) = d_o$$
$$T_z = T_o \left[1 - \frac{(\beta r_o \phi)^2}{2} \cdot \frac{J_o - J_1}{J_o - J_1} \right]$$
$$\tau_z = r_o T_o \left[\beta r_o \phi \frac{J_o - J_1}{J_o - J_1} \right]$$

4. **Parabolic Electrode Spacing, p**

$$d(r) = d_o \left[1 - p \left(1 - \left(\frac{r}{r_o}\right)^2 \right) \right]$$
$$T_z = T_o \left[1 - a p d_o \frac{J_o - J_o}{J_o - J_1} \right]$$
$$T_t = \tau_z = \eta_o = 0$$

5. **Cylindrical Buckling, λ**

$$d(\eta) = d_o \left[1 - \lambda \sin \frac{\pi\eta}{r_o} \right]$$
$$T_z = T_o$$
$$\eta_o = -\lambda (0.1) d_o r_o a \frac{J_o}{J_o}$$
$$T_t = \tau_z = 0$$

$d_o = 0.090$ in., $a = -0.65\%/\text{mil}$, $r_o = 6$ in.

$\beta = 0.411°/\text{mil}$, $T_o = 0.0255$ lbs

$J_o = 8$ mA/cm^2, $J_1 = 2$ mA/cm^2, $J_o = 4.3$ mA/cm^2

Electrode Spacing = $d(r)$; Axial Thrust = T_z; Transverse Thrust = T_t; Torque About Thrust Axis = τ_z; Displacement of Center of Thrust = η_o.

3. Rotation About Thrust Axis

A rotation ϕ of the accelerator with respect to the screen about the thrust axis causes a decrease in axial thrust T_z and a torque τ_z about the thrust axis. The expected amounts of rotation also depend highly on the electrode support design. Upon substitution into the formula for τ_z we find that

$$\tau_z = \left(4.32 \times 10^{-3} \ \frac{\text{in.-lb}}{\text{deg}}\right) \phi \ .$$

Thus, 1° of relative electrode rotation will cause a roll axis torque of 4.32×10^{-3} in.-lb.

4. Parabolic Electrode Spacing

The change in thrust magnitude has been calculated for the parabolic electrode spacing shown below

$$d(r) = d_o\left\{1 - p\left(1 - \left(\frac{r}{r_o}\right)^2\right)\right\} \ .$$
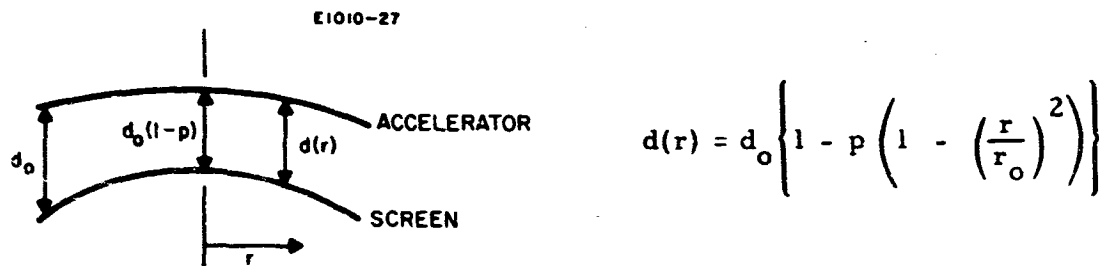
This mode of misalignment results from the thermal buckling of the electrodes. When the electrode gap decreases from d_o at the edge to $p \cdot d_o$ at the center $(p < 1)$, the change in thrust is

$$\alpha p d_o \ \frac{J_o - \bar{J}_o}{J_o - J_1} = 0.617 \ \alpha p d_o = \left(\frac{0.4\%}{\text{mil}}\right) p d_o \ .$$

Thus if $p = 1/2$, $pd_o = 45$ mils and the change in thrust is 18%.

As was discussed in Section III-B the expected amount of buckling, which we have characterized by the parameter p, is highly dependent on the initial shape of the electrodes and the amount of radial clamping by the supports. Since the dependence of p on initial shape

is nonlinear as shown in Fig. 37, and the sensitivity of p to radial constraint is severe (see Fig. 39), the uncertainty in knowing p and therefore the thrust magnitude is large.

5. Cylindrical Buckling

A particular cylindrical non-axisymmetric mode of electrode misalignment was considered because it has been observed in operating thrusters and because it apparently cannot be eliminated. The "grain" induced in the electrode material during rolling is the cause of this buckling mode. The electrode spacing is shown below

$$d(\eta) = d_o \left\{ 1 - \lambda \sin \frac{\pi \eta}{r_o} \right\}$$
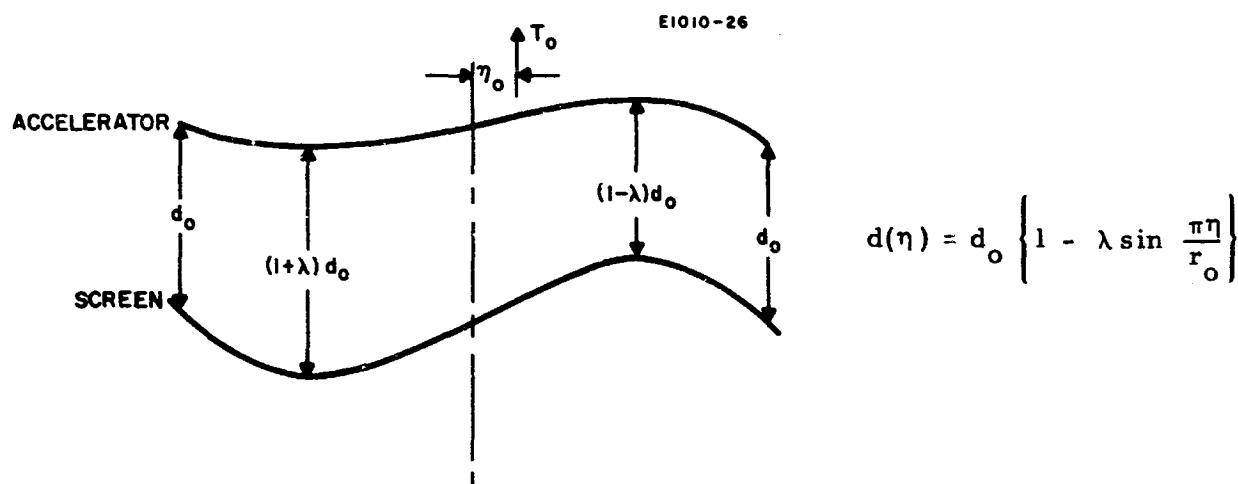
as a function of η, the direction of roll. In this mode of misalignment the thrust is axial and has magnitude T_o, but the center of thrust is displaced by an amount η_o. The relationship between λ and η_o is

$$\eta_o = (0.65 \text{ in.}) \lambda \ .$$

Thus, for $\lambda d_o = 20$ mils, $\lambda = (2/9)$ and $\eta_o = 0.145$ in.

V. THRUSTER DESIGN AND INSTRUMENTATION

A. Objectives

As discussed in Section I, this total program was naturally divided into two phases: the first comprised an analytical study of the thrust vector displacement problem and the design of experimental and measuring devices; the second phase will involve a program to construct the thrust measuring equipment and to measure the thrust direction of an engine under varying conditions. This section of the report deals with the design of the experimental system, composed of the thruster and thrust stand. The thruster should be representative of the state of the art and designed so that the electrodes can be moved relative to each other in a controlled manner in order to simulate misalignments which may occur naturally during operation. The basic requirements of the thrust stand are that it be capable of resolving the thrust direction to $\pm 1/2^\circ$ of angle and that torques about the thrust axis of 5×10^{-4} in. -lb or greater be measurable. A second experiment consists of measuring the electrode misalignments that do occur naturally during a 50 hour period and correlating them with variations in the direction of thrust. The detailed design of the various components and the way in which they will be incorporated into the total experimental system are discussed below.

B. Thruster Design

It is particularly important that the thruster designed under this task be representative of the current state of the art in terms of performance and fabrication techniques. With this in mind, the following design criteria were established.

    a.   30 cm diameter beam — based on current performance, a thruster of this size represents a power level of approximately 2 kW. Recent system studies indicate that this is a useful module size.

b.   Thermionic cathode — this cathode type was chosen to be consistent with current mission analysis and experimental studies at JPL.

c.   Lightweight construction — sheet-metal techniques are used to hold the thruster weight to approximately 11 lb.

In order to minimize the weight, the use of aluminum (versus stainless steel) was considered for the discharge chamber shell, anode, and other structural members. Stainless steel was chosen because (a) it is known to resist attack by mercury; (b) it is readily welded to the soft iron end plates, while aluminum must be rivetted; (c) no weight penalty is associated with the use of stainless steel because it may be used in very thin sections.

The estimated weights of the various components are listed in Table XI.

d.   Ion optical array — a "conventional" ion optical array consisting of a matrix of round apertures in a hexagonal close packed pattern was chosen. The following dimensions were used:

screen:	70% open area
	0.187 in. holes on 0.210 in centers
	0.030 in. thick
	molybdenum or alloy
accelerator:	apertures 0.144 in. (based on in-house HRL and JPL studies)
	maximum thickness 0.110 in. based on required 10^4 hour lifetime
	molybdenum or alloy
spacing:	nominally 0.090 in. but can be reduced to increase perveance
	a center support is proposed to improve stability

104

e.   Basic design — the basic design is a scaled version of the SERT II thruster which has been recently developed at NASA-LeRC. The most significant deviation from direct scaling is that the discharge chamber length has been held approximately constant, as suggested by a recent HRL scaling study.[6] It is anticipated that some effort will be required in the second phase of the contract to experimentally evaluate this design and to modify the magnetic field configuration to improve performance.

Based on the above criteria, the thruster shown in Fig. 42 was designed. The nominal current performance is 1200 mA (beam) at I_{sp} = 3500 sec. The total input power to the thruster as a function of specific impulse is shown in Fig. 43.

It was not part of this phase of the program to construct or test the thru 'er; the program sought only to provide the design. Near the end of the program, however, an opportunity arose to test a thruster of this size and approximate design (constructed with HAC IR&D funds) with an oxide cathode of the type proposed for use here. Stable operation was achieved on the first attempt, with efficiencies of approximately 200 eV/ion discharge losses at 85% mass utilization. The thruster was operated briefly at beam currents of 1.25 A. These preliminary data are quoted here to verify that the design is basically sound and suitable for the proposed tests.

C.   Instrumentation for Electrode Motion and Position Monitoring

Two types of experiments are proposed. The first involves moving the accelerator in known increments with respect to the screen and observing the resultant thrust deflection. This will provide a direct correlation with the analytical calculations of the preceding sections. The second experiment is to permanently mount the screen and accelerator as they would be in a flight system and observe time
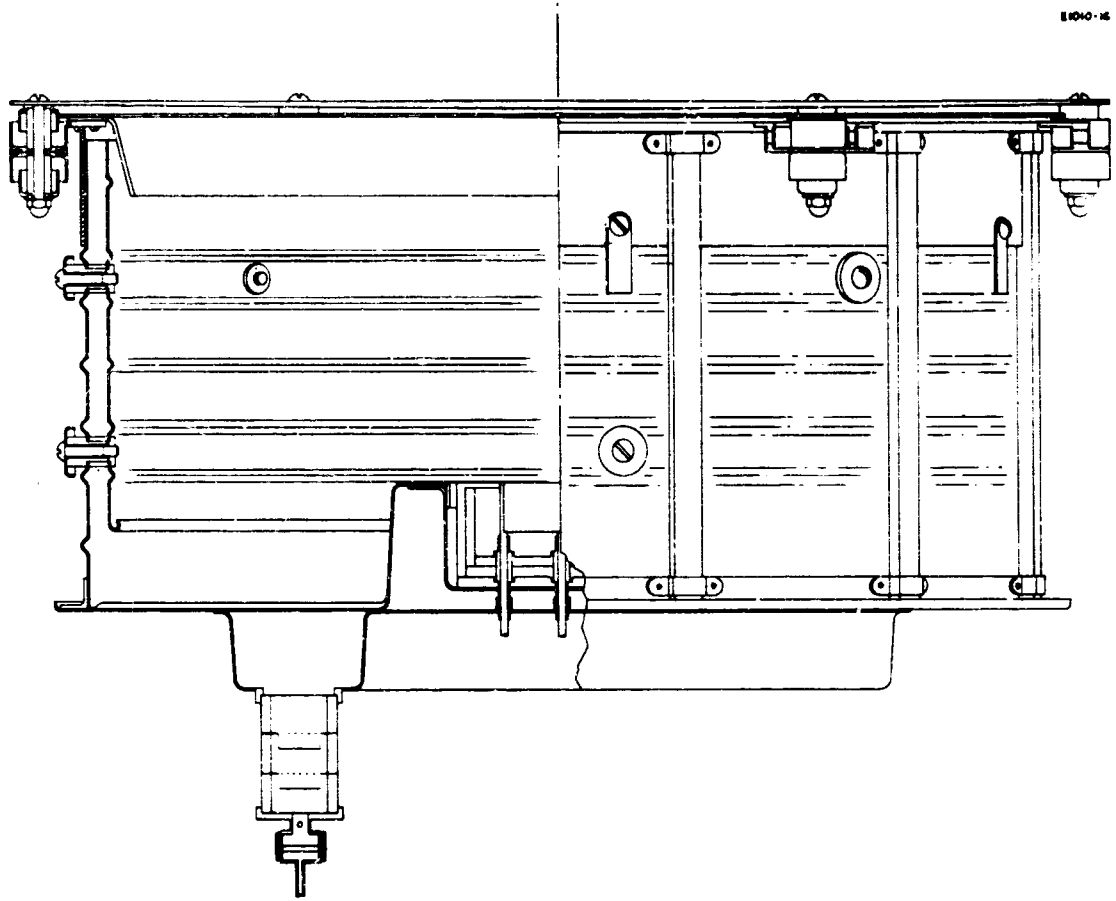
Fig. 42.   Cross sectional view of the thruster.
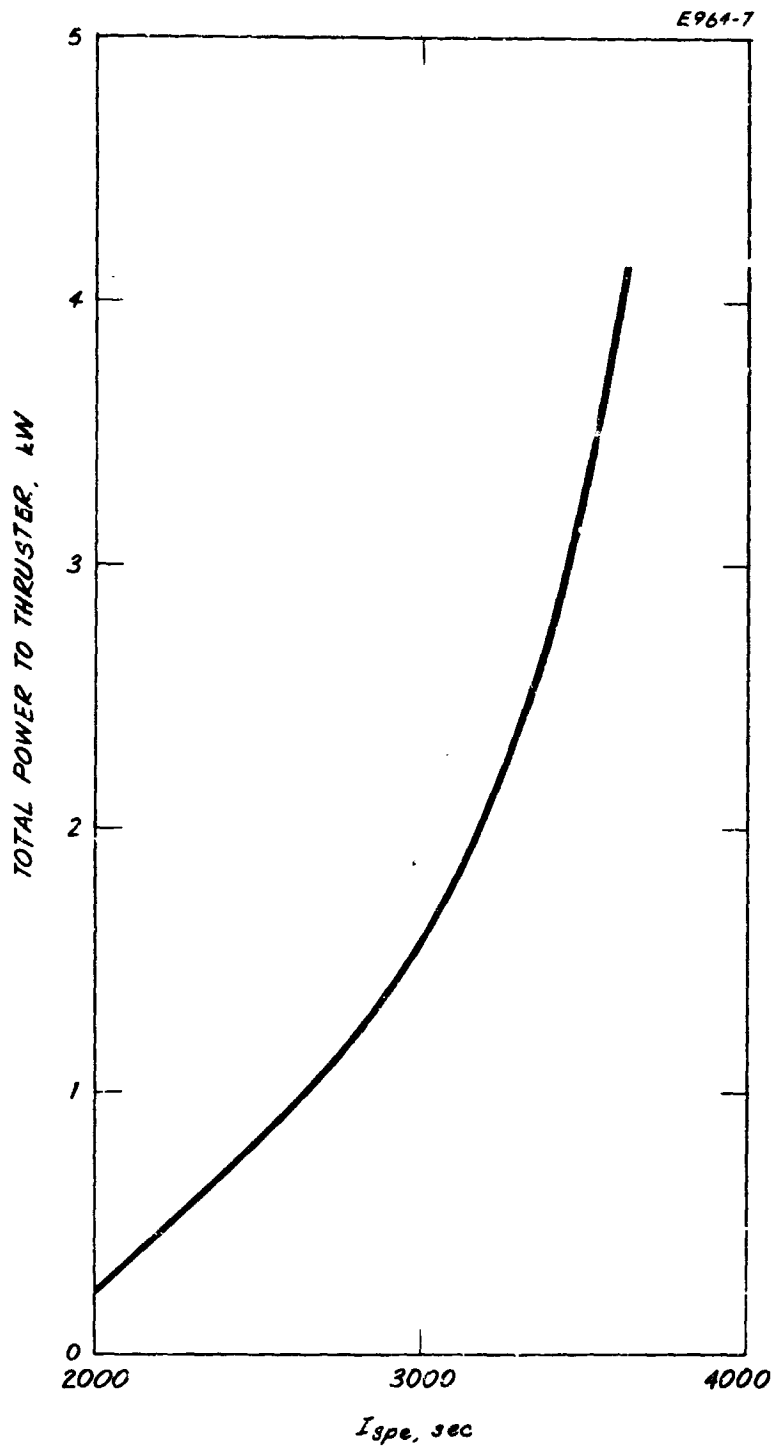
Fig. 43. Power handling capability as a function
of specific impulse.

TABLE XI

Component Weight

Part	Material	Weight, lb		
		0.010 in.	0.020 in.	Components Independent of Sheet Metal Thickness
Screen Collar	CR Steel			1.13
Lower Ring	CR Steel			0.47
Outer Shell	Stainless Steel	0.71	1.42	
Anode	Stainless Steel	0.57	1.14	
Screen Pole Piece	CR Steel			0.42
Screen Electrode	TZM Molybdenum			0.71
Accel Electrode	TZM Molybdenum			1.96
Back Plate	CR Steel	0.51	1.02	
Cathode Pole Piece	CR Steel	0.08	0.15	
Magnets	Alnico V			1.50
Insulator Assemblies				0.49
Subtotal		1.87	3.73	6.68
Total		8.55	10.41	

variations in thrust as the thruster is turned on and during a 50 hour period of steady state operation. Position monitors to measure the relative motion of the electrodes and any changes in shape that occur during the test period will be mounted on the thruster. These data will be used to corroborate the variations in thrust direction predicted by the structural analysis of the system coupled with both the analytical and experimental studies of ion beam deflection discussed earlier.

1.   Motion Generator

To conduct the experiment it is necessary to move the accelerator laterally as well as axially in increments of approximately 0.005 in. over a range of 0.020 in. It is also necessary to rotate the electrode about the thruster axis such that the periphery moves a similar amount. It is desirable that the motion be precalibrated and that a ratchet action be used so that the electrode will stay in position once it is moved without requiring a high degree of thermal or electrical stability in the actuator.

A straightforward means of accomplishing this is shown i.·Fig. 44. It consists of a cylindrical cam driven by a solenoid. An overriding clutch is mounted so as to lock the shaft after each impulse and provide ratcheting . on. During the development a thermal driver unit was constructed to perform the function of the solenoid. It consisted of a stack of bimetal washers formed into truncated cones. The driving action was much smoother with this device than with the solenoid; however, the cooldown time required between cycles was too long (>30 min) to permit convenient experimentation. Based on this fact the solenoid driver was selected for the final design.

As shown in the layout in Fig. 45, five of these units will be mounted on the thruster to control the accelerator position with respect to the screen.

ACCEL
ELECTRODE
INSULATOR
MTG RING

SOLENOID
PULL ROD

CAM

BEARING

SOLENOID

OVERRUNNING CLUTCHES
ARROW INDICATES
DIRECTION OF FREE
ROTATION
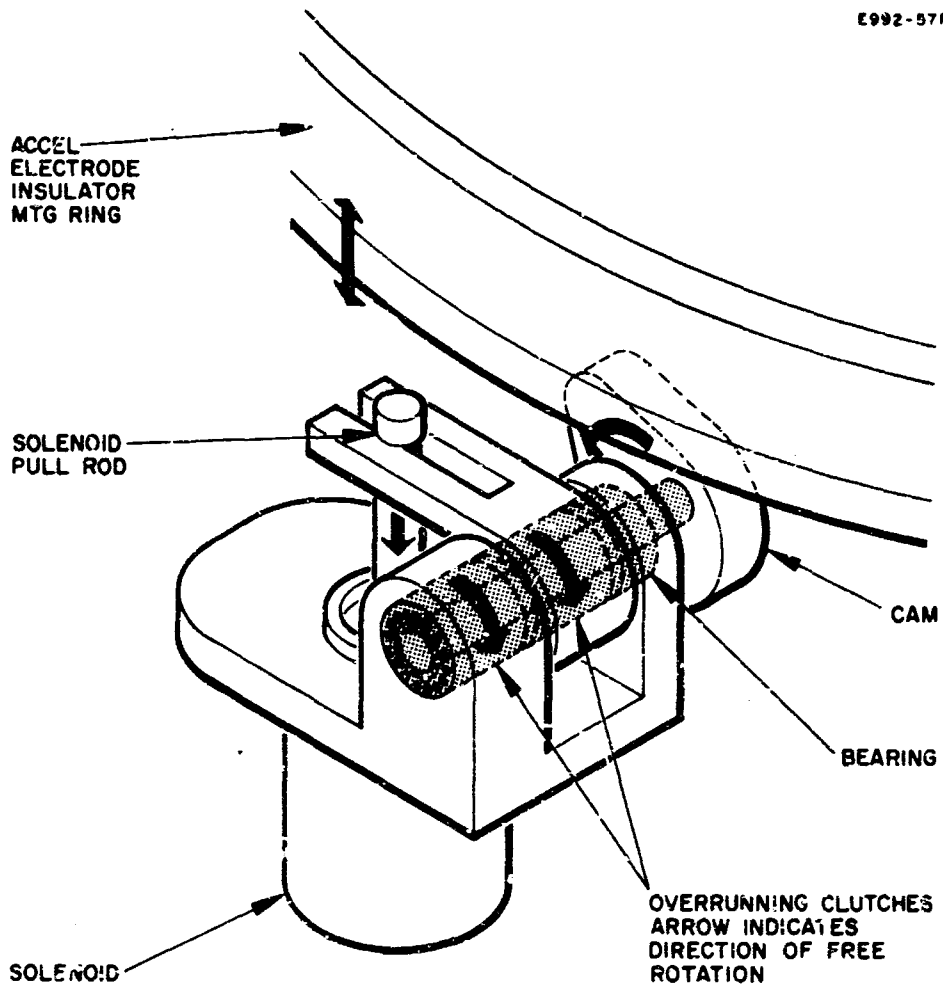
Fig. 44.   Electrode motion actuator.
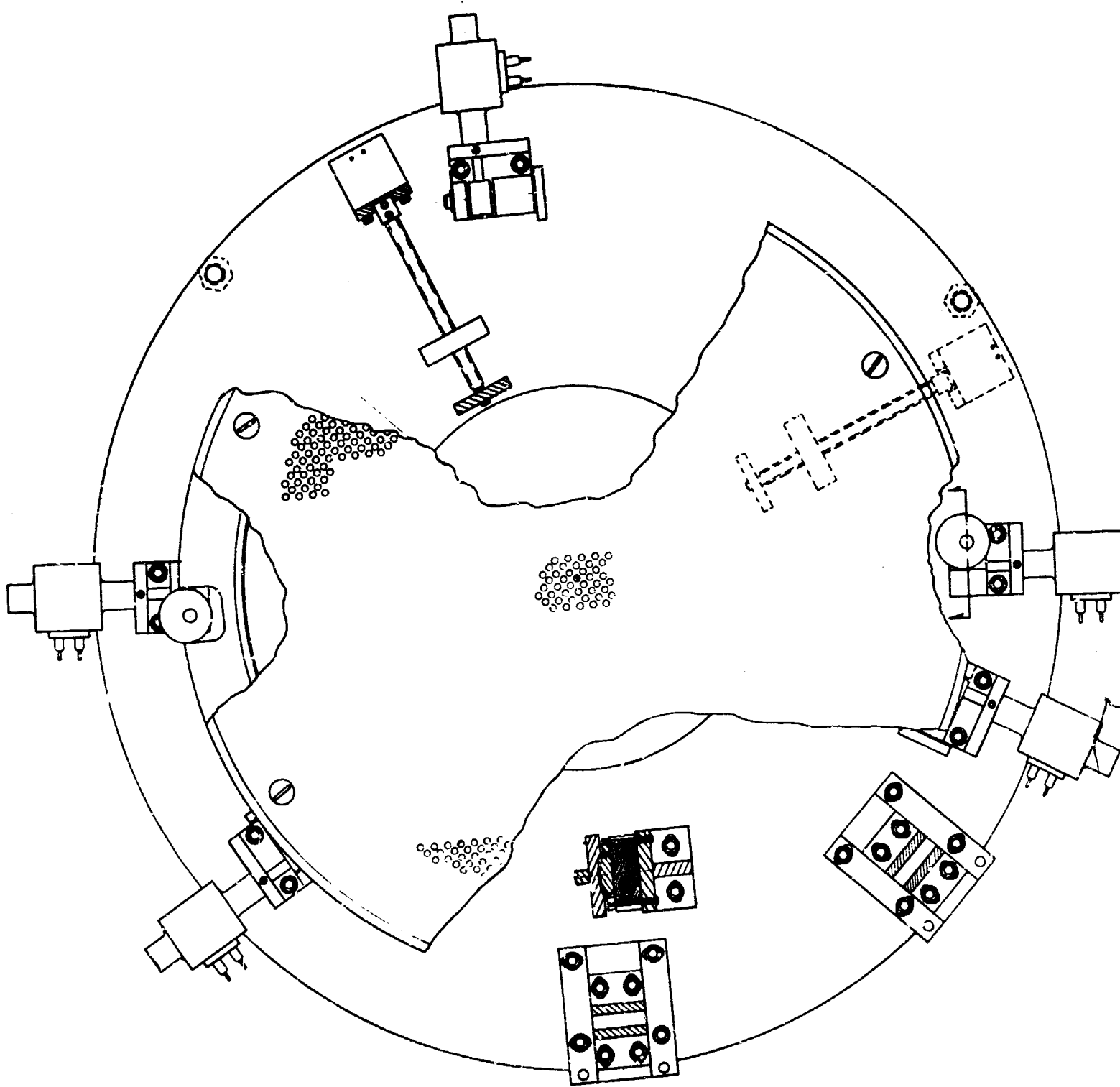
Fig. 45. Preliminary layout-floating suspension thrust stand and

111
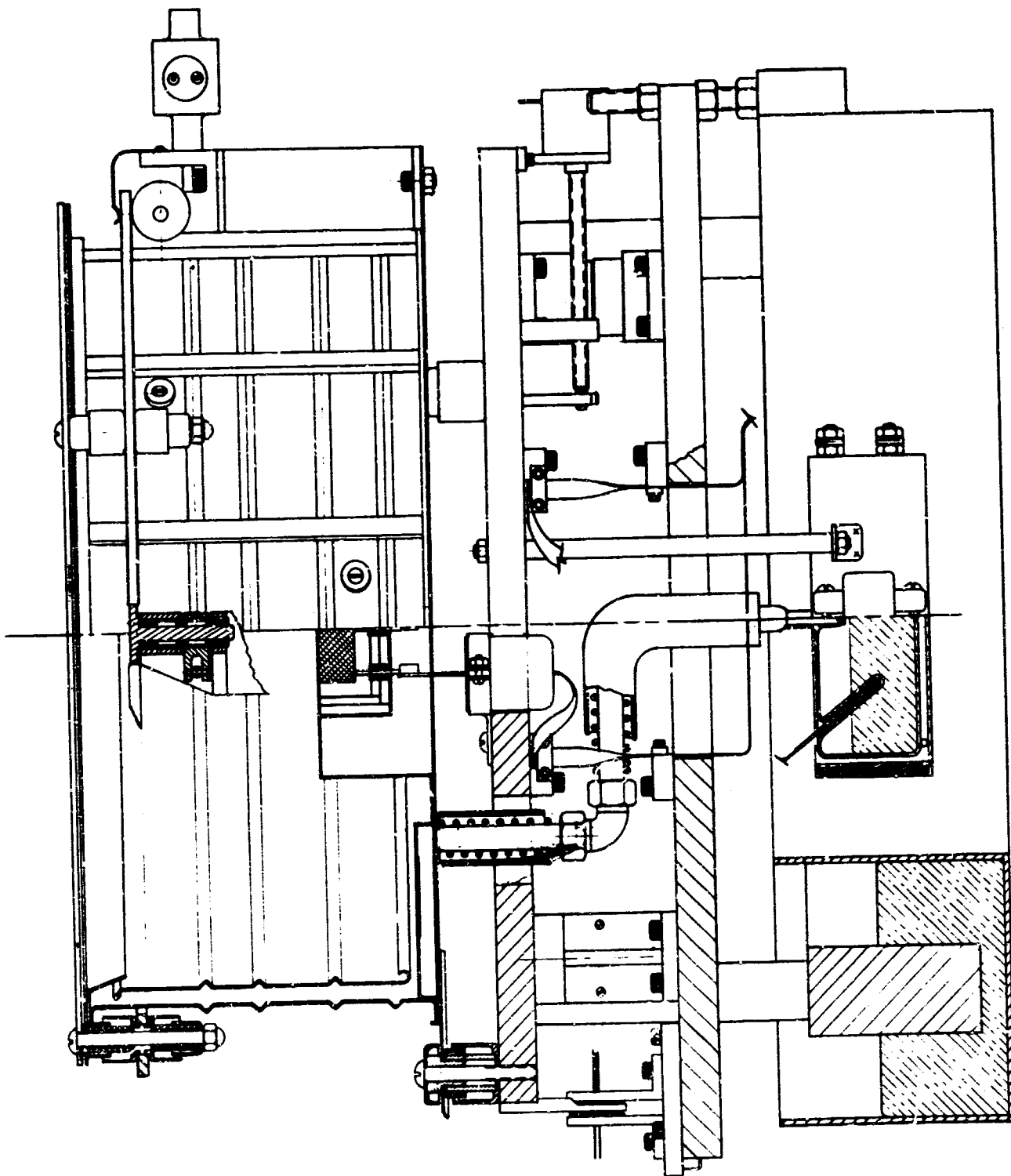
nd and 30 cm thruster with accel electrode motion generators.

2.   Position Monitor

Two types of position monitor are required. The first must measure the axial alignment of individual apertures in the screen and accelerator electrodes and the second the actual contour of the electrode surfaces. These measurements must be made in vacuum on a thruster while it is operating.

It was initially proposed that a light beam be used for each of these measurements. Differential detectors are available which may be used to monitor the motion of a collimated beam of light to a few thousandths of an inch. Further investigation indicated, however, that the task can be done more simply with a differential transformer of the type sold by Automatic Timing and Controls Inc. (Type 6234). One such transformer was purchased, tested, and found to provide a response of

$$\frac{1.8 \text{ mV}}{(0.001 \text{ in.})(\text{primary volt})}$$

Further experiments indicate that cross coupling between motions in the orthogonal direction is attenuated by at least an order of magnitude.

Measurement of the electrode surface contours while the thruster is operating represents a relatively difficult task. It is proposed to accomplish this as shown in Fig. 46. A series of short pins will be set in the accelerator surface across a diameter. The relative positions of these pins will be observed from outside the vacuum chamber with an alignment telescope[*] capable of directly reading position to 0.001 in. over a ± 0.050 in. range. The screen position may be similarly monitored by mounting pins on the existing holes in the accelerator electrode. By blocking 10 to 15 of the nearly 3000 holes in the electrodes, a reasonably good measure of the electrode

---

[*]K&E type 712020 available at HRL.

113

E964-A

ACCEL.

SCREEN
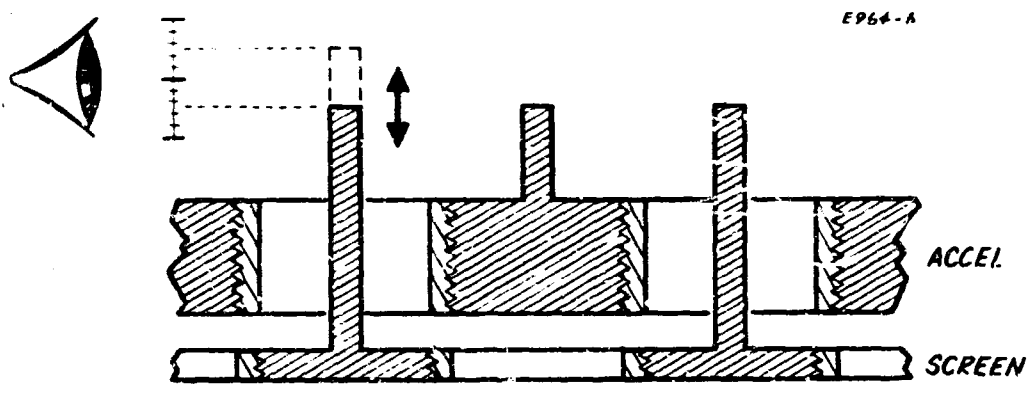
Fig. 46. System to measure electrode warping.

profile is possible. It will be necessary, of course, to block apertures symmetrically about the centerline so that thrust perturbations do not result.

D.   Thrust Stand

In order to carry out the experimental verification phase of this program, a device is required to measure the location of the thrust vector from the thruster described above to within $\pm 1/4^{\circ}$ of angle and to determine whether any couple exists about the thrust axis to an accuracy of 5×10^{-4} in. -lb. Competitive methods of making this measurement were analyzed. Conventional techniques for measuring either thrust or ion trajectories are investigated first. Each of these (viz., scanning Faraday cups, torsion wire suspension, and ion beam collection reaction) were eliminated for this application. At this point two new concepts of thrust measuring system were considered.[*] It appears that each has sufficient sensitivity to measure the thrust vector directly, but that one may possess some inherent advantages. The systems considered are discussed below.

1.   Scanning Faraday Cup

The basic concept here is to use a Faraday cup to establish the number and direction of the ions at each point in the beam and from this information to infer the thrust direction. As with all the methods compared the limiting accuracy must be $\pm 1/4^{\circ}$. A fundamental problem associated with the various ways in which this general technique may be applied is that the ions in the beam do not follow laminar trajectories. For this reason, it is necessary actually to measure the direction that the ions are traveling at each point.

The most direct way to accomplish the above is to make the measurements at a point sufficiently far downstream that the actual source

may be approximated by a point source. With the above required accuracy, the source must subtend an angle less than $1/2^{\circ}$ at the cup. For a 30 cm diameter thruster this gives a beam path length well over 100 ft. Not only are facilities of this size not available, but scattering in the beam would make the results uncertain.

The second possibility is to employ a Faraday cup relatively close to the thruster. The cup must now be designed to accept only ions which have emanated from an area on the source which subtends a $1/2^{\circ}$ angle or less at the collector. In other words, the cup must be preceded by a very narrow angle collimator. In principle at least, this device may now be used to measure experimentally the beam intensity as a function of angle (between Faraday cup beam axis) at each point in the beam. This measurement technique of course would generate an enormous amount of data. The experiment is difficult not only because of the accuracy required to position and control the location of the cup, but also because of the low signal level available ($\sim 10^{-8}$ A) after the selective collimation. Actually reconstructing the thrust vector from such measurements would no doubt require considerable computer analysis.

Another important factor which mitigates against this method is that collection of the data to establish a single thrust vector might require several hours, a period which may be much longer than the stability of either the measuring equipment or the thruster.

In summary, it does not appear practical to construct the thrust vector to the desired accuracy from detailed measurements of ion trajectories in the beam. The principal difficulties arise from the very large amount of information required to define the beam with sufficient accuracy.

2.   Torsion Wire Systems

The basic concept here is to hang the thruster from a thin wire and then measure the angle through which the wire twists because of the torque created by unbalanced forces. A number of

variations of this general idea, such as suspending the thruster between two wires (as in a taut wire galvinometer) and using nulling techniques to maintain the net angular deflection at zero, all fall into this same general category.

With this type of suspension system it is conceptually possible to measure torques of the magnitude of interest here (5×10^{-4} in.-lb). However, there are a number of practical difficulties which seriously limit the application of the technique.

● Electrical Leads — A number of electrical connections must be made to the thruster. Each of these will stiffen the suspension and reduce sensitivity. A possible solution is to allow each lead to dip into a separate mercury pool, thus providing a friction free contact. It is very difficult to estimate the chance of success of this technique; it is at best a very cumbersome one.

● Stability — This arrangement is very susceptible to pendulum type instabilities. In principle, these can be damped out, but only with a sacrifice in over-all system response.

● Nulling Mechanism — Considering the device as a simple pendulum, it may be shown that the engine thrust (25 mlb) will cause motions of the thruster system of the same order of magnitude as those created by the torsional forces about the wire axis which we are trying to measure. This system thus requires a relatively sophisticated nulling system which automatically balances the main thrust vector at all times while at the same time measuring the much smaller (by a factor of approximately 100) force necessary to compensate for the thrust variation which we wish to measure.

● Interpretation of Data — A system such as this would be designed to measure only the torque about the axis of the suspension wire. Inherent in the system are a number of other degrees of freedom which may be excited by perturbations in the thrust direction. Coupling between these may make interpretation of the experimental results very difficult.

In summary, while this type of system conceptually has just sufficient sensitivity to measure the torque specified (5×10^{-4} in.-lb), a number of practical problems make application of the basic principle difficult, if not impossible.

3.   Collectors

Under ideal circumstances it is possible to measure thrust produced by an ion thruster by measuring the effect of the impinging ions on a collector. The principal practical difficulties which arise are associated with the dissipation of the beam power (~ 2 kW must be carried away from the collector by some type of forced cooling system, usually water). It is impractical to consider water leads with sufficient flexibility to permit the collector to respond to thrust levels of the magnitude of interest here. Therefore, it is not possible to measure the thrust direction by observing the reaction of the collector to the thrust.

4.   Stiff Column Thrust Stand

The heart of this design is an extremely sensitive tiltmeter recently developed at HRL which is capable of resolving deviations of 10^{-9} rad from the horizontal. The basic concept is illustrated in Fig. 47. The thruster is so positioned that both the gravitational vector and the nominal thrust vector are parallel and lie along the axis of a slender hollow column which both supports the test package and contains the necessary electrical leads to operate the thruster. The base of the column is supported on a massive platform stabilized by a servo loop which is controlled by a tiltmeter. A second tiltmeter mounted on the platform supporting the thruster monitors small angular fluctuations which occur when variations in thrust direction cause the slender column to deflect.

The sensitivity of this system may be estimated as follows. The angular deflection of a slender column is given by
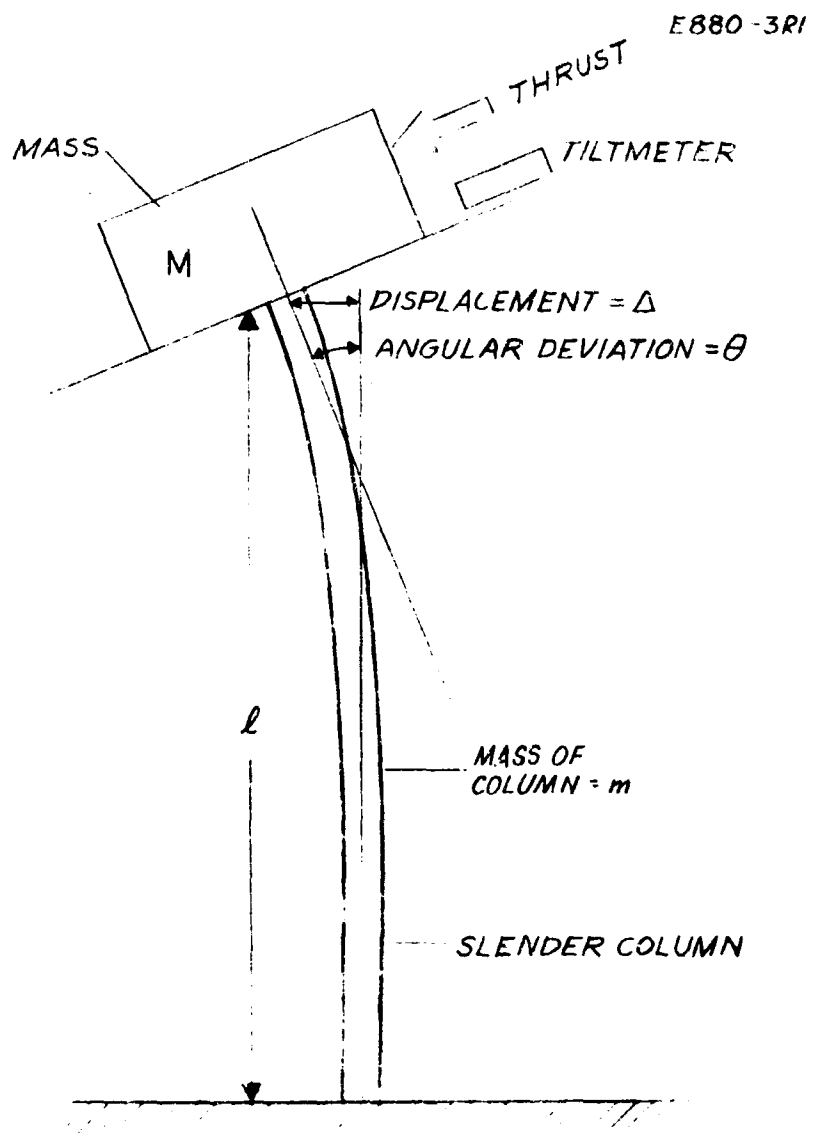
Fig. 47. Basic thrust measuring concept.

$$\Theta = \frac{1}{2} \frac{F\ell^2}{EI} \text{ rad}$$

where

$F \equiv$ force perpendicular to column

$\ell \equiv$ length of column

$E \equiv$ modules of elasticity

$I \equiv$ moment of inertia of cross section of column.

For a 6 in. long quartz rod, 1/4 in. in diameter, used in the proposal, $\Theta = 10^{-2} F$. With the sensitivity of 10^{-8} rad specified for the tiltmeter, forces of 10^{-6} lb may be detected.

The basic concept of monitoring the position of a flat "pancake" shaped bubble formed in a liquid under a flat plate, which is the heart of the tiltmeter design, may be employed in two ways to achieve the desired result here. The first (Fig. 48) is to provide a servo system to maintain the platform on which the thruster is mounted in a level position using the bubble as an accurate null indicator. If the servo loop has been precalibrated it may be used to directly read out the force necessary to counteract that resulting from thrust deviations. The second (Fig. 49) technique is to use a complete tiltmeter which includes not only the bubble sensor but the necessary suspension and servo system to maintain the bubble in a level position on a moving platform and to indicate table declination directly.

A detailed design of a representative system of this type was presented in the first quarterly report under Phase I of this contract. It was demonstrated that a 12 in. long stainless steel tube, 3/4 in. o.d. with a 0.020 in. wall would serve satisfactorily to support a 32 lb load while providing the required flexibility for use with a standard HAC 4 in. diameter tiltmeter. A mathematical analog was developed in the above quarterly report which indicated that with typical values a 19 mV signal would be available at the minimum thrust deviation of $1/4^{\circ}$. The frequency response can be made essentially linear up to 1 cps.

120
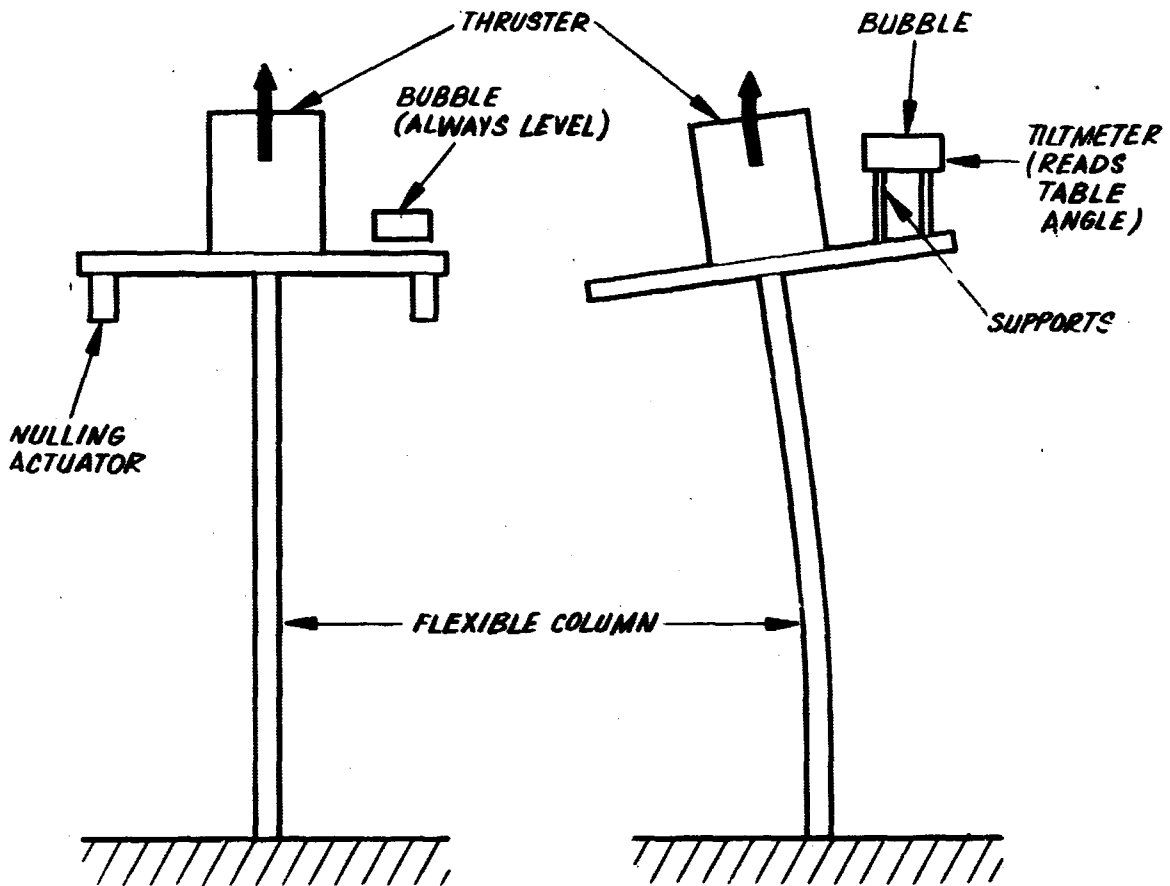
Fig. 48. Null producing system.

Fig. 49. Measurement of angular deflection.

Figure 50 depicts the perturbing forces associated with the misalignment of the thrust vector and the center of mass. Ideally, these forces should act along the axis of the supporting column. Displacements of these two forces from the ideal position are represented by x and y, respectively, in Fig. 50. The column of length ℓ is supported on an accurately level table and makes an angle β with the horizontal. Assume first that $\beta = 90^\circ$ and that the two perturbing torques (taken about point A at the base of the column) are

$$L_1 = (T \cos \alpha)(x)$$

$$L_2 = Mg \, y$$

where

$$M \equiv \text{mass of the system (assume 25 lb)}$$
$$T \equiv \text{total thrust (assume 0.025 lb)}$$
$$\alpha \equiv \text{thrust deviation } (\geq 1/4^\circ).$$

The torque produced by the thrust component that we wish to measure is

$$L_3 = T(\sin \alpha)\ell$$

where ℓ = column length (assume 12 in.). To assure that $L_3 > L_1$ and $L_3 > L_2$, we must have

$$\therefore \; x < 0.050 \text{ in.}$$

and

$$y < 5 \times 10^{-5} \text{ in.}$$

Fig. 50. Perturbing forces.

These calculations show that there is a relatively large tolerance on the alignment of the thrust vector with the axis of the supporting column, while very little shift in center of mass position is permissible.

Consider first the thrust vector misalignment. For a perfectly symmetrical thruster the thrust vector should pass through the exact center of the ion optical system. This can certainly be specified to better than the 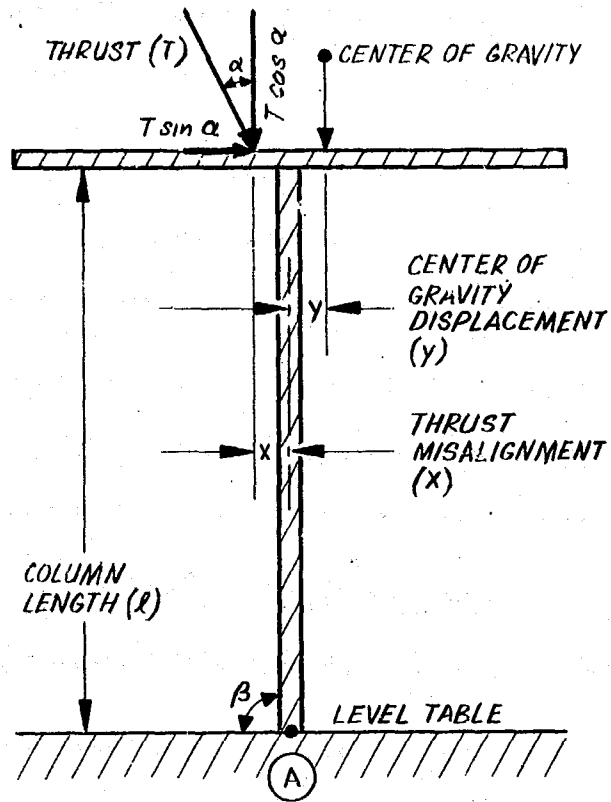0.050 in. permissible error calculated above. Determining the probability that a shift of this magnitude will occur during testing should be one of the goals of the analytical study. It is fortunate that reasonable lateral shifts in the thrust vector location are tolerable, because it is not possible to separate the two torques L_1 and L_3 by varying the total thrust, since each varies directly with the thrust magnitude and angle. The only other variable which even in principle permits the separation of the two effects is the misalignment x. As shown below, this cannot be adjusted during a run because of the very large effects associated with shifting the position of the center of mass.

The force on the thrust table due to gravity acting on the center of mass of the table and its load (the thruster, etc.) must pass accurately through the pivot point A at the base of the support column. Since neither the center of mass nor the pivot point can be located to the necessary accuracy, a technique for mechanically balancing the system is required. The location of the thrust vector physically defines where the thruster must be located with respect to point A; therefore, balancing must be done by the addition of weights to the table, possibly using one of the many techniques developed for modern analytical balances. Final precision balancing may be done with automatic nulling incorporated into the system to maintain the bubble level during the test.

Small shifts in the center of mass may occur during operation because material is being removed from or deposited on the ion source or its supporting structure. Other center of mass shifts may inevitably occur when the electrodes are moved with respect to each

other as part of the experimental program. These latter effects can
be calculated and also measured directly by shifting the electrodes
with no beam extraction and thus may be subtracted from the observed
thrust deviation to give the true reading. Because the electrode mass
and the amount of motion will be known, it is also possible to compen-
sate for the center of mass motion by moving an equivalent weight in
the opposite direction. The permissible tolerance for angle β may
be directly calculated once the column length ℓ is fixed.

5.   Floating Suspension Thrust Stand

        This new concept of thrust stand uses a suspension
mechanism which permits the three components of the thrust and the
torques about the three mutually perpendicular axes to be measured[*]
at the same time. The thruster platform is floated in a mercury pool
and is free to drift horizontally or to lean away from the vertical,
depending on forces applied. It is also possible for the system to
rotate about its vertical axis if a couple exists about this axis. As
discussed below, the suspension must be carefully designed to assure
stability and to assure that the suspension itself introduces minimum
perturbations into the system.

        The operation of the system may be understood by referring to
Fig. 51, which shows a two dimensional sketch of the essential elements
of the device, and Fig. 52, which illustrates the two types of thrust
misalignment which may occur. The mercury surface remains
horizontal, thus removing the necessity of placing the entire apparatus
on a stable table, as in the previous design. In operation the table is
releveled by the force motors F_z, using the tiltmeter as a reference,
while horizontal and rotational motion is arrested by the force motors
F_x and F_r, respectively. The position monitors which establish these
null positions are not shown.

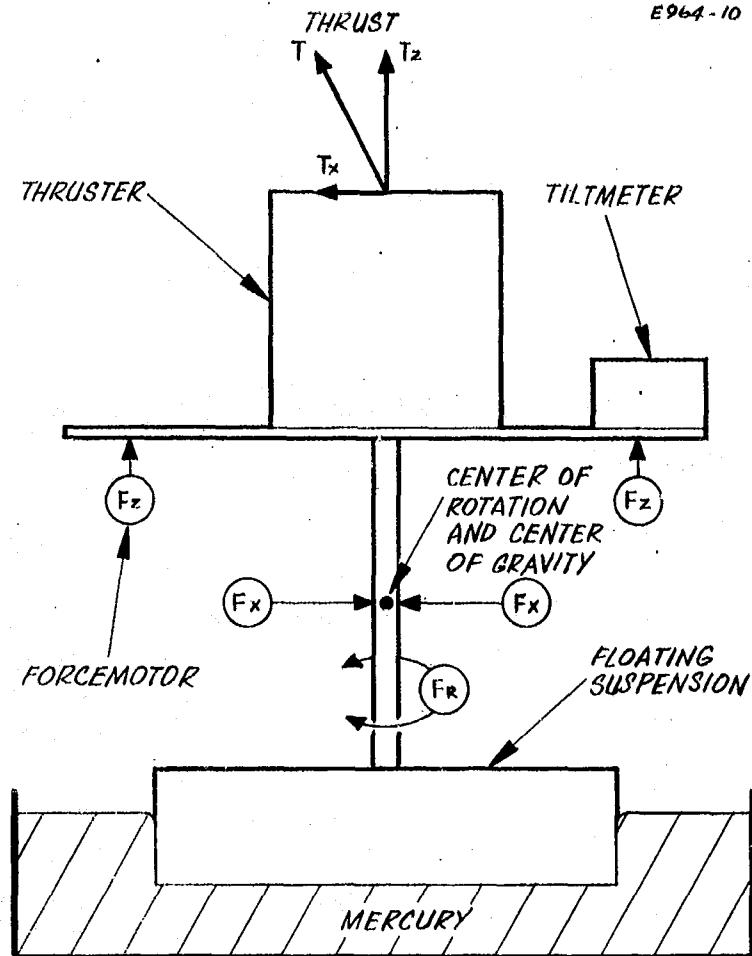[*] The total thrust is calculated from electrical measurements.

THRUST

E964-10
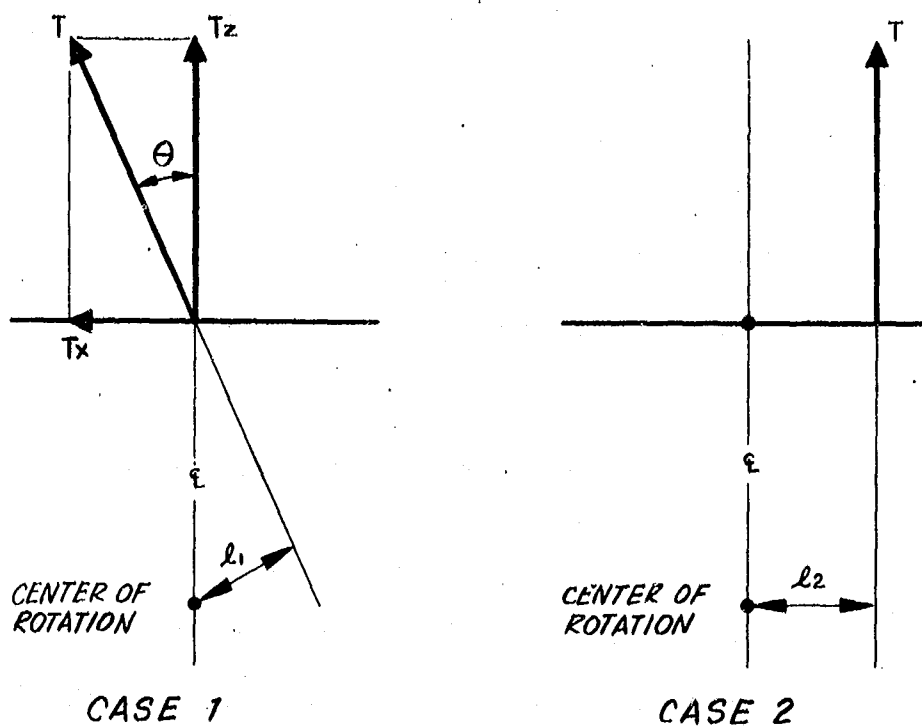
Fig. 51. Sketch of floating suspension device.

126

Fig. 52. Two types of thrust misalignment.

Consider first case 1 of Fig. 52. Here the thrust vector is at an angle θ with the desired direction along the centerline. It is apparent that such a force tends both to tilt the platform and to move it horizontally. To resolve such a force, force motors F_z level the platform and the force motor F_x compensates for the horizontal drift. Next, consider case 2 of the same figure, which illustrates a situation in which the thrust vector has moved laterally while remaining parallel to the centerline. Notice that if $\ell_1 = \ell_2$, the same torque is produced about the center of rotation, as in case 1. However, there is no lateral force in the second case.

The primary advantages of the floating suspension are (1) that it resolves the two possible types of thrust misalignment illustrated in Fig. 52 and (2) that a single experimental setup measures both angular deflections of the thrust vector and torques set up about the centerline or nominal thrust axis. Figure 53 illustrates the proposed suspension mechanism which provides the additional degrees of freedom.

It is desirable to design the floating suspension system so that the buoyant force of the mercury supports the platform but does not tend to force it to maintain a particular position. In other words, by proper mechanical design the system may be made critically stable so that the buoyant forces tend neither to right it or to upset it. The design criteria which define such a neutral system were described in an earlier quarterly report.

The preliminary design of the system incorporated a bubble sensor, such as is used as the sensing mechanism on the HAC tiltmeter, to sense the table position with respect to the horizontal. It was subsequently recognized that it is not necessary to maintain the table accurately horizontal at the null position when the neutrally stable suspension described above is achieved. By using linear position sensors referenced to the platform supporting the mercury reservoir to monitor the motion of the floating table in the vertical (z)
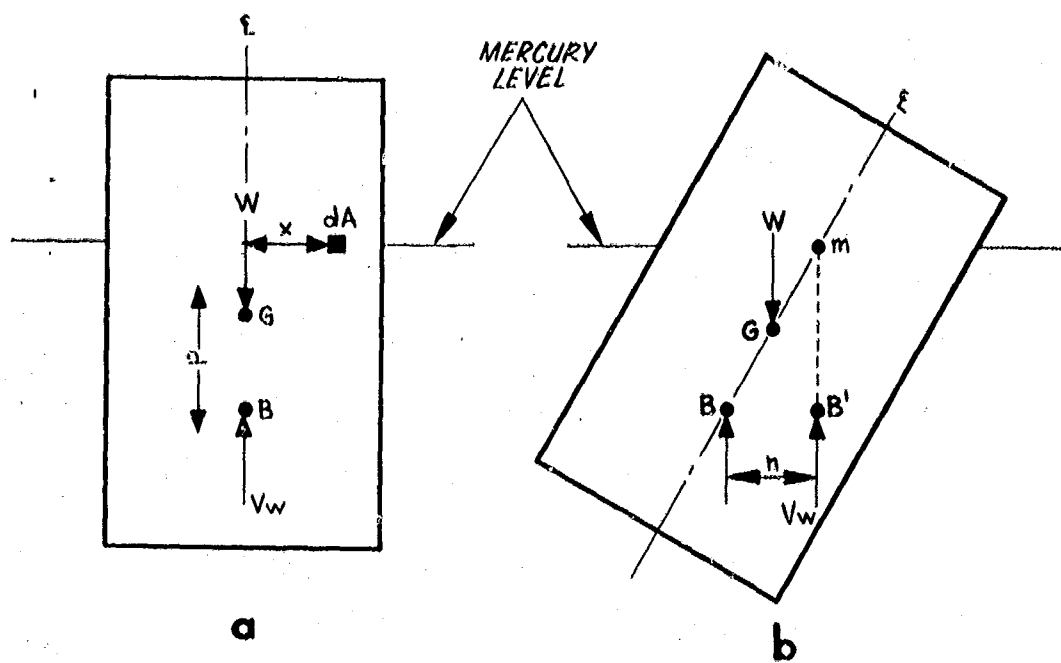
128

Fig. 53. Proposed suspension system.

as well as the horizontal (x, y) plane, the dynamic control system is greatly simplified and made unconditionally stable. Both systems are described and compared in the following discussion.

As shown in Fig. 54, the several components of thrust and torque are balanced by a combination of eight force motors; four are aligned with the vertical axis z, positioned in a plane symmetrically, and four are aligned in the horizontal plane. It will be demonstrated below that this arrangement is adequate to determine the thrust deflection and torque by algebraic manipulation of the static force motor readings.

The vertical force motors are intended only to balance torque about an axis in the horizontal plane (x, y). The main thrust (along the z-direction — vertical) is obtained from measurement of the ion engine beam current and voltage; thus z-motion is unimportant. Therefore, these four force motors are operated as series pairs such that the two always produce an equal and opposite force. This gives the required torque with no net z force.

The horizontal force motors must balance torque about the vertical (z) axis and translational thrust components in the x-y plane. Therefore, the opposite horizontal force motors cannot be paired to always produce an equal and opposite force because they must produce a net balancing force in addition to the torque.

Figure 55 shows the transducer and force motor control arrangement for the five degrees of freedom of interest. The β_x and β_y rotations are sensed by the (two-axis) bubble sensor or by four linear transducers. These signals drive the four vertical motors in matched pairs. The rotation about the vertical axis and the translation in the x-y plane cannot be sensed independently. This coupled motion is observed by four photoelectric transducers, which sense the net x-y motion of a point on the edge of the platform. Hence, the displacement which each horizontal transducer experiences is the sum of x-y center of gravity translation, plus rotation (a sin β_z).
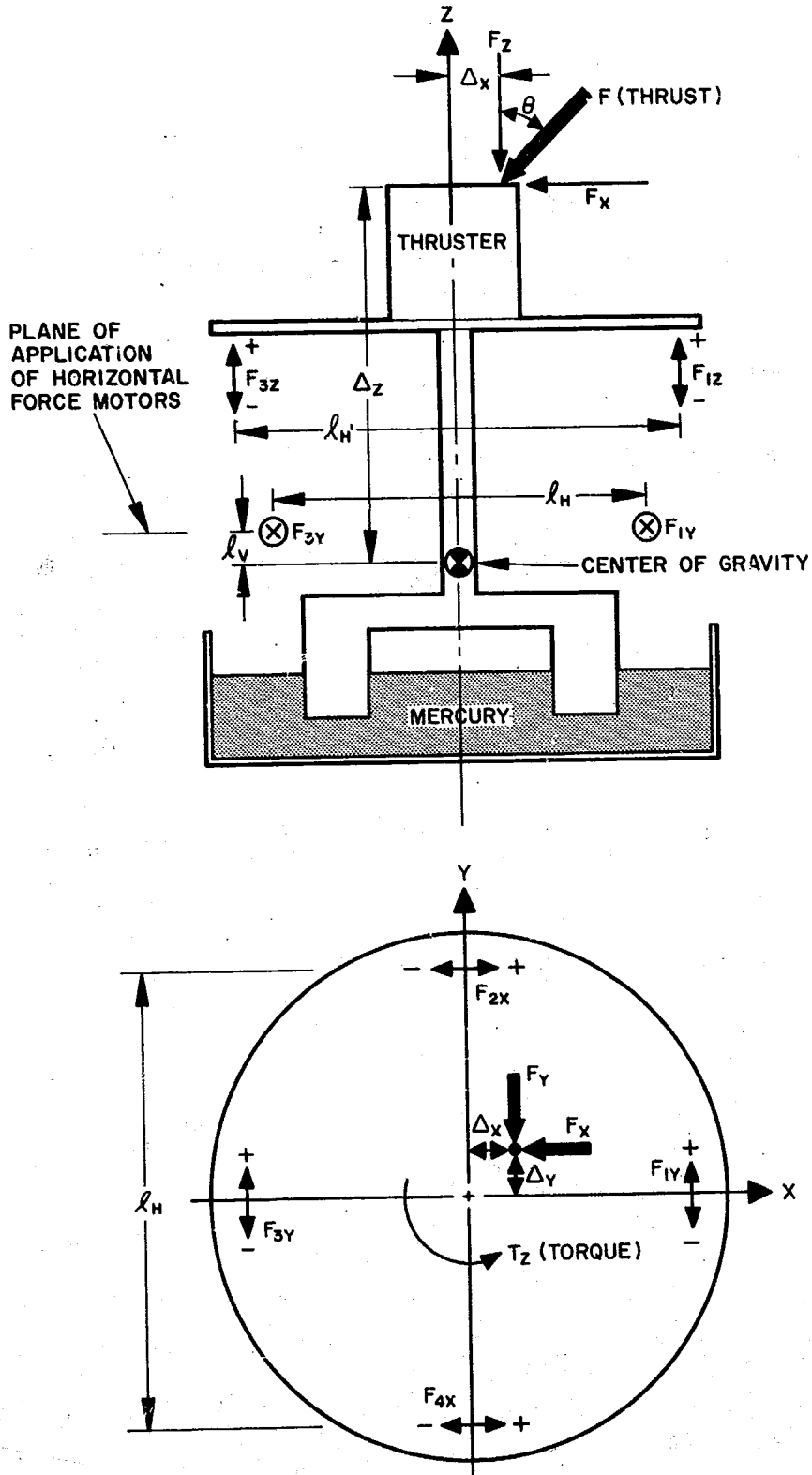
Fig. 54. Thrust stand schematic layout.
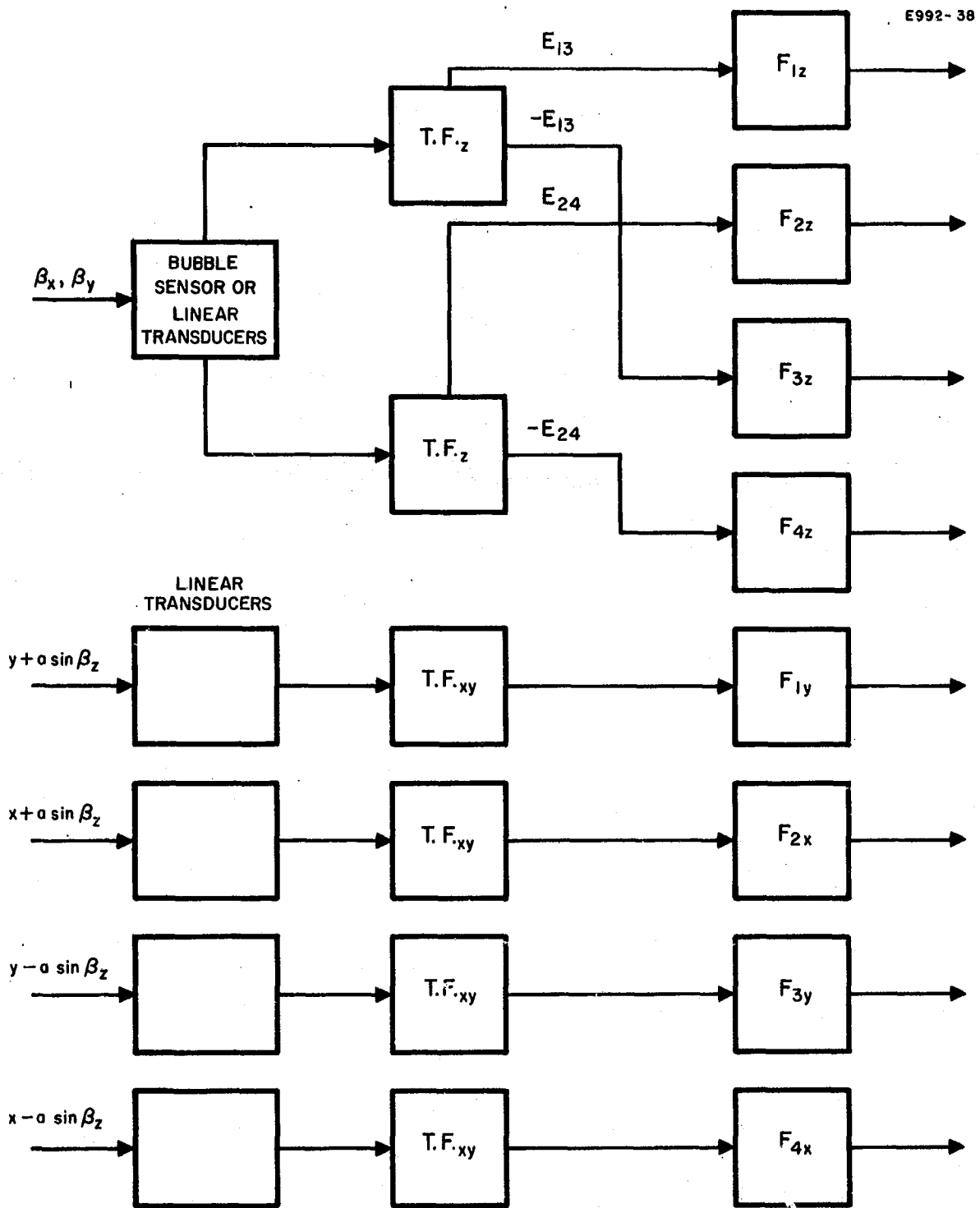
Fig. 55. Transducer-force motor arrangement.

Each of the horizontal force motors is controlled by its associated transducer, independently of the other three. The total system thus has six control loops.

a. <u>Static Analysis</u>[*] — The principle of thrust stand operation is that under steady static conditions, the static forces applied by the force motors exactly cancel out the applied constant force of the thrust vector plus an associated torque. From a knowledge of the force motor readings, the thrust vector deviation from the normal plus the torque may be determined.

The thrust vector deflection is determined by balancing the horizontal force motors. The thrust vector is represented by

$$\vec{F} = F_x \hat{i} + F_y \hat{j} + F_z \hat{k}$$

where i, j, k are unit vectors in the x, y, z directions. The angular deflection θ which we seek may be expressed as

$$\sin \theta = \frac{\sqrt{F_x^2 + F_y^2}}{F} \ . \tag{33}$$

In order that the x and y components will balance exactly,

$$F_{1y} + F_{3y} = F_y$$

and

$$F_{2x} + F_{4x} = F_x \ .$$

The amplitude of the total thrust F is measured independently from beam current and voltage. Substituting into (33),

[*] The analysis of this thrust stand was carried out by J. D. Smith, D. Berman, and S. Harrison.

$$\sin \theta = \frac{1}{F} \left[\left(F_{2x} + F_{4x} \right)^2 + \left(F_{1y} + F_{3y} \right)^2 \right]^{1/2} . \tag{34}$$

Therefore, we obtain the deflection θ from calculation involving only the basic horizontal force motors. This is true in theory; in practice, success will depend on the accuracy of the readings, and the required deflection resolution. For $1/4°$,

$$\sin \theta \approx \theta = \frac{1}{4} \left(\frac{\pi}{180} \right) \approx 0.004 \text{ rad.}$$

Assuming no torque about z and equal x-y components ($F_{2x} = F_{4x} = F_{1y} = F_{2y} = F_{xy}$), the force measuring accuracy required to measure this deflection, for a nominal thrust of 0.025 lb, is

$$\theta F = \sqrt{\left(2F_{xy} \right)^2 + \left(2F_{xy} \right)^2} = 2\sqrt{2} \, F_{xy}$$

Evaluating,

$$F_{xy} = \frac{(0.004)(0.025)}{2\sqrt{2}} = 0.35 \times 10^{-4} = 35 \, \mu \text{ lb.}$$

The applied engine torque is obtained by balancing the total applied and induced torques against the combined torsional reaction of the force motor array. The induced torque is $\vec{F} \times \vec{R}$, where $\vec{R} = \Delta x \hat{i} + \Delta y \hat{j} + \Delta z \hat{k}$ = the vector distance between the point of thrust application, and the total system center of mass. The induced torque components about the x, y, and z axis are, respectively, ($\Delta z F_y - \Delta y F_z$), ($\Delta x F_z - \Delta z F_x$), and ($\Delta y F_x - \Delta x F_y$).

The torque balances about each of the three axes are

$$(F_{1z} - F_{3z})\ell_{H'} - (F_{2x} + F_{4x})\ell_v = \Delta z F_y - \Delta y F_y \tag{35}$$

$$(F_{2z} - F_{4z})\ell_{H'} - (F_{1y} + F_{3y})\ell_v = \Delta x F_z - \Delta z F_x \tag{36}$$

$$-(F_{1y} - F_{3y})\ell_H + (F_{2x} - F_{4x})\ell_H = \Delta y F_x - \Delta x F_y - T_z \qquad (37)$$

where T_z is the engine applied torque, and ℓ is the lever arm of the force motors about the system center of gravity (Fig. 56).

Equation (37), balance of torques about the z-axis, yields the applied torque T_z, provided we know Δx and Δy, the lateral displacement of the applied force. These are available from (35) and (36). The distance Δz is not unknown, since it represents the distance between the accelerator electrode of the thruster and the system center of gravity. Hence

$$T_z = \left[\left(F_{1y} - F_{3y}\right) + \left(F_{2x} - F_{4x}\right)\right]\ell_H + \left(\Delta x F_y - \Delta y F_x\right) .$$

The accuracy required for torque measurement is 5×10^{-4} in.-lb. Neglecting the thrust vector coupling, the last term disappears, and $F_{1y} = F_{2x}$, etc. Thus,

$$T_z = 4F_{xy}\,\ell_H .$$

From Fig. 56, the lever arm length $\ell_{xy} \approx 8$ in. Evaluating,

$$F_{xy} = \frac{5 \times 10^{-4}}{4 \times 8} = 1.5 \times 10^{-5} = 15\ \mu\text{lb}.$$

Thus, the applied torque measurement accuracy requirement is slightly more severe than that of the thrust vector deflection measurement.

State-of-the-art thrust measurements down to 10 μlb have been demonstrated in a one-axis thrust platform developed by HRL for the U Air Force.[*] However the six degree of freedom platform presents new problems with transducer characteristics, mechanical balancing, and dynamic stability. The dynamics are discussed below.

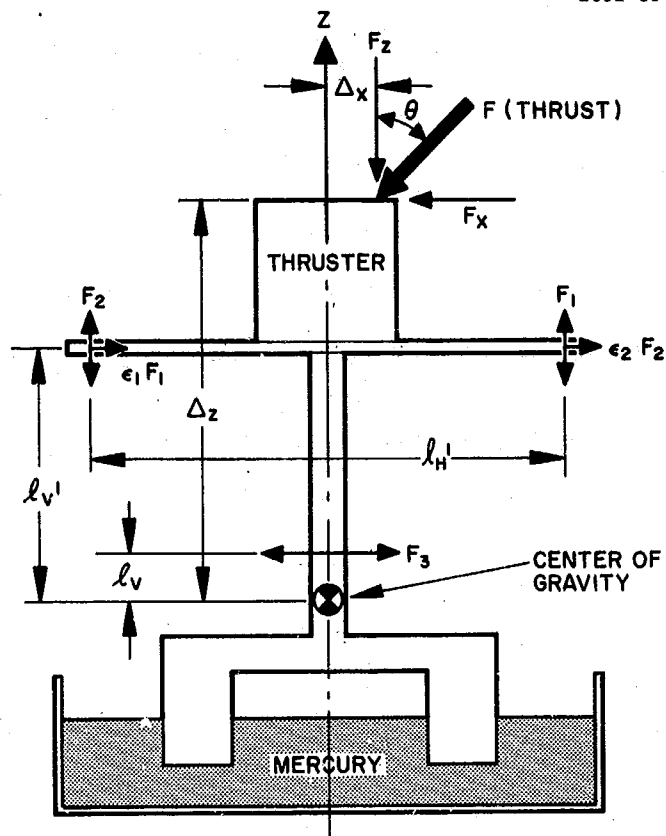[*]Contract AF 04(611)-10536.

Fig. 56. Forces applied to thrust stand.

b.   Dynamic Model — In order to study the thrust platform dynamics, the motion was limited to two degrees of freedom: one translational (x) and one rotational (β). The rotational motion is about an axis perpendicular to the translation axis, making the problem essentially two-dimensional.
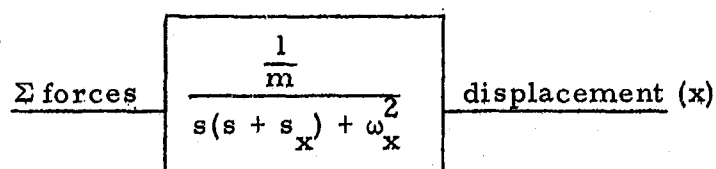
These two components of motion are sufficient to demonstrate the different transducer loop dynamics and the coupling effects between the various degrees of motion. Thus, this limited model can provide adequate insight into the dynamic characteristics of the platform, although it should be kept in mind that the real problem has thrice the complexity represented here.

Figure 57 shows the schematic for the dynamic model.

Three force motors balance the applied force components F_x, F_z. The two force motors F_1, F_2 provide a restoring torque to balance the applied torque $\Delta x F_z + \Delta z F_x + (\ell_3 F_3)$, where Δx, Δz are the applied force coordinates with respect to the system center of mass. The force motor F_3 balances the horizontal applied force component which we wish to measure.

Because we wish to study the platform dynamics, we must now consider other forces which were not important in the static case. These are displacement and damping forces which exist when the system is not in a null condition. These additional forces consist of viscous damping in the mercury liquid, spring displacement and damping forces from the electrical leads, and buoyancy torques due to displacement of the float metacenter. Thus, each degree of motion is described by a damped spring-mass system, although some of the spring and damping forces may be very small.

In block diagram notation

$$\Sigma\text{ forces} \longrightarrow \boxed{\dfrac{\dfrac{1}{m}}{s(s + s_x) + \omega_x^2}} \longrightarrow \text{displacement (x)}$$

137

Fig. 57. Block diagram schematic for the two-dimensional dynamic model.

E992-40

138

$$\Sigma \text{ torques} \quad \boxed{\dfrac{\dfrac{1}{I}}{s(s + s_\beta) + \omega_\beta^2}} \quad \text{rotation } (\beta)$$
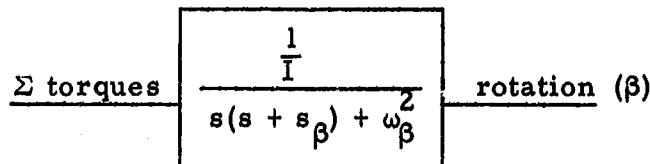
where.

$m \equiv$ system mass

$I \equiv$ system moment of inertia about horizontal axis

$\omega_x \equiv$ natural frequency, x-motion

$\tau_x = 1/s_x \equiv$ time constant, x-motion

$\omega_\beta \equiv$ natural frequency, β-motion

$\tau_\beta = 1/s_\beta \equiv$ time constant, β-motion.

To complete the model, we also include the coupling forces which can cause one degree of motion to affect another degree. This coupling is of two types:

   1.   physical coupling

   2.   induced coupling.

The first of these can be visualized by considering the translational displacement of a body attached to a spring not at the center of mass. The displacement thus causes a reactive torque, in addition to the translational restoring force. The second type of coupling is that induced by the force motors. For example, when the x-translational force motor acts it will induce a torque.

The coupling transfer function may be written

$$F_i \quad \boxed{a}$$
$$x, \beta \quad \boxed{C_0 + C_1 s} \quad \otimes \longrightarrow \text{Force or Torque}$$
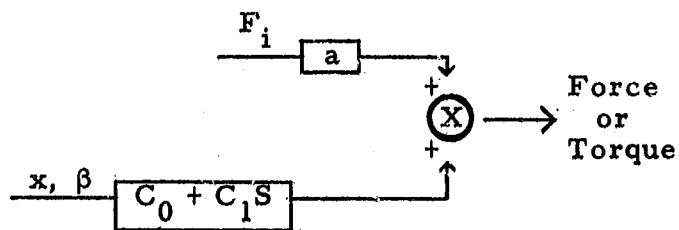
c.   Control System Analysis and Design — The engine
thrust measuring instrument is a precision balance of six components of
force and torque.   Before engine thrust is measured the system must be
balanced by adjusting the engine and counterweights to reduce the effects
of environmental vibrations which might result from vacuum pumps,
seismic disturbances, etc.   When the balance adjustments have been
made and the mechanical zero established, the mechanical system is then
calibrated with the electrical instrumentation and control system.

The following physical equations describe a single degree of
translational dynamics of the six-degree thrust platform during an
engine thrusting condition.   These equations are based on the assump-
tion that the platform has been previously balanced in an engine non-
thrust condition such that platform disturbance from background vibra-
tion is completely balanced out.

$$(F_E - F_R) = M\ddot{x} + B\dot{x} + Kx$$

where

F_E ≡ engine thrust force (lb) or torque

F_R ≡ platform restoring force (lb) or torque

M ≡ total mass of system (lb-sec^2/in.) or moment
of inertia

B ≡ velocity damping (lb-sec/in.)

K ≡ spring rate (lb/in.)

$\ddot{x}$ ≡ horizontal acceleration

$\dot{x}$ ≡ horizontal velocity

x ≡ horizontal displacement

Linearizing and performing a LaPlace-transform on the force balance
equation yields the linear operator expression

$$\frac{\Delta x(S)}{\Delta F(S)} = \frac{1}{(MS^2 + BS + K)} \quad .$$

140

The thrust platform is designed to have a minimum mechanical spring rate K in the direction of thrust measurement. However, all residual spring forces cannot be completely eliminated. As the value of mechanical spring rate K approaches zero, the transfer function of the mechanical device approaches the following

$$\frac{\Delta x(S)}{\Delta F(S)} \approx \frac{1/B}{S(\tau_1 S + 1)}$$

where

$$\tau_1 = M/B \text{ (sec)}.$$

It is clearly shown here that as the mechanical spring rate (resulting from wire, cable, buoyance effect, etc.) approaches zero, the device assumes the characteristics of a mechanical integrator with a cascaded first order lag with a time constant τ_1 (sec).

In order to achieve moderate speed operation the platform mechanism control loop is closed to meet the following requirements:

1. The goal of the dynamic response of the control system with a 20 lb engine weight load on the platform will be approximately 1 cps at all force ranges.

2. The goal threshold of the thrust stand is less than 3.0 μlb of thrust.

3. The goal steady state error of the thrust stand is less than 3% of the upper limit of the 100 μlb range setting.

4. The system is optimally damped for all ranges of thrust and weight loads and stable with a 20 lb engine weight load at all force ranges.

Since the thrust platform is basically an integrator device, the platform will continue to displace as long as a force imbalance exists across the platform within the mechanical limits of the mechanism. To provide a restoring force feedback F_R to servo set the platform

to its steady state null position during engine thrusting, it is necessary to provide a voltage integrator to generate a restoring voltage E_R to the restoring motor that is a function of the time integral of the displacement away from the null position. Displacement of the platform Δx causes an error voltage ΔE_x to be generated in the transducer output. This error voltage is integrated to contribute to the restoring voltage E_R to the force motor. When the horizontal forces across the platform are balanced, the platform is restored to the null position. The addition of a voltage or mechanical integrator (i. e. , a bubble sensor) into the control loop results in additional control loop phase shift and system instability. Therefore, in order to provide a response with a high degree of stability for this type of system, it becomes necessary to introduce a proportional plus derivative compensating network in parallel with the voltage integrator and in tandem with the mechanical integrator.

Horizontal loop — Consider now the transfer function block diagram of the horizontal force balance control loop (Fig. 58). The open loop transfer function for the linear system is

$$GH(S) = \frac{K_o (S^2 + a_1 S + a_2)}{S\left[S^2 + (B/M)S + K/M\right]}$$

where

$$K_o = \left(\frac{P}{M}\right)\left(\frac{\delta E_x}{\delta x}\right)K_D \text{ rad/sec}$$

$$a_1 = K_P/K_D \text{ (rad/sec)}$$

$$a_2 = K_I/K_D \text{ (rad/sec)}^2$$

$$P = K_A K_M \text{ (lb/V)}$$
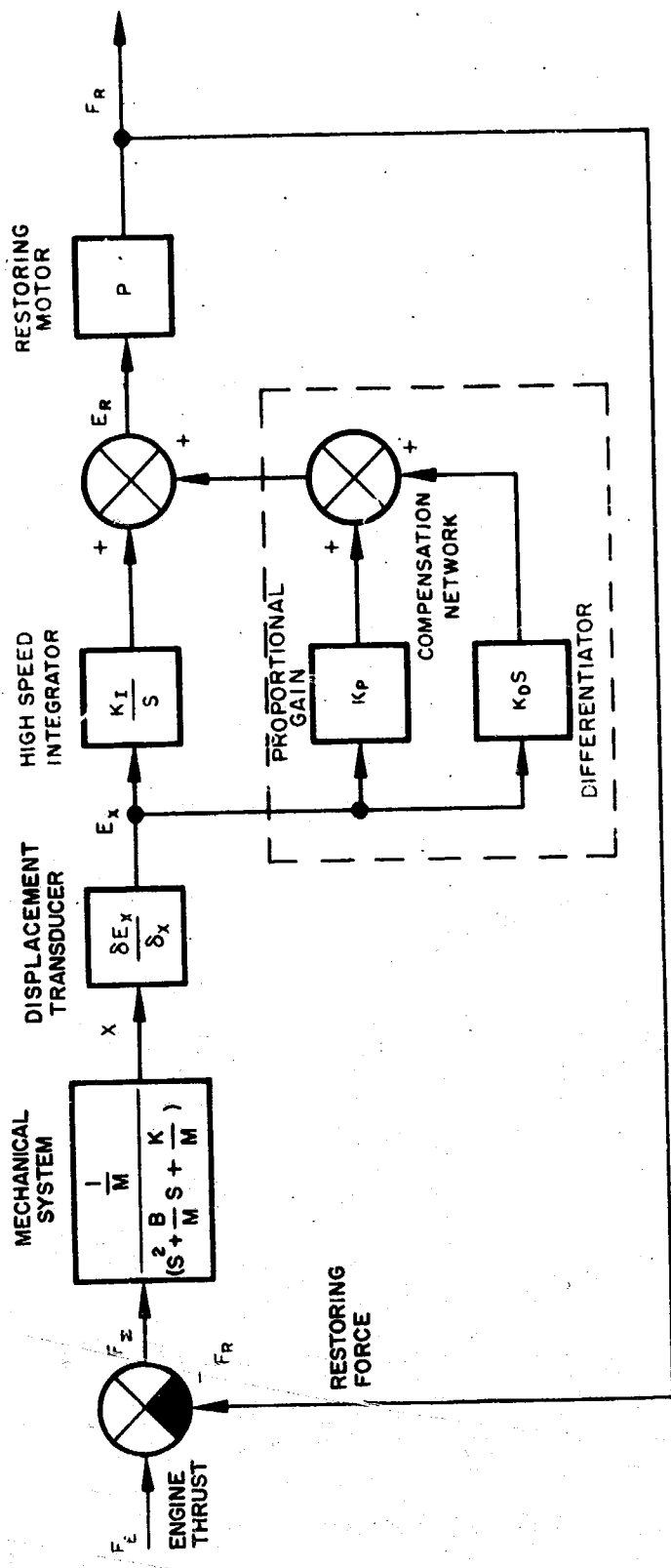
$$K_P \equiv \text{ proportional gain (volts/volts)}$$

142

Fig. 58. Horizontal force balance control loop system block diagram.

143

$$K_D \equiv \text{derivative gain (volt-sec/volt)}$$

$$K_I \equiv \text{integral gain (volt/sec-volt)}$$

$$P \equiv \text{force motor power gain (lb/volt)}$$

$$\frac{\delta E_x}{\delta_x} \equiv \text{displacement transducer gain (V/in.)} .$$

If the network gains can be assumed to be adjustable, then a_2 can be set approximately to equal (K/M) and a_1 can be adjusted to approach (B/M) experimentally (e. g., the network gains[*] can be set to the following analytically determined values).

$$a_1 = K_P/K_D = B/M \approx 5.0 \text{ (rad/sec)}$$

$$a_2 = K_I/K_D = K_x/M \approx 1.0 \text{ (rad/sec)}^2$$

If $K_D = 1.0$ sec/rad, then $K_I = 1.0$ rad/sec and $K_P = 5.0$. The roots of the polynomial are thus

$$S^2 + (B/M)S + K/M = S^2 + (K_P/K_D)S + \frac{K_I}{K_D} = 0$$

$$\sigma = -\frac{a_1}{2} \pm \frac{1}{2}\sqrt{a_1^2 - 4}$$

$$= -2.5 \pm \frac{1}{2}\sqrt{25 - 4}$$

$$\sigma_1 = -0.2, \quad \sigma_2 = -4.8$$

---

[*]Gains less than unity (1) imply passive networks.

144

The open loop transfer function is thus

$$\frac{F_R(S)}{F_\Sigma} = \frac{K_o (S + \sigma_1)(S + \sigma_2)}{S(S^2 + (B/M)S + K/M)}$$

where $F_\Sigma = F_E - F_R \equiv$ error signal, shown in Fig. 59. Because the roots of the network are adjusted to equal the roots of the mechanical system, the open loop transfer function is reduced to

$$\frac{F_R}{F_\Sigma}(S) = \frac{K_o}{S} .$$

The closed loop transfer function now becomes

$$\frac{F_R}{F_E}(S) = \frac{K_o}{S + K_o} = \frac{1}{\tau S + 1}$$

The over-all loop response acts as a first order lag with a time constant (τ) equal to $1/K_o$, i. e.,

$$\tau = \frac{1}{K_o} = \left(\frac{M}{P}\right) \frac{1}{K_D\left(\frac{\delta E_x}{\delta_x}\right)} \text{(sec)} .$$

Here

$$M = 0.065 \text{ lb sec}^2/\text{in.}$$

$$K_D = 1.0 \text{ sec/rad}$$

$$\left(\frac{\delta E_x}{\delta_x}\right) \approx 10^4 \text{ V/in.}$$

$$P = 10^{-5} \text{ lb/V.}$$

$$G(S)H(S) = \frac{Ki(S+0.02)(S+50)}{S(S+0.2)(S+4.8)}$$

E992-41

$\delta = 0.7$
$\omega = 65\,\text{rad/sec}$
$K_O = 85$

$\delta = 0.8$
$K_O = 113$

$\delta = 0.9$
$K_O = 154$

ω_n

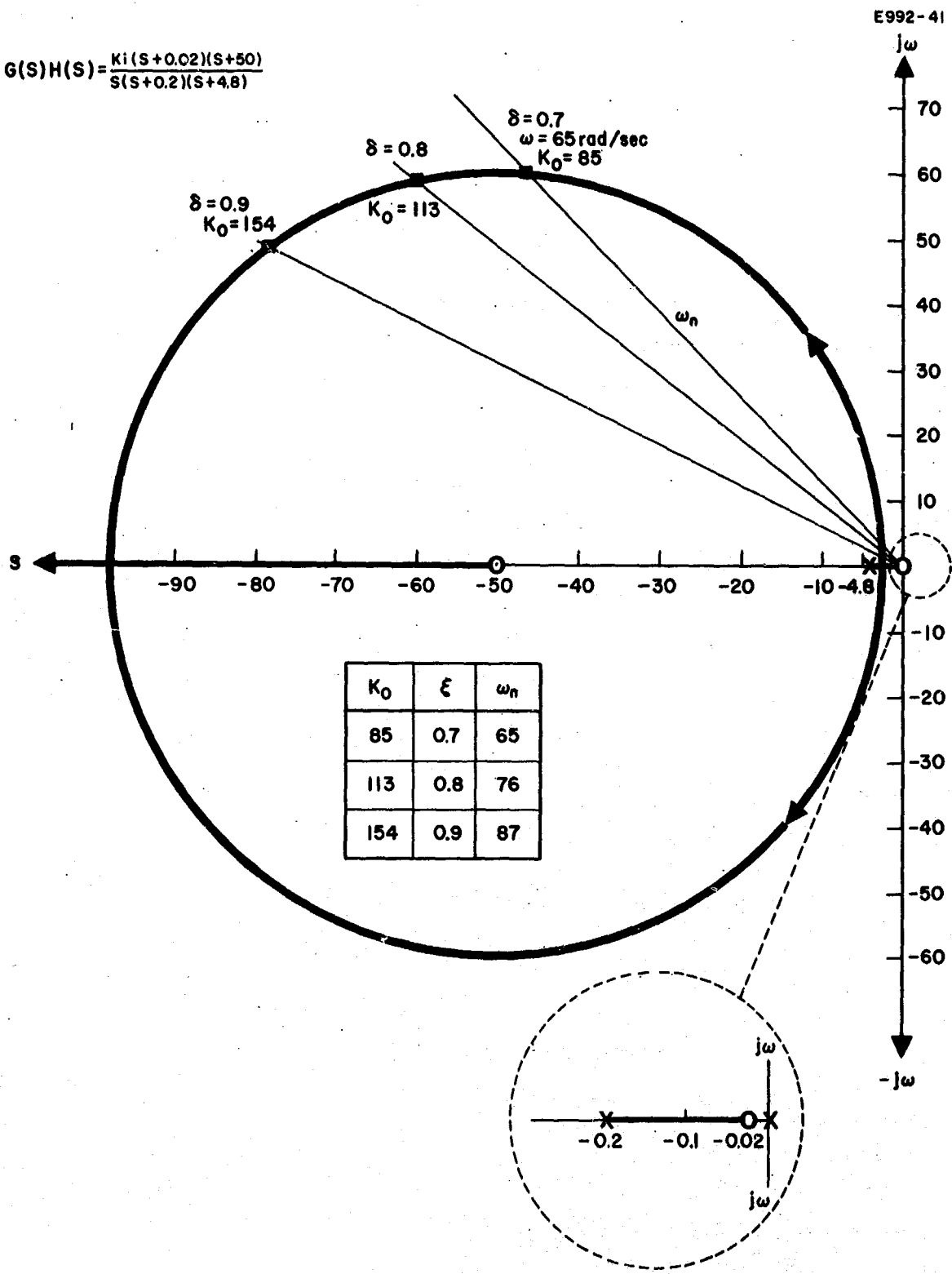| K_O	ξ	ω_n
85	0.7	65
113	0.8	76
154	0.9	87

Fig. 59. Root locus plot of horizontal platform control open loop transfer function.

146

Therefore,

$$\tau \approx 0.65 \text{ sec.}$$

Improved frequency response can be obtained by increasing the proportional network gain K_P. For example, let $K_P = 50$; the network roots are then

$$\sigma = \frac{-50}{2} \pm \frac{1}{2} \sqrt{2500 - 4}$$

$$\sigma = -25 \pm \frac{1}{2} \sqrt{2496}$$

$$\sigma_1 \approx 0.02; \quad \sigma_2 \approx 50$$

The open loop transfer function now becomes

$$\frac{F_R}{F_\Sigma} (S) = \frac{K_o (S + 0.02)(S + 50)}{S(S + 4.8)(S + 0.2)} \quad .$$

A plot of the root locus of the open loop transfer function is shown in Fig. 59. The percent overshoot when the system is subjected to a step input can be estimated easily by referring to Fig. 60. For a damping factor $\xi = 0.7$ the overshoot is near zero. For higher values of damping factor it is noted that the system is heavily damped. For lower values of damping, the system is underdamped. For operation at a damping factor of 0.7, the over-all system natural frequency (ω_n) is approximately 65 rad/sec or 10 cps, as shown in Fig. 60. This estimate will be verified in subsequent analog solutions.

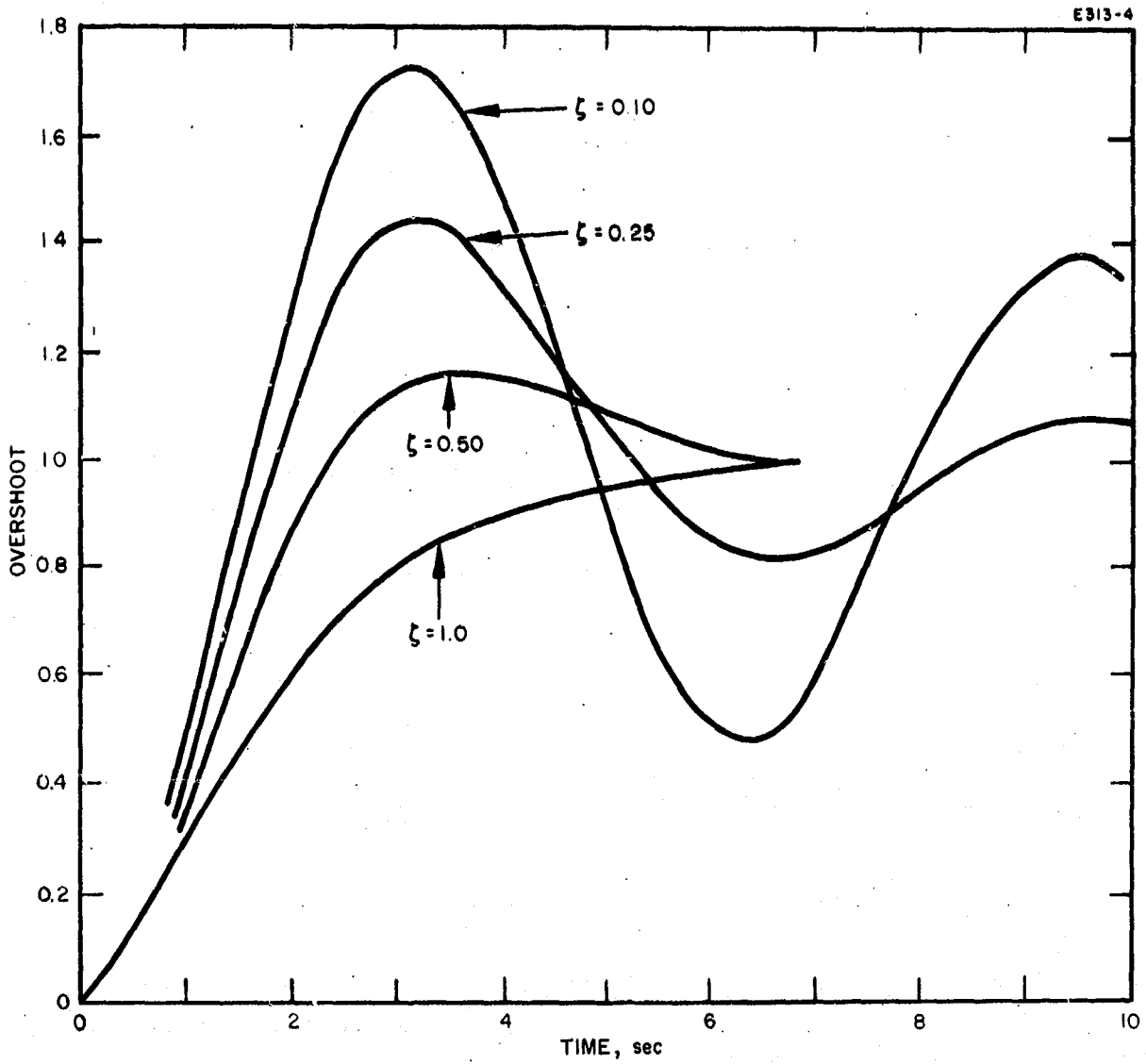$$\omega_n = 65 \text{ rad/sec} \approx 10 \text{ cps}$$

$$\xi = 0.7$$

147

Fig. 60. Unit step-function response for system with transfer function $\omega_s^2/(s^2 + 2\zeta\omega_n s + \omega_n^2)$.

The closed loop function of the horizontal force balance system is

$$\frac{F_R}{F_E}(S) = \frac{G}{1 + GH}(S)$$

where $H = 1$.

The frequency response characteristic shows that the theoretical system bandwidth is approximately 20 cps for a system gain of $K_o = 85$ rad/sec. The system equations indicate that the bandwidth of the horizontal force system can be extended by increasing the system gain K. Thus, the power gain of the control loop and the mass of the system will determine the system bandwidth; for a 10 cps system natural frequency with a 20 lb load on the thrust stand, the open loop gain of the system should be at least

$$K_o = \frac{P}{M}\left(\frac{\delta E_x}{\delta x}\right)K_D = 85 \text{ rad/sec}.$$

Rotational Deflection Control Loop — Consider now the transfer function block diagram of the rotational force balance control loop shown in Fig. 61. The basic components of the system are the mechanical system, bubble sensor, compensating network, and power amplifier and electromagnetic force motor.

In theory, any static moment resulting from an off-axis engine thrust component will be counterbalanced by an equal and opposite torque from the force motor, provided that the control loop is properly designed. The design of a compensating network for the rotational control loop is somewhat more critical, however, if a bubble level sensor is used, because of the dynamic characteristics of this component.

Consider the basic system problem. The Laplace transfer function of the mechanical system in the rotational axis, neglecting for the moment the cross coupling effects, may be described as
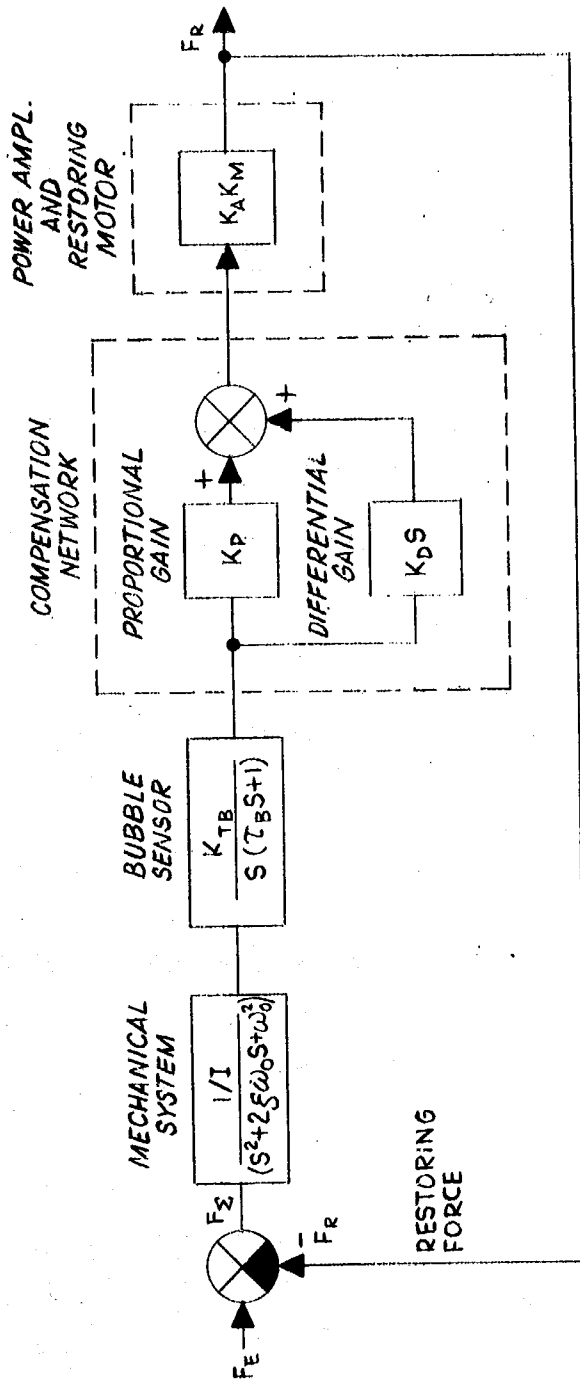
149

Fig. 61. Rotational force balance control loop system block diagram.

$$\frac{\Delta\theta}{\Delta F_E}(S) = \frac{1/I}{(S^2 + 2\xi\omega_\beta S + \omega_\beta^2)} \tag{38}$$

where

$$\omega_\beta = f(I, K_{eff}) .$$

As the effective spring rate K_{eff} approaches a small value, as in the case of a neutrally balanced system with negligible spring rate coupling of the electrical cabling, the platform system dynamics approach the characteristics of a mechanical integrator for small force perturbations; e.g., as $\omega_\beta \to$ small value,

$$\frac{\Delta\theta}{\Delta F_E}(S) = \frac{1/I}{S(S + 2\xi\omega)} . \tag{39}$$

The bubble sensor also has the characteristics of a mechanical integrator, i.e.,

$$\frac{\Delta E}{\Delta\theta}(S) = \frac{K_{TB}}{S(S + S_{TB})} . \tag{40}$$

The cascading of the two devices now presents a relatively severe stability problem, as shown below.

$$\frac{\Delta E}{\Delta F_E}(S) = \frac{K_{TB}/I}{S^2(S + 2\xi\omega_\beta)(S + S_{TB})} . \tag{41}$$

The double integration term (S^2) results in 180° phase shift of the input signal. The compensation network therefore must correct the total system phase shift to less than 180° if over-all loop stability is to be achieved.

The first step in considering the compensating network is to consider a single first order lead network coupled to the output of the

bubble sensor output. This network would be comprised of a proportional plus derivative network:

$$\frac{\Delta\theta^1}{\Delta\theta} = K_P + K_D S = K_p (\tau_c S + 1) .\qquad (42)$$

The effects of compensating for this phase shift with single or multiple lead networks were considered in detail both analytically and by analog simulation in the second quarterly report of Phase I of this contract, to which the reader is referred for details. The final conclusion drawn is that it is possible to stabilize such a system. It was also concluded, however, that a much simpler and equally sensitive system could be constructed by using linear displacement sensors placed at the periphery of the floating mass to achieve the same result. The final design is based on this latter concept; the dynamic analysis is then similar to that for the horizontal loop.

The cross coupling effects between loops were briefly studied on the analog computer. The result was that if each loop was independently stabilized the coupling introduces no new instability.

The basic conclusions to be drawn from the study are that

a.   the bubble sensor may be replaced with linear transducers and that an over-all simplification of the system will result

b.   the linear transducers should be designed to provide maximum possible sensitivity (10^5 V/in., if possible)

c.   the floating mass should be as light as possible; this suggests exchanging the position of the forcemotor magnets (now mounted on the float) and the coils if suitably flexible leads can be demonstrated.

5.   Development of Thrust Stand Hardware

A layout of the system is shown in Fig. 62. The various components may be readily identified by referring to the schematic
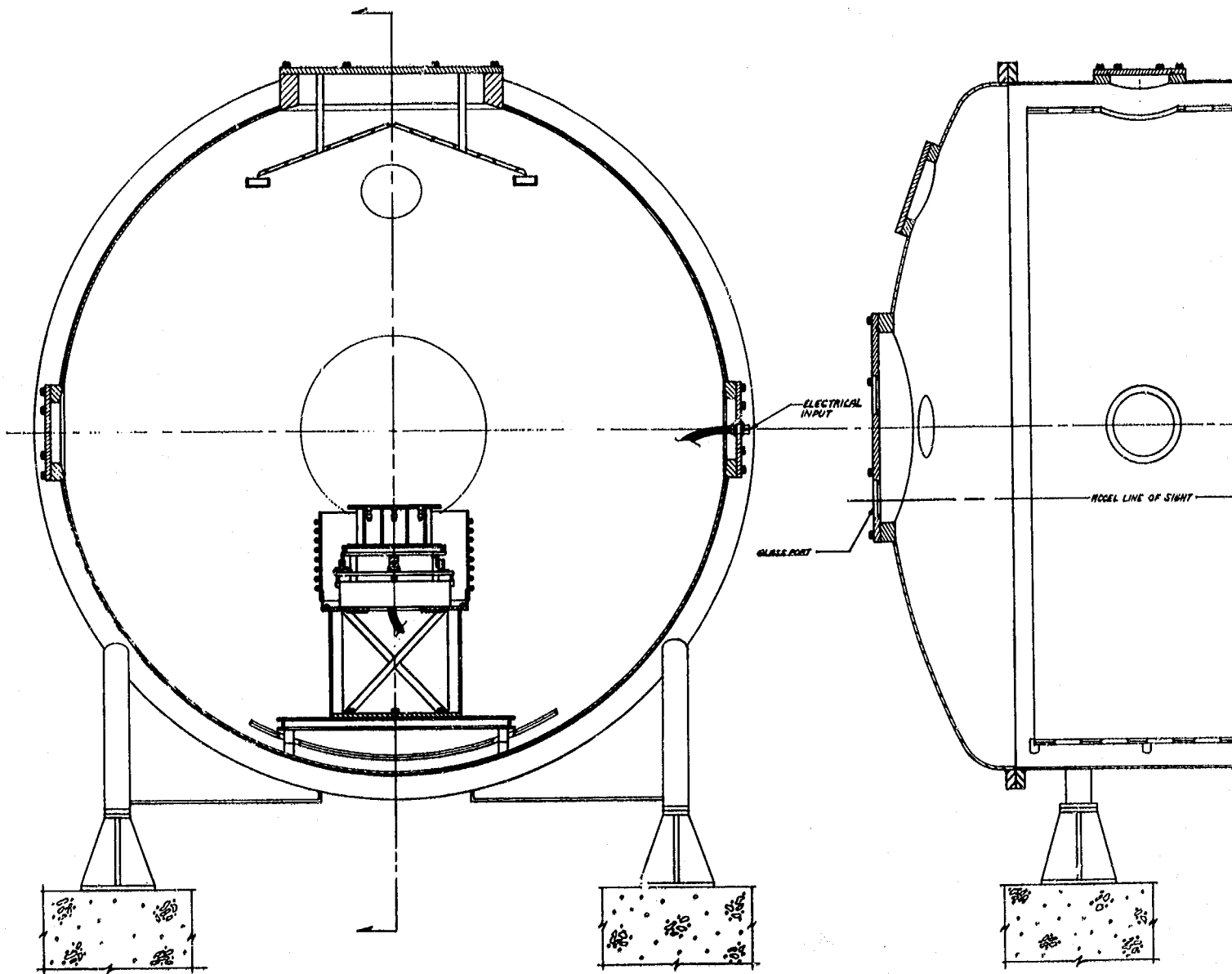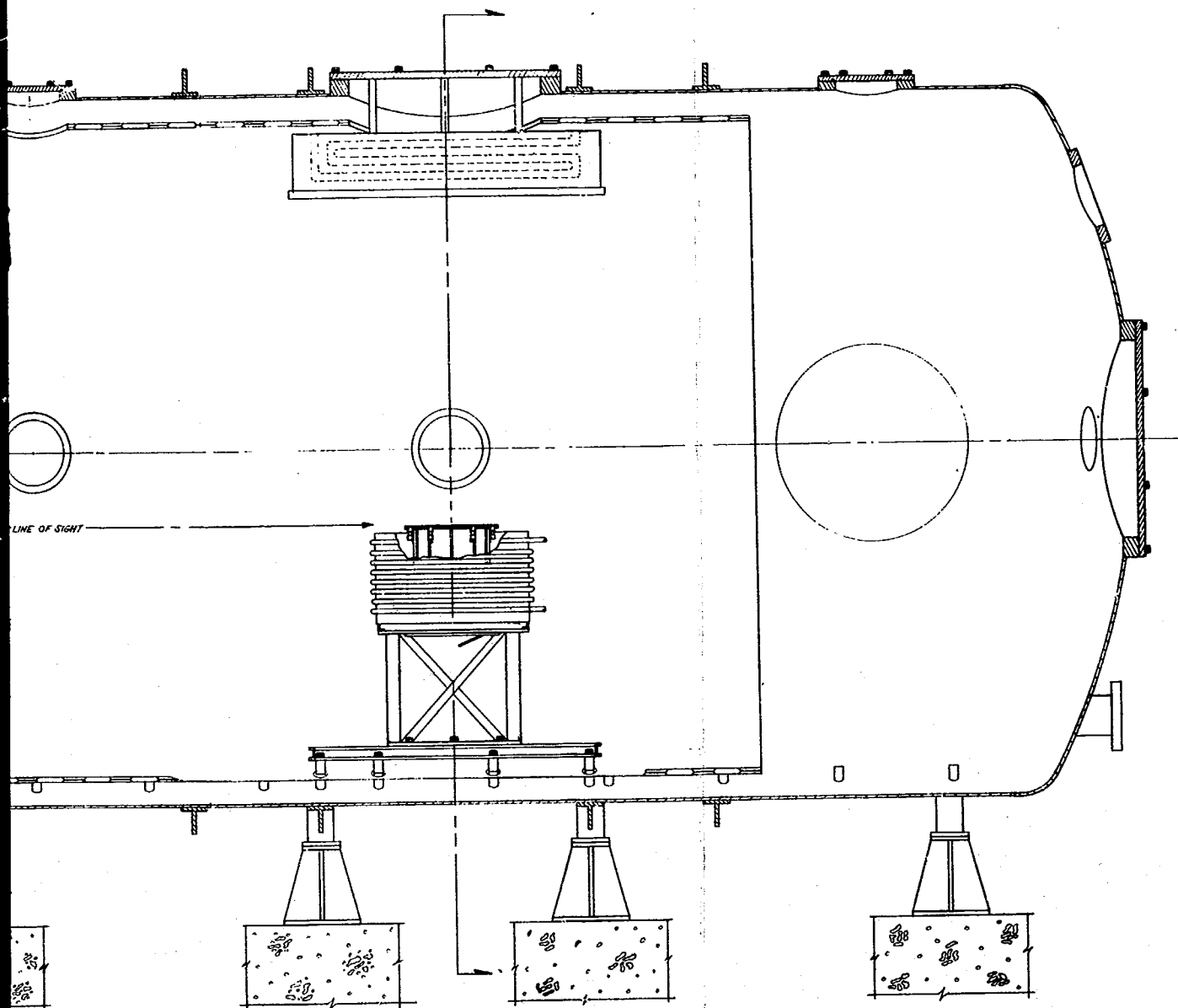
ELECTRICAL
INPUT

ACCEL LINE OF SIGHT

GLASS PORT

Fig. 62.   Cross sectional layout of thrust stand a

LINE OF SIGHT

st stand and thruster in 9 ft diameter chamber.

sketch of the system in Fig. 54. At the end of Phase I the main components (pan, float, table, etc.) were fabricated and assembled. The floatation principle and neutral bouyancy condition were demonstrated. The other components necessary for the system are discussed individually below.

a. Displacement Sensors — A displacement sensor which utilizes a light beam and a pair of matched photocells has been developed (see Fig. 63); the light falling onto the cell is apertured by a slit mounted on the floating table. The relative motion between the slit and the light bulb and sensors which are mounted on the fixed table causes a variation in the amount of light reaching each half of the split photocell. This produces a difference in voltage across the matched load resistors which may be interpreted directly in terms of the relative motion.

A system of this type using a United Detector Technology photodetector and gallium arsenide light source has been designed, fabricated, and tested. As shown in Fig. 64, this model, actuated by a micrometer drive, has demonstrated resolution of linear motion of less than 0.0001 in. and good sensitivity. This high sensitivity and the absence of any mechanical coupling between the floating and fixed suspension make this a very attractive system for this application.

b. Forcemotors — Electromechanical forcemotors such as those used to drive loudspeakers are preferred here because the force generated is directly proportional to input current and independent of position over a range which is large compared with the operating range. It is tentatively planned to mount the permanent magnet driver on the floating suspension and the voice coil on the fixed platform. This increases the weight of the floating system (in contrast to the requirements of the dynamic analysis) but reduces the spring constant associated with the number of leads crossing from the fixed to floating table. As quantitative information concerning lead stiffness becomes available, this decision will be reevaluated.

APERTURE
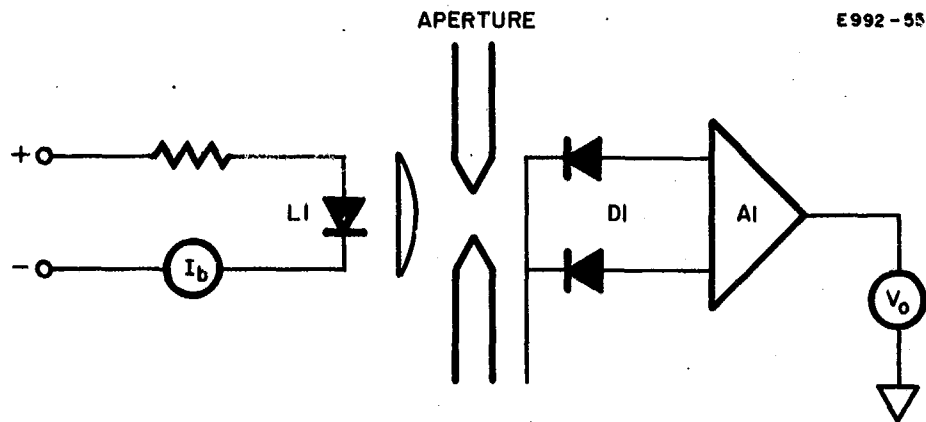
AI — BURR BROWN NO. 1506
    GAIN = 200

LI — GAS LIGHT SOURCE
    NO. 470A
    ELECTRO NUCLEAR LABS

DI — IR DETECTOR
    NO. PIN SPOT II
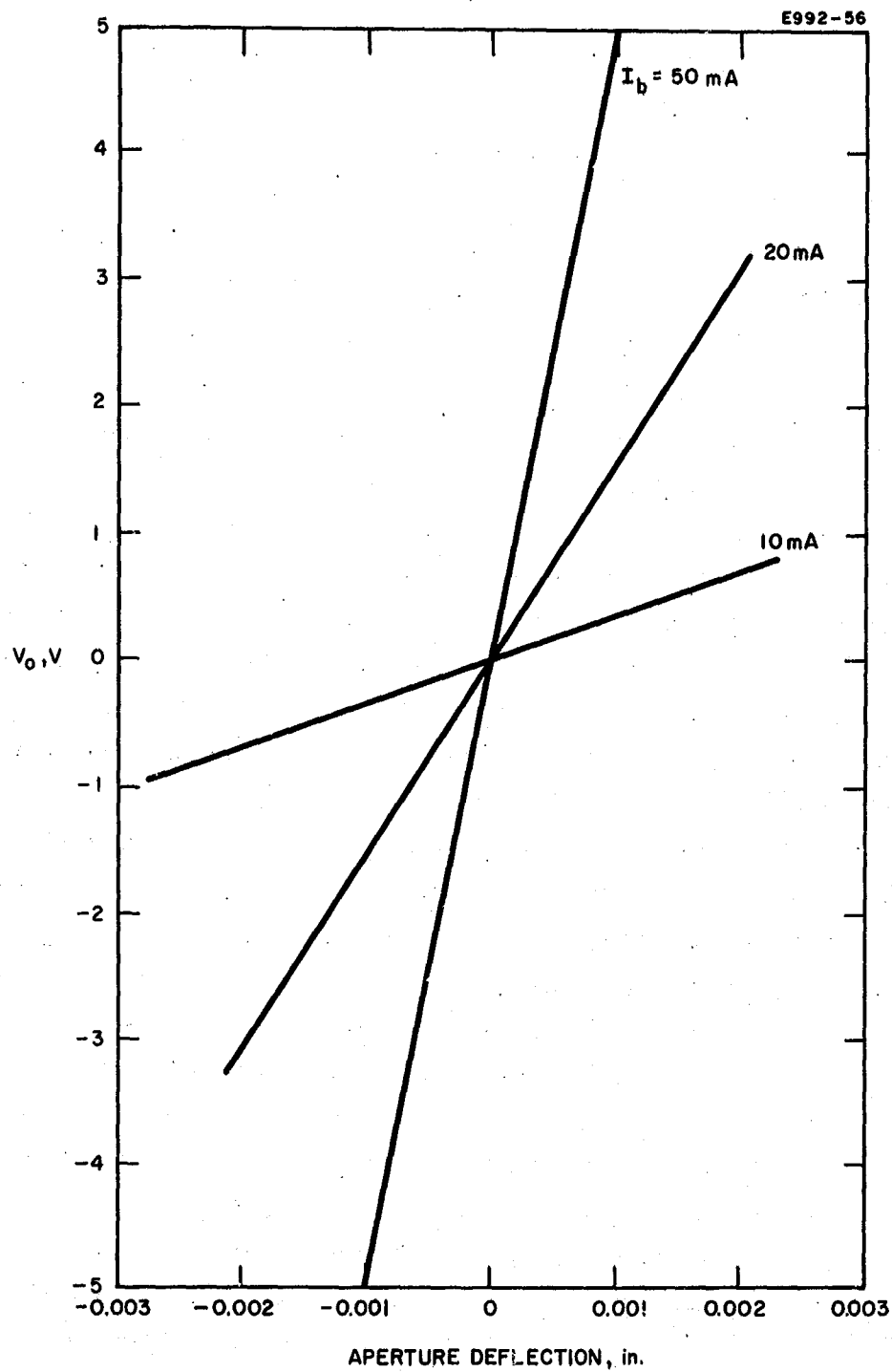   UNITED DETECTOR TECH

Fig. 63. Optical linear displacement sensor.

Fig. 64. Sensitivity of linear displacement sensor.

157

Three commercial speakers have been disassembled and the forcemotors checked. The most useful forcemotor for this task comes from an Altec speaker, which has a nominal force of 0.5 lb/A. One possible difficulty with the commercial speakers is that the voice coils are by design mounted on very lightweight and delicate structures. This may ultimately necessitate rewinding of the coils on a more rigid form to provide stable mechanical coupling to the table.

    c. <u>Electrical Leads</u> — A minimum of 16 leads will be required to operate the thruster and all the actuators necessary for the experiment. These must mechanically connect the floating system and the fixed tank. It is desirable, therefore, that they be as flexible as possible to reduce the spring constant associated with the suspension system. Several lead geometries have been proposed and samples of highly flexible leads have been obtained from an internal HAC source and from Cicoil Corp. of Chatsworth. The spring constants and other features of these leads will be evaluated before the thrust stand design is completed.

The Hughes cabling is very thin and composed of thin (0.0015 to 0.002 in. thick) conductor sandwiched between insulating films of teflon. This makes this cabling very flexible in bending through the flat plane. The conductor width is varied to increase or decrease the current carrying capability of the cables.

The Cicoil cable can be composed of different kinds of stranded fine wire conductors. These are sandwiched in silicone. The thickness varies with the conductor and ranges from 0.015 to 0.080 in. thick. A sample thirty-six conductor cable is 15/16 in. wide and relatively flexible. The over-all flexibility of this cable can be greatly increased by slitting the insulation between the conductors.

VI. CONCLUSIONS

The major conclusions resulting from this program are given briefly below.

The ion optical characteristics of an ion thruster accelerator with plasma source can be analyzed accurately by the use of an appropriate digital computer program, including the effects of motion of the plasma sheath and perturbations in trajectories resulting from electrode movement. The transverse thrust resulting from lateral electrode displacement has been found to be linear over reasonable ranges. Coefficients were determined relating the change in axial and transverse thrust to electrode perturbations. The effect of electrode tilt was found to be negligible compared with lateral displacements.

The main identifiable mode of thrust vector change was found to be due to electrode warping resulting from thermally induced stresses. This effect will alter the accel-screen spacing, thereby changing the axial thrust by as much as 18% for typical expected thermal stresses. While no torque around the roll axis of a spacecraft will be created by axisymmetric buckling of electrodes, the change in thrust of an individual thruster in an array can lead to torques around the roll and pitch axes. These torques can be eliminated by transverse displacement of the array relative to the spacecraft center of mass.

The electrode warping effect is inherent in the electron bombardment type thruster. While it is felt that dramatic improvements will not result from thruster design changes, the analysis carried out in this program has shown directions for electrode support structure development in order to reduce the warping.

Analysis of the possible causes of torque around the thrust axis of the engine (corresponding to the roll axis of the spacecraft) showed that these components cannot be predicted accurately by analysis alone. The causes would be due to electrode misalignment in assembly or due to vibration. However, this study has yielded tolerances useful in specifying assembly precision.

159

While this study has shown the difficulty of developing a general rule which accurately characterizes the expected thrust vector misalignment of an electron bombardment thruster, considerable insight into the fundamental causes of misalignment has been achieved. The development of the precision floating thrust stand will allow accurate measurement of the several components of thrust. This capability will be particularly valuable in determining the result of effects which cannot be calculated accurately: for example, the torque around the thrust axis due to assembly errors and vibration induced movement. In Phase II the thrust stand will be developed and can then be used for experimental verification of those effects determined in Phase I by analysis as well as those difficult to calculate effects just mentioned. This experimental facility will offer a means by which an effective program of development of new techniques of thruster design and construction can be carried out (e. g., on new electrode support techniques) so as to reduce the misalignment problems in the thruster.

VII.   NEW TECHNOLOGY

The following items of new technology were conceived and developed to varying degrees in the course of this program.

1.   Stiff column system
2.   Floating suspension system
3.   Light beam motion indicator
4.   Overriding cam mechanism for electrode motion.

REFERENCES

1. W. S. Seitz and S. Eilenberg, J. Appl. Phys. 38, 276 (1967).

2. C. Fay, A. L. Samuel, and W. Shockley, Bell System Tech. Rev. 17, 19 (1938).

3. K. Amboss, IEEE Trans. ED-12, 313 (1965).

4. W. C. Lathem, J. Spacecraft Rockets 5, 735-737 (1968).

5. W. J. O'Donnell and B. F. Langer, ASMEJ. Vol. 308 (1962).

6. E. A. Richley and W. R. Kearslake, AIAA Paper No. 68-542, 1968.

APPENDIX I — DETERMINATION OF GEOMETRIC (VIEW) FACTORS

A.   **Definition of Geometric (View) Factors for Radiative Heat Transfer**
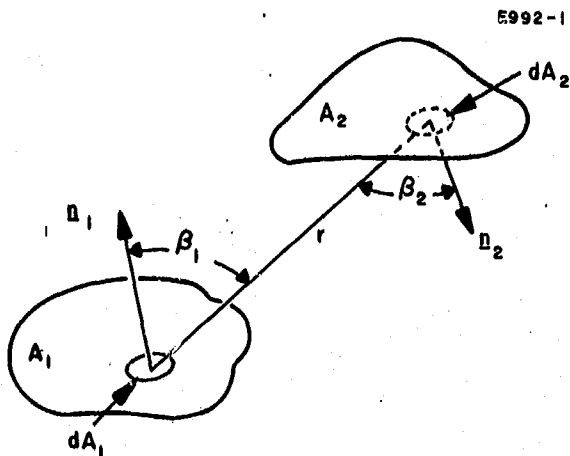
The definition of the geometric (view) factor $F_{A_1 - A_2}$ which enters into the calculation of the radiant heat transfer between two finite surfaces A_1, A_2 follows from the assumptions that:

1.   The intensity of heat radiated from an infinitesimal area element dA_1 is proportional to dA_1 and varies with direction as the cosine of the angle from the normal $\underline{n}_1$ to dA_1.

2.   The quantity of heat incident on an element dA_2 from dA_1 is proportional to the solid angle $d\omega = dA_2 \cos\beta_2 / r^2$ subtended by dA_2 as seen from dA_1.

The ratio

$$\frac{\int_{A_1} \int_{A_2} \dfrac{\cos\beta_1 \cos\beta_2}{r^2} dA_1 dA_2}{\int_{A_1} \int_{2\pi} \cos\beta_1 \, dA_1 \, d\omega} = \frac{1}{A_1} \int_{A_1} \int_{A_2} \frac{\cos\beta_1 \cos\beta_2}{\pi r^2} dA_1 dA_2$$

$$\equiv F_{A_1 - A_2} \, ,$$

165

of the heat radiated by area A_1 which is incident on area A_2 to the heat radiated by A_1 in all directions (2π solid angle) is defined as the view factor $F_{A_1-A_2}$ from area A_1 to A_2.

From this definition of $F_{A_1-A_2}$, the very useful reciprocity relation

$$A_1 F_{A_1-A_2} = A_2 F_{A_2-A_1}$$

follows immediately. Another useful relation for deriving one view factor from others is based on conservation of energy. This states that if a surface A_1 radiates to surface A_2 and $A_2 = A_2' + A_2''$, then

$$F_{A_1-A_2} = F_{A_1-A_2'} + F_{A_1-A_2''}$$

B. Four Elementary View Factors

Formulas for the four basic view factors which are used in the determination of the over-all grid system view factors are given below.

1. Cylinder Walls to Disk

In the previous quarterly report the view factor from the walls of a cylinder to a disk was derived. With new notation corresponding to the figure below, the formula is

$$X = \frac{h}{\ell}, \quad Y = \frac{r}{\ell}$$
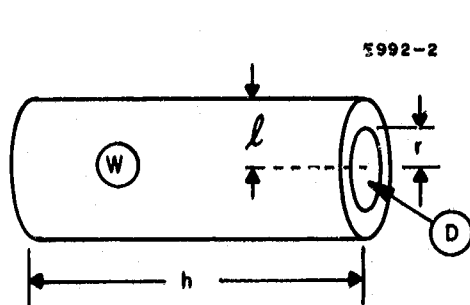
$$F_{WD}(X, Y) = \frac{1}{4X}\left\{ \sqrt{(X^2 + Y^2 + 1)^2 - 4Y^2} - (1 - Y^2)^2 - X^2 \right\}$$
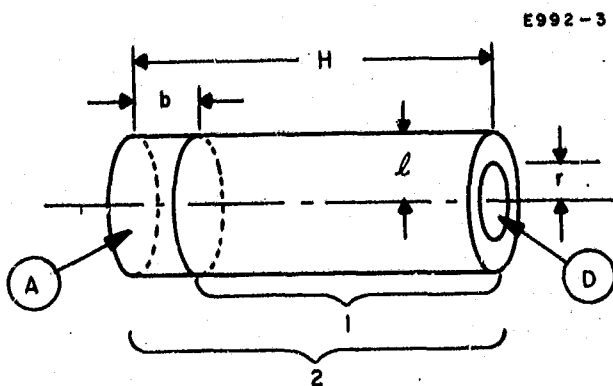
2. Section of the Cylinder Wall to Disk

Using the reciprocity law in the relation,

166

$$F_{D-2} = F_{D-A} + F_{D-1} - 1$$

gives

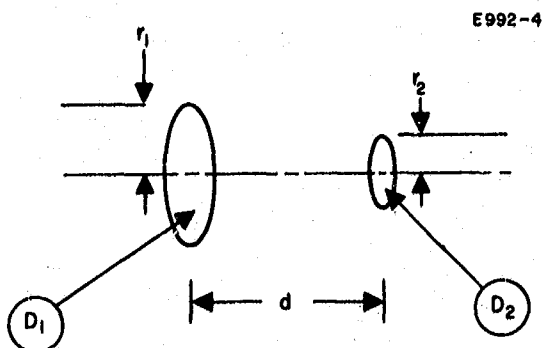$$A_2 F_{2-D} = A_A F_{A-D} + A_1 F_{1-D'}$$

where

E992-3

$$A_1 = 2\pi\ell (H-b)$$

$$A_2 = 2\pi\ell H$$

$$A_D = \pi r^2$$

$$F_{1-D} = F_{WD}\left(\frac{H-b}{\ell}, \frac{r}{\ell}\right)$$

$$F_{2-D} = F_{WD}\left(\frac{H}{\ell}, \frac{r}{\ell}\right) .$$

The view factor from the section of a cylinder A to the disk D is then found to be

$$F_{AD}(H, b, \ell, r) = \frac{H}{b} F_{WD}\left(\frac{H}{\ell}, \frac{r}{\ell}\right) - \frac{H-b}{b} F_{WD}\left(\frac{H-b}{\ell}, \frac{r}{\ell}\right) .$$

The next two view factors are found in many texts. See, for example, Eckert.[*]

3.   Disk to Disk

E992-4

$$X = \frac{d}{r_1}, \quad Y = \frac{r_2}{d}$$
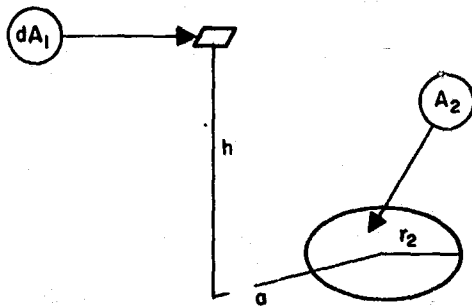
$$Z = 1 + (1 + Y^2) X^2$$

$$F_{DD}(r_1, r_2, d)$$

$$= \frac{1}{2}\left\{ Z - \sqrt{Z^2 - 4(XY)^2} \right\}$$

---

[*]E. Eckert, Heat and Mass Transfer (McGraw-Hill, New York, 1959).
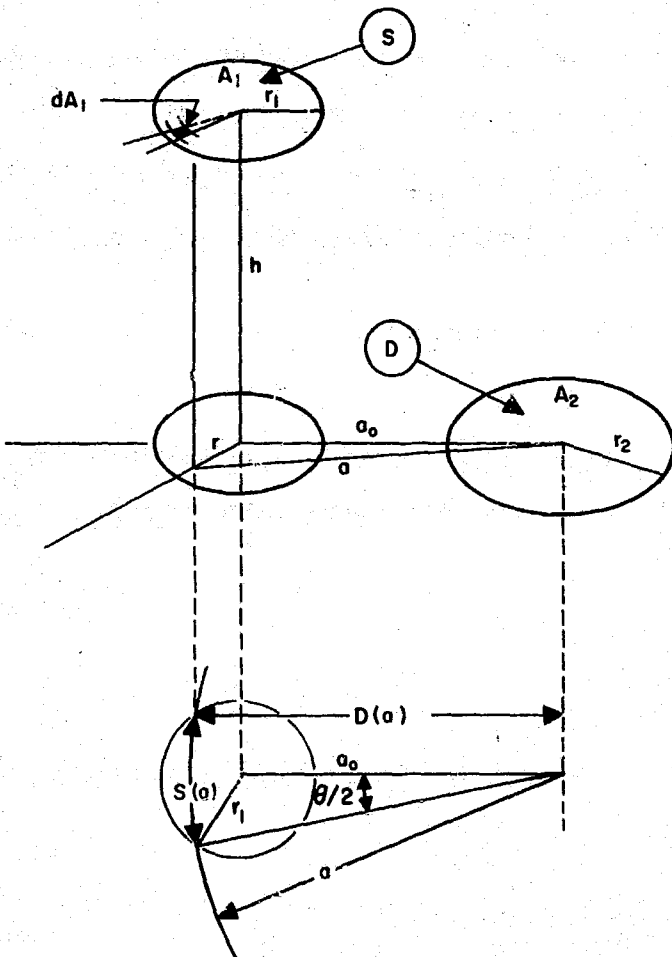
4. Area Element to Disk

E992-5

$$X = \frac{h}{a}, \quad Y = \frac{r_2}{h}$$

$$Z = 1 + (1 + Y^2) X^2$$

$$F_{dA_1 - A_2} = \frac{1}{2} \left\{ 1 - \frac{Z - 2X^2 Y^2}{\sqrt{Z^2 - 4X^2 Y^2}} \right\}$$

5. Disk to Off-Axis Disk

E992-6

The view factor from a disk A_1 to a parallel but off-axis disk A_2 is found from the integral of $F_{dA_1 - A_2}$:

$$F_{A_1 - A_2} = \frac{1}{A_1} \int_{A_1} F_{dA_1 - A_2} \, dA_1 .$$

This integral must be calculated numerically; the most convenient form is

$$F_{A_1 - A_2} = \frac{1}{A_1} \int_{a_o - r_1}^{a_o + r_1} F_{dA_1 - A_2} S(a) da$$

168

$$S(a) = 2a \cos^{-1} \left| \frac{D(a)}{a} \right| , \qquad D(a) = \frac{a_o^2 + a^2 - r_1^2}{2a_o} .$$

In the applications below, the view factor $F_{A_1-A_2}$ is referred to as $F_{SD}(h, r_1, r_2, a_o)$, i.e.,

$$F_{SD}(h, r_1, r_2, a_o) = \frac{1}{A_1} \int_{a_o-r_1}^{a_o+r_1} F_{dA_1-A_2} S(a) \, da .$$

C. Calculation of View Factors for the Grid System

1. View Factor F_{1-2}

The figure at right shows a pair of aligned apertures in the perforated plates S and A. Node 1 corresponds to the disk which is at the back of the plate S aperture and node 2 corresponds to the cylindrical aperture wall. (For simplicity, the screen apertures are not countersunk.) The view factor F_{1-2} is given by
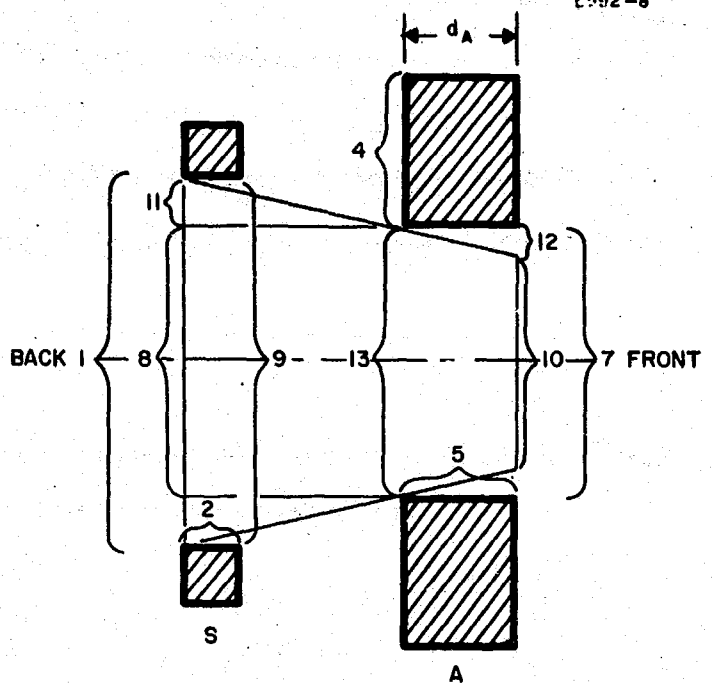
$$F_{1-2} = 1-F_{1-9} = 1-F_{DD}(r_s, r_s, d_s) .$$

169

2. View Factor F_{1-7}

Node 7 is a disk which is the front of the plate A aperture. Auxiliary nodes 8, 10, 11, and 12 are also used in the calculation of F_{1-7}. Nodes 8 and 10 are disks concentric to 11 and 7, and nodes 11 and 12 are the remaining annuli. An "aperture" effect is present in the calculation of F_{1-7} because of the nonzero thickness d_A of plate A. Thus F_{1-7} is a function of d_A. It would be difficult to account for this partial shielding between nodes 1 and 7 in the view factor calculation. Instead, upper and lower bounds are found for $F_{1-7}(d_A)$. From the geometry it is clear that for $d_A > 0$,

$$F_{1-7}(d_A) < F_{1-7}(0) .$$

A good lower bound for $F_{1-7}(d_A)$ is found as follows. Using the equations

$$F_{1-7}(d_A) = F_{1-12} + F_{1-10}$$

$$F_{1-12} = \frac{A_{11}}{A_1} F_{11-12} + \frac{A_8}{A_1} F_{8-12} ,$$

we obtain

$$F_{1-10} + \frac{A_8}{A_1} F_{8-12} + \frac{A_{11}}{A_1} F_{11-12}(d_A) = F_{1-7}(d_A) < F_{1-7}(0)$$

$$= F_{1-10} + \frac{A_{11}}{A_1} F_{11-12}(0) + \frac{A_8}{A_1} F_{8-12} .$$

Thus the inequalities

$$F_{1-10} + \frac{A_8}{A_1} F_{8-12} < F_{1-7}(d_A) < F_{1-7}(0) \tag{I-1}$$

bound $F_{1-7}(d_A)$ below by taking $F_{11-12}(d_A) = 0$ and above by having $F_{11-12}(d_A) = F_{11-12}(0)$. Since $F_{11-12}(d_A) < F_{11-12}(0) \ll 1$, the complicated view factor $F_{11-12}(d_A)$ is actually negligible. In terms of the elementary view factors given, eq. (I-1) becomes

$$F_{DD}(r_S, r_{10}, w) + \left(\frac{r_A}{r_{10}}\right)^2 \left\{ F_{DD}(r_A, r_A, w) - F_{DD}(r_A, r_{10}, w) \right\} < F_{1-7}(d_A)$$

$$\text{(I-2)}$$

$$F_{1-7}(d_A) > F_{DD}(r_S, r_A, w) \qquad \text{(I-3)}$$

where

$$w = d_S + d + d_A$$

$$r_{10} = r_A - \frac{d_A}{d+d_S}(r_S - r_A) \ .$$

3.   View Factor F_{1-4}

Node 4 corresponds to all of the material on the back side of plate A. The auxiliary nodes 9 and 13 are disks corresponding to the front of the plate S aperture and the back of the plate A aperture. The view factor F_{1-4} will be found from the relation

$$F_{1-4} = F_{1-9} - F_{1-13'} \ ,$$

where node 13' corresponds to the disks at the back of __all__ of the plate A apertures. The view factors F_{1-9} and $F_{1-13'}$ are given by

$$F_{1-9} = F_{DD}(d_S, r_S, r_S)$$

$$F_{1-13'} = F_{DD}(d_S + d, r_S, r_A) + 6 F_{SD}(d_S + d, r_S, r_A, S_o) \ .$$

In the expression for $F_{1-13'}$ only the six apertures surrounding node 13 were considered, and the shielding due to the thickness of plate S was neglected. The approximate expression for F_{1-4} is then

$$F_{1-4} = F_{DD}(d_S, r_S, r_S) - \{F_{DD}(d_S + d, r_S, r_A) + 6F_{SD}(d_S + d, r_S, r_A, S_o)\}.$$

4.   View Factor F_{1-5}

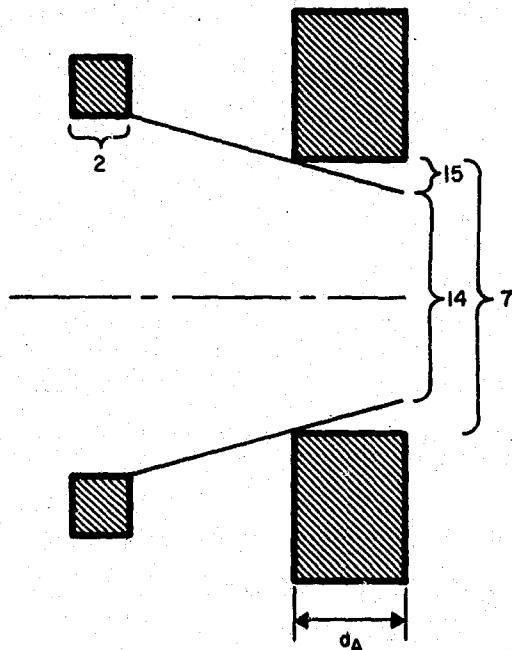Node 5 represents the cylindrical wall of the aperture in plate A. It is easily seen that

$$F_{1-5} = F_{1-13} - F_{1-7}$$

$$F_{1-5} = F_{DD}(d_S + d, r_S, r_A) - F_{1-7}(d_A)$$

where the value of $F_{1-7}(d_A)$ is chosen from (I-2) and (I-3).

5.   View Factor F_{2-7}

E992-22

As in the case of F_{1-7}, there is partial shielding in the path from node 2 to node 7, because of the nonzero thickness d_A of plate A. Instead of calculating $F_{2-7}(d_A)$ precisely, an estimate is made based on upper and lower bounds. An upper bound which neglects the shielding completely is $F_{2-7}(d_A) < F_{2-7}(0)$. A lower bound which omits the difficult view factor F_{2-15} is $F_{2-7}(d_A) > F_{2-14}$. In terms of the elementary view factor formulas these bounds become

$$F_{AD}(w, d_S, r_{14}, r_S) < F_{2-7}(d_A) < F_{AD}(w, d_S, r_A, r_S)$$

172

where

$$w = d_S + d + d_A ,$$

$$r_{14} = r_A - \frac{d_A}{d} (r_S - r_A) .$$

6. View Factor F_{2-5}

The view factor F_{2-5} is found from the relation

$$F_{2-5} = F_{2-13} - F_{2-7};$$

node 13 is shown in the figure in Section C-1 of this appendix. The formula for F_{2-5} is

$$F_{2-5} = F_{AD}(d_S + d, d_S, r_A, r_S) - F_{2-7}(d_A)$$

where an estimate of $F_{2-7}(d_A)$ is made using (I-1).

7. View Factor F_{2-2}

Since node 2 represents a concave surface it radiates to itself. The view factor F_{2-2} is found from the equation

$$F_{2-9} + F_{2-1} + F_{2-2} = 1,$$

and is given by

$$F_{2-2} = 1 - 2F_{AD}(d_S, d_S, r_S, r_S) .$$

8. View Factor F_{3-4}

Node 3 represents all the material surface on the front of plate S. The calculation of F_{3-4} takes several steps. First we find F_{9-4} from the equations

$$F_{9-4} = 1 > F_{9-13'}$$

$$F_{9-13'} = F_{9-13} + 6F_{SD}(d, r_S, r_A, S_o) \ .$$

The expression for $F_{9-13'}$ includes only the six nearest holes surrounding node 13. More distant groups of holes consist of 6 $\sqrt{3}\,S_o$, 6 at $2S_o$, 12 at 1.5 $\sqrt{3}\,S_o$, etc. The view factors from node 9 to node 13 and to each of the above groups are shown in Fig. I-1 as functions of the plate spacing d. The contributions to the over-all view factor $F_{9-13'}$ from holes more distant than S_o are negligibly small. Next, we define node 9' as the disks corresponding to the fronts of all the holes in plate S, and note that

$$F_{9'-4} = F_{9-4} \ .$$

The view factor $F_{4-9'}$ is then found from the reciprocity condition

$$F_{4-9'} = \frac{A_{9'}}{A_4}\, F_{9'-4} \ .$$

The area ratio $A_{9'}/A_4$ is defined by

$$\frac{A_{9'}}{A_4} = \frac{f_S}{1-f_A}$$

where f_S and f ꞏ the opened area fractions in plates S and A. Finally, the desired view factor F_{3-4} is found from the equations

$$F_{3-4} = \frac{A_4}{A_3}\, F_{4-3} = \left(\frac{1-f_S}{1-f_A}\right)^{-1} F_{4-3}$$
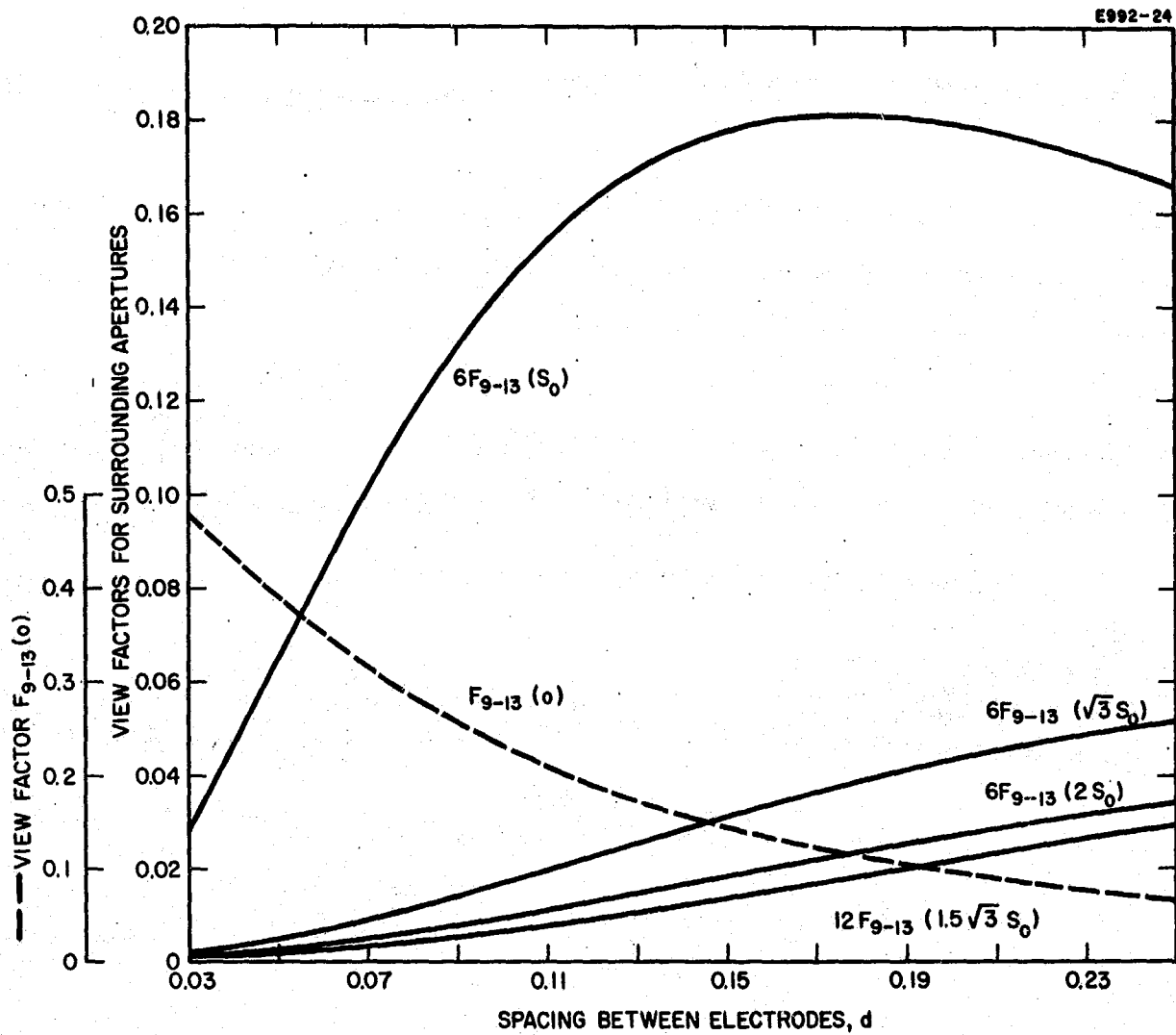
$$F_{4-3} = 1 - F_{4-9'} \ .$$

Fig. I-1. Terms in the over-all view factor F_{9-13}.

The resulting expression is

$$F_{3-4} = \left(\frac{1-f_S}{1-f_A}\right)^{-1} \left\{1 - \frac{f_S}{1-f_A}\left(1 - F_{DD}(d, r_S, r_A) - 6F_{SD}(d, r_S, r_A, S_o)\right)\right\}$$

9. **View Factors $F_{3-5'}$, $F_{3-7'}$**

Nodes 5' and 7' correspond to the cylindrical wall and front disk surface of all of the plate A apertures. From the equation

$$F_{3-13'} = 1 - F_{3-4} = F_{3-5'} + F_{3-7'},$$

we learn the sum $(F_{3-5'} + F_{3-7'})$. No good approximation has been found to date for either; the difficulty is apparently that the shielding due to plate A enters significantly. Until more time is spent on their calculation, we will take

$$F_{3-5'} = F_{3-7'} = \frac{1}{2} F_{3-13'} = \frac{1}{2}\left(1 - F_{3-4}\right).$$

10. **View Factors F_{5-7}, F_{5-5}**

The view factors F_{5-7}, F_{5-5} are given by the formulas

$$F_{5-7} = F_{AD}(d_A, d_A, r_A, r_A)$$

$$F_{5-5} = 1 - 2F_{5-7}.$$

176

APPENDIX II — A MODEL FOR THERMAL BUCKLING OF THE ELECTRODES

The simplified model of thermal buckling considered here was developed for the purpose of explaining the computer results for electrode buckling. An analytical solution of the model problem is obtained and shown to agree qualitatively with the computer results. In the model problem a peak also occurs in the curve of axial displacement versus initial axial position.

A. Computer Results for the Electrode

The buckling of an initially dished 30 cm molybdenum electrode (0.030 in. thick) due to a radial temperature gradient $T(r)$ was calculated (by a "finite element method" computer program) for various values of initial eccentricity e (see Fig. II-1). The electrode was assumed to be simply supported at the edge and to have no temperature variation through the thickness. The computer program actually analyzed a solid plate with one small (0.075 in.) central hole, but employed modified elastic constants E and ν to reflect that the electrode is perforated. A graph of the calculated deflection η/d versus e/d is shown in Fig. II-2. It is the negative slope portion of this curve for which an explanation is sought.

B. Model for Thermal Buckling

The model for thermal buckling consists of a triangle of rods, hinged at the vertices a, b, and c (Fig. II-3). Each rod has cross section A, Young's modulus E, and thermal expansion coefficient α. In the unloaded state (Fig. II-3(a)), the rods are in mechanical equilibrium with no internal stresses. The loaded state (Fig. II-3(b)), of the model is reached by heating rods ac and bc to temperature T, and in turn compressing spring S. Rod ab remains at zero temperature.
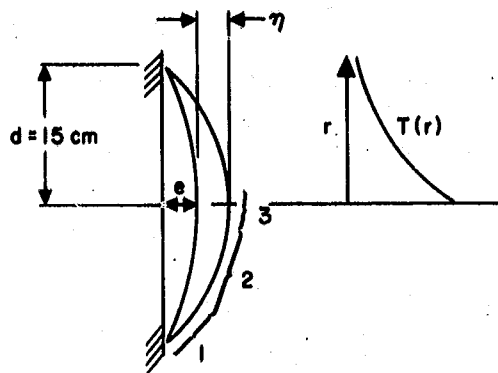
E1010-31
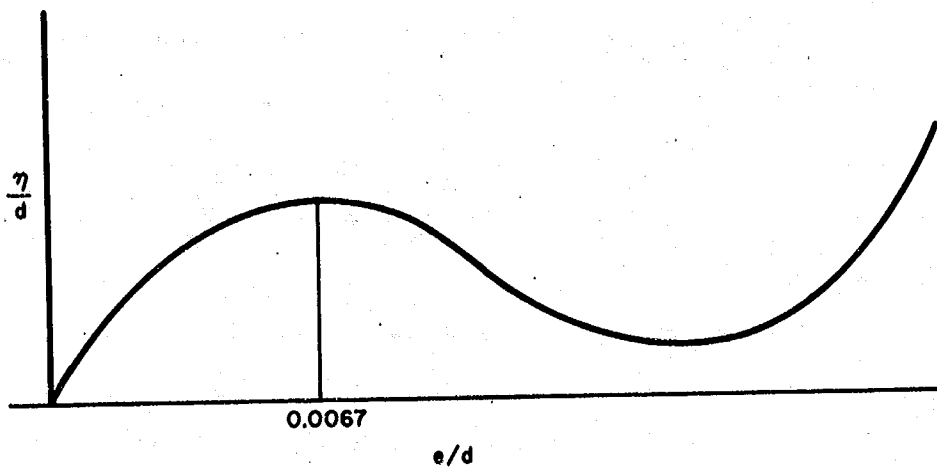

Fig. II-1.   Buckling geometry.

Fig. II-2.   Central deflection versus initial depth.
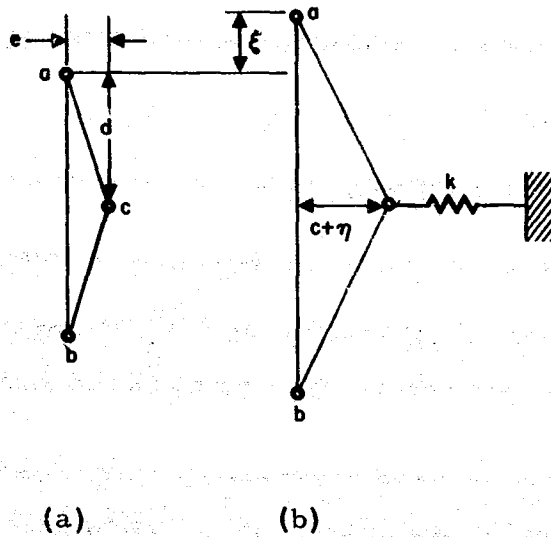
E1010-30

(a)   (b)

Fig. II-3. Model for thermal buckling.
(a) Unloaded. (b) Loaded.

The analogy of the state of Fig. II-3(b) with the deformed state of the electrode is as follows: (see Fig. II-1)

1.   Rod ab provides the radial clamping of the outer, relatively cold region 1 on the electrode.
2.   Rods ac and bc correspond to the thermally expanding central portion 2 of the electrode.
3.   The spring provides the bending resistance of the cap 3.

The solution of the thermal buckling problem under the assumptions

$$(e/d)^2 \ll 1, \quad (\xi/d)^2 \ll 1, \quad (\eta/d)^2 \ll 1, \quad aT \ll 1, \quad \beta \ll 1, \quad aT < 2\beta$$

is

$$\eta/d = \frac{(e/d)\, aT}{(e/d)^2 + 2\beta - aT} \qquad (II-1)$$

$$\beta = \frac{k/2}{EA/d} \; .$$

The graph of this solution is shown in Fig. II-4 for

$$a = 10^{-6}/{}^{\circ}F,$$
$$T = 100^{\circ}F,$$
$$E = 10^7 \text{ psi},$$
$$A = 0.1 \text{ in.}^2$$
$$d = 10 \text{ in.},$$
$$k = 100 \text{ lb/in.}$$

Upon examination of the force balance equations for equilibrium a physical explanation of the peak is discovered. Because of the spring the displacement η is proportional to the axial component of the compressive force F_c in rods ac and bc. The axial component is
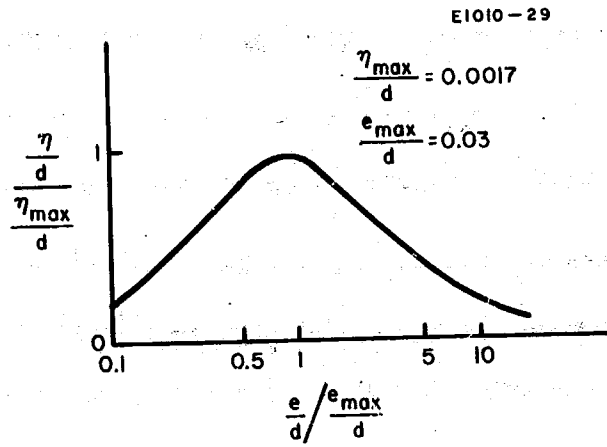
Fig. II-4. Solution of buckling model.

F_c sin $\not{\kappa}$ abc and sin $\not{\kappa}$ abc is proportional to e. It turns out that F_c is proportional to $(e^2 + \text{constant})^{-1}$ and therefore $\eta \, \alpha \, e/(e^2 + \text{constant})$. In the next paragraph the exact fourth degree algebraic equation for η is derived and solved for $(\eta/d)^2 \ll 1$. Additional assumptions of $(e/d)^2 \ll 1$, $\alpha T \ll 1$, $\beta \ll 1$ are made to further simplify the solution and obtain (II-1). These assumptions apply to realistic situations as in the example of Fig. II-4.

C. Derivation of Equation (II-1)

The length L_o of rods ac and bc before loading are, from Fig. II-3(a),

$$L_o = \{d^2 + e^2\}^{1/2} \quad . \tag{II-2}$$

After loading by thermal expansion and the spring force the length is, on the basis of Fig. II-3(b),

$$L = \{(d + \xi)^2 + (e + \eta)^2\}^{1/2} \quad . \tag{II-3}$$

The compressive force F_c in rods ac and bc is equal to the force required to compress each from length $L_o (1 + \alpha T)$ to length L and is

$$F_c = EA \frac{L_o(1 + \alpha T) - L}{L_o(1 + \alpha T)} \quad . \tag{II-4}$$

The tension force F_t in rod ab is equal to the force required to stretch it from length 2d to length $2(d + \xi)$ and is

$$F_t = EA \frac{2(d + \xi) - 2d}{2d} = EA \frac{\xi}{d} \quad . \tag{II-5}$$

Two equations for the unknown displacements ξ and η are provided by equating the vertical forces acting at hinge a and the horizontal forces at hinge c. These equations are

$$\frac{d + \xi}{L} \ F_c \ = \ F_t \qquad\qquad\qquad \text{(II-6)}$$

$$2 \frac{e + \eta}{L} \ F_c \ = \ k\eta \ . \qquad\qquad\qquad \text{(II-7)}$$

A single equation for η can be derived from (II-6) and (II-7) as follows. After substitution of the expression (II-4) for F_c, eq. (II-7) is solved for L to give

$$L \ = \ L_o \ (1 + aT) \ \frac{e + \eta}{e + A\eta} \qquad\qquad\qquad \text{(II-8)}$$

where

$$A \ = \ 1 + \frac{\beta L_o}{d} \ (1 + aT).$$

The relationship

$$\xi \ = \ \beta \ \frac{\eta d}{e + \eta \ (1-\beta)} \ , \quad \beta \ = \ \frac{k/2}{EA/d} \ , \qquad\qquad \text{(II-9)}$$

is found by dividing (II-6) by (II-7), is then used to eliminate ξ in (II-3) and obtain

$$L \ = \ \frac{e + \eta}{e + \eta(1-B)} \ \{d^2 + [e + \eta(1 - \beta)]^2 \}^{1/2} \ . \qquad \text{(II-10)}$$

Finally, equating (II-8) and (II-10) yields

$$L_o \ (1 + aT) \ \frac{e + \eta(1-\beta)}{e + \eta A} \ = \ \{d^2 + [e + \eta(1-\beta)]^2 \}^{1/2} \ . \qquad \text{(II-11)}$$

If the variables e and η are normalized and η' is assumed small, i.e.,

$$e' \ = \ (e/L_o), \quad \eta' \ = \ (\eta/L_o) \ll 1,$$

eq. (II-11) simplifies to

$$(1 + aT) \{ e' + \eta' (1-\beta) \} = \{ 1 + \eta' \{ 2e(1-\beta) + \eta' (1-\beta)^2 \} \}^{1/2} (e' + \eta' A)$$

$$= \{ 1 + \eta' \{ e' (1-\beta) + \frac{1}{2} \eta' (1-\beta)^2 \} \} (e' + \eta' A)$$

$$= e' + \eta' \{ A + e'^2 (1-\beta) \} + \ldots \qquad \text{(II-12)}$$

Solving (II-12) for η' gives

$$\eta' = \frac{e' \, aT}{e'^2 (1-\beta) + \beta \left(1 + \dfrac{L_o}{d} \right) (1 + aT) - aT} \qquad . \qquad \text{(II-13)}$$

Under the additional assumptions that

$$e'^2 \ll 1, \, aT \ll 1, \, \beta \ll 1,$$

eq. (II-13) reduces to

$$\eta' = \frac{e' \, aT}{e'^2 + 2\beta - aT} \qquad .$$